# THE DEVELOPMENT OF MEASUREMENT TECHNIQUES TO IDENTIFY AND CHARACTERIZE DUSTS AND ICE NUCLEI IN THE ATMOSPHERE

A Dissertation

by

ANDREW GLEN

Submitted to the Office of Graduate and Professional Studies of
Texas A&M University
in partial fulfillment of the requirements for the degree of

DOCTOR OF PHILOSOPHY

| | |
|---|---|
| Chair of Committee, | Sarah D. Brooks |
| Committee Members, | Don Collins |
| | Ping Yang |
| | Andrew G. Klein |
| Head of Department, | Ping Yang |

May 2014

Major Subject: Atmospheric Sciences

# ABSTRACT

Mineral dusts and ice crystals directly influence the Earth's radiative budget through radiative scattering and absorption. The interaction of spherical particles on the radiative budget are well known, however mineral dusts and ice crystals are generally non-spherical leading to large uncertainties in the radiative impacts of these particles. In addition, atmospheric dust has the ability to act as an Ice Nuclei (IN) aiding in the formation of ice crystals in the atmosphere through four well known nucleation mechanisms. The work presented here discusses new instrumentation and methods to measure and identify both the optical scattering properties and ice nucleation properties of atmospherically relevant dusts.

The Texas A&M University Continuous Flow Diffusion Chamber (CFDC) was constructed and characterized in the laboratory using a known effective IN, silver iodide. This instrument was then deployed in the Arctic as part of the Indirect Semi-Direct Aerosol Campaign (ISDAC) where it measured the concentration of potential IN under atmospheric conditions. The results of which, showed the Arctic has higher particle concentrations during the spring compared to data collected in the fall during other field projects. In addition, extreme nucleation events were observed with average IN concentrations as high as 100 $L^{-1}$.

The optical scattering properties of atmospherically relevant dusts were measured using a prototype instrument, the Cloud Aerosol Spectrometer with Polarization (CASPOL) under laboratory conditions. The data collected using this instrument allowed

the classification of 13 atmospherically relevant dusts into 3 distinct groups based on the optical scattering properties. This instrument was then upgraded by the manufacturer and used to measure the optical scattering properties of both atmospherically relevant dusts and ice crystals generated using the CFDC with the previously examined dusts as potential IN. The results show the dusts can still be categorized into 3 distinct groups and can be differentiated from generated ice crystals. These results provide methodologies for differentiating atmospheric dust from ice crystals in the atmosphere using remote sensing instrumentation.

# ACKNOWLEDGEMENTS

First, I would like to take this opportunity to thank all the people who helped and provided support throughout my Ph.D. I would like to extend my appreciation to Dr Sarah Brooks, for her role as my advisor. Dr Brooks provided thoughtful insight into my research and encouraged me to develop my skills as a researcher and a scientist by building upon my strengths and improving areas of weakness. Her willingness to work with me throughout my time as a "non-traditional" student is greatly appreciated.

I would also like to thank my committee members, Dr. Don Collins, Dr, Ping Yang and Dr. Andrew Klein, for their guidance and support throughout the course of this research. In addition, a thanks must go out to all my research group peers, in particular Dr. German Vidaurre, for their role in my growth as a scientist. Also thanks must be given to Darrel Baumgardner and his colleagues at DMT for help and support with the CASPOL instrument. Furthermore, thanks must be given to the numerous people around the world who I have had the opportunity to work with throughout my research.

I cannot forget to thank my family, especially my parents, Malcolm and Sally, who have encouraged me to push myself and have always supported my decisions no matter how far from home they have taken me.

Finally, I would like to thank my wonderful wife Crystal for all her love, encouragement, patience and support throughout this work. Crystal was always there to provide the coffee needed to keep me working through the long stressful nights or the delivery of a home cooked meal during the extended lab work. She always provided a

willing sounding board for my ideas and frustrations, with kind words of encouragement whenever I needed them. Without her the world would certainly be duller, she is my sunshine when the clouds are gray.

TABLE OF CONTENTS

Page

LIST OF FIGURES

Page

LIST OF TABLES

Page

# 1. INTRODUCTION

## 1.1 Importance of Dust in the Atmosphere

Mineral dusts strongly influence the Earth's radiative budget through scattering and absorption of light (Attwood and Greenslade, 2011; Sassen, 2002). Atmospheric dust comprises approximately 45% of the total aerosol mass loading of the atmosphere (Caquineau et al., 2002). The direct radiative impact of this loading produces an estimated net cooling effect of approximately -0.1 $Wm^{-2}$ (IPCC, 2007). In addition, atmospheric dust influences liquid droplet and ice nucleation (Chen et al., 1998; Kanji and Abbatt, 2009), the deposition of micronutrients into oceans (Duce and Tindale, 1991; Uematsu et al., 2003) and regional air quality (Prospero, 2006; Prospero et al., 2001). Mineral dust lifetimes in the troposphere can be on the order of a week for particles smaller than 10 μm, while larger particles are removed faster by sedimentation due to gravity and by precipitation (Attwood and Greenslade, 2011). Hence, deposition occurs hundreds and sometimes thousands of miles from the source. For example, Saharan dust can spread along three major pathways: westward over the Atlantic Ocean to the Americas, northward over the Mediterranean to Europe, and eastward to the Middle East (Goudie and Middleton, 2001). Several other source regions around the world are characterized by dusts of differing physical and chemical properties and areas of influence. For example, the Simpson-Stzelecki Desert of Central Australia is rich in iron oxides (Bullard and White, 2002), while the Gobi Desert is composed primarily of

crustal material and carbonates (Xu et al., 2004). Various dusts have visibly observable differences, such as color which is often a sign of oxidation state and surface morphology which is an indication of atmospheric aging and processing (Bullard and White, 2002). Aerosol optical properties are influenced by the composition, age, shape, morphology, refractive index, number concentration and size distribution of the particle population (Bi et al., 2009; Curtis et al., 2008; Mishchenko et al., 1997; West et al., 1997; Yang and Liou, 2006).

The direct radiative effect of light scattering by spherical aerosols can be calculated using Mie theory (Bohren and Huffman, 2004; Morgan et al., 2010). The earth's radiative balance and climate are driven by interactions between sunlight and a variety of constituents in the atmosphere. The most difficult interactions to predict and hence the largest uncertainties in climate predictions are those involving non-spherical particles in the atmosphere, including aerosols such as dust, soot, pollen, and frozen ice cloud particles (Archuleta et al., 2005; Carlson and Benjamin, 1980; Dessler and Yang, 2003; IPCC, 2007). However, the optical properties of non-spherical particles such as dust are more challenging to predict theoretically. One approach is to calculate the volume equivalent spherical size and use that in Mie calculations (Clavano et al., 2007). This method leads to significant differences between non-spherical particles and spherical particles of equivalent size (Mishchenko et al., 1997; West et al., 1997). Other methods such as T-Matrix (Mishchenko et al., 1997), Discrete Dipole Approximation (DDA) and Improved Geometric Optics Methods (IGOM) for modeling optical properties of particles with specified geometries can be used (Bi et al., 2009). However,

it has been shown that polarization and backscattering intensities are unique to individual particle geometries (Bohren and Singham, 1991; Clavano et al., 2007; Mishchenko, 2009; Mishchenko et al., 1997). Experimental validation is needed to examine the applicability of these numerical methods for determining the optical properties of non-spherical particles.

While many laboratory studies have investigated the optical properties of non-spherical dusts, properties are typically determined for ensembles of particles (Arakawa et al., 1997; Attwood and Greenslade, 2011; Curtis et al., 2008; West et al., 1997). For example, Attwood and Greenslade (2011) determined the relative humidity dependence of light extinction for three clays, including illite, kaolinite, and montmorillonite. Curtis et al. (2008) measured the scattering of light by populations of dusts over a larger range of collection angles, approximately 17° to 176°. The dust samples used in that study were Arizona Test Dust (ATD), silicate clays including illite, kaolinite, and montmorillonite, and non-clay minerals such as calcite, gypsum, hematite, and quartz. The scattering phase function of non-spherical mineral dusts over multiple scattering angles (15° to 170°) was measured by West et al. (1997). Their results showed variation in the change in polarization state of light depending on the types of dust sampled. Glen and Brooks (2013) showed through direct measurement techniques using the CASPOL instrument, that various types of dusts exhibited distinctly different scattering properties.

Remote sensing measurements of ambient atmospheric dust are important, as they provide a much greater spatial and temporal coverage of dust ensembles than in-situ measurements. In addition, the use of multiple detectors and wavelengths provides

additional information on particle properties. For example, depolarization ratio, defined as the ratio of returned powers in the planes of the polarization orthogonal and parallel to that of the linearly polarized source, can be used to determine particle sphericity (Sassen, 1991). Mishchenko et al. (1997) showed that even after applying particle size and orientation averaging, a single spheroidal shaped particle always produces a unique shape specific phase function distinctly different from those produced by other spheroidal particles. Thus depolarization ratios can be used to differentiate non-spherical or rough particles from spheres. For example, a dual wavelength Mie scattering lidar was employed to obtain aerosol particle size information and sphericity for Asian dust and anthropogenic plumes in the Northwest Pacific (Sugimoto et al., 2002). The depolarization ratio is also dependent on the orientation of the non-spherical particles, i.e. horizontally orientated particles have different backscatter and depolarization characteristics than vertically orientated particles (Cho et al., 2008). Highly irregular particle morphologies typically have a low backscatter signal and a high depolarization ratio (Cho et al., 2008). Although depolarization ratio is the working definition for a parameter used in various studies, it has been noted that technically the interaction between particles and linearly polarized light does not explicitly depolarize the incident light but instead changes the state of the polarized light (Harris-Hobbs and Cooper, 1987).

## 1.2 Importance of Ice in the Atmosphere

Both dust and ice crystals are influential in the radiative balance of the atmosphere and their influences are heavily modified due to their non-spherical nature. It is well known that that dusts have the ability to act as ice nuclei albeit to varying degrees (Atkinson et al., 2013; Koehler, 2007; Koehler et al., 2010).

The percentage of ice crystals present in the atmosphere is strongly dependent on the presence of ice crystal containing clouds such as cirrus; it is estimated that cirrus clouds cover 30% of the Earth's surface (Cziczo et al., 2013). Even with the prevalence of non-spherical dust and ice crystals in the atmosphere and their relevance to climate, they still remain poorly understood with medium to low levels of scientific understanding (IPCC, 2007).

There are two general mechanisms by which ice particles can exist in the atmosphere, through either homogeneous freezing or heterogeneous freezing mechanisms (Vali, 1999). Heterogeneous nucleation can take place via condensation, contact, immersion or depositional freezing. Homogeneous freezing of an aqueous solution droplet in the atmosphere can only occur at temperatures below -40°C whereas heterogeneous freezing of super cooled liquid water droplets requires the aid of an atmospheric particle such as an effective ice nuclei (IN), and typically occurs at temperatures warmer than ~ -36°C (Isono, 1955; Vali, 1999). Continuous Flow Diffusion Chambers (CFDC) are the preferential instrument for measuring the potential activation of IN and growth of ice crystals in situ (Archuleta et al., 2005; DeMott et al.,

2011; Prenni et al., 2006; Rogers et al., 2001b, 1998). Within these chambers heterogeneous nucleation of a suitable IN using available liquid water and water vapor and can take place via contact, immersion or depositional freezing. Contact and immersion freezing mechanisms require the availability of liquid water droplets (supersaturated with respect to water) before freezing can occur. However, the depositional freezing mechanism can occur when the ambient conditions are sub saturated with respect to liquid water. Typically, effective heterogeneous IN are insoluble solids such as mineral dust.

Several studies have shown that desert dust, as one example, can act as an effective IN under specific temperature and supersaturation conditions (Chen et al., 1998; Creamean et al., 2013; Kanji and Abbatt, 2009; Rosenfeld et al., 2011). Despite the large atmospheric loading of particulate matter, the concentration of IN in the atmosphere is very low, typically 1 in $1x10^5$ particles, making it difficult to accurately measure their importance.

The full extent of small ice crystals on the radiative balance is not well known. Ice crystals are typically non-spherical particles (Heymsfield and Iaquinta, 2000), with varying shapes which span the range from plates, to columns, droxtals, bullet rosettes, aggregates, and random irregular (Yang and Liou, 2006). Ice crystal shapes are controlled by the temperature and supersaturation conditions under which the ice forms, the seed IN composition, and whether or not melting or fracturing of the ice crystal has occurred (Bailey and Hallett, 2004). The radiative properties of ice crystals have been studied both in-situ and by modeling studies. In order to understand the optical scattering

properties of ice particles, shape as well as crystal habit, number concentration, and other microphysical properties must also be considered (Lin et al., 1998; Liou, 1986). Typically, studies of ice crystals have focused on the larger sized particles, with diameters greater than 30 μm. However, it was shown by Noone et al. (1993) and Ström et al. (1994) that a large fraction of the number concentration of ice particles in cirrus clouds resides below 10 μm. Since these results were published, modeling efforts began to examine the importance of small ice crystals in radiative processes and found that incorporating these small crystal populations into the model can improve model performance by over 10% (Zender and Kiehl, 1994). In addition, Lin et al. (1998) determined that small ice crystals, those having a mean diameter near 0.1 μm, are important in cirrus cloud formation processes.

Although remote sensing techniques have been improving in recent years, there is still uncertainty in determining the difference between atmospheric dust and ice crystals by satellite platforms. Ice crystals in cirrus clouds can often be missed by satellite measurements if the cloud is optically thin (Dessler and Yang, 2003). In addition, the determination of the particle type, either dust or ice crystal, is limited due to the non-spherical nature of both these particle types. Liu et al. (2008) studied vertical profiles of atmospheric dust in the Ganganagar, Taklimakan and Gobi desert regions using the CALIPSO lidar and found depolarization ratios as high as 0.3 for dust in the lower layers of the atmosphere. Hu et al. (2007) and later, Cho et al. (2008) illustrate a relationship between CALIPSO derived depolarization ratio and backscattering intensities for non-spherical particles, they show that ice crystals can have depolarization

ratios ranging from 0.1 to 0.5 with varying backscatter intensities. Baum et al. (2005a) and Baum et al. (2005b) show that there are substantial differences in the bulk scattering properties of ice clouds depending on the habit of the ice crystals and the wavelength of radiation. The need of the remote sensing community to improve the differentiation between dusts and ice crystals is of great importance if the understanding of the radiative balance of the atmosphere is to be further improved.

# 2. CONTINUOUS FLOW DIFFUSION CHAMBER

The construction and development of a Continuous Flow Diffusion Chamber (CFDC) was undertaken at Texas A&M University. The following section discusses the construction of this instrument and data collected during its development. The CFDC is an instrument designed to measure the ice nucleation potential of aerosol under specifically controlled conditions of temperature and supersaturation. This instrument has been used in both laboratory and field studies to assess potential Ice Nuclei (IN) activation.

## 2.1 CFDC Description

The CFDC measures in-situ IN concentrations as a function of operational chamber conditions. Both temperature and supersaturation can be adjusted to create a controlled environment for IN activation, with the aerosol sample temperature ranging from ≈ -50 °C to -10 °C, and supersaturation with respect to ice from 0 to 50%.

The sample air entering the CFDC is initially dried using desiccant driers and flows through a cyclone impactor which removes particles larger than ~ 1.6 μm. The sample then enters the chamber through a focusing ring, surrounded by the sheath air. The chamber is composed of two concentric cylinders with air flowing vertically downward within the annulus. Prior to the sampling of the aerosol, the walls of each cylinder are cooled to different temperatures using a custom built refrigeration system

and are coated with a uniformly thin layer of ice. This is done by utilizing a sliding plate at the base of the chamber to allow De-Ionized (DI) water to be pumped into the chamber when its cooled, ice then forms on the walls and the remaining water is drained out. Generally during operation, the outer wall is warmer than the inner wall, the temperature gradient across the chamber generates the supersaturation field, similar to that shown in Figure 1 (adapted from Rogers (1988) and Rogers (1994)).

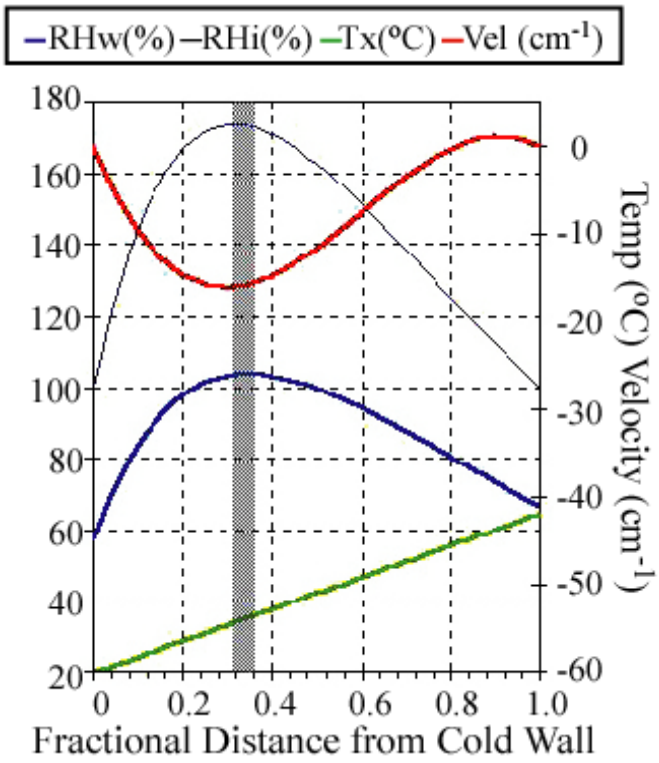


**Figure 1. Temperature, relative humidity and aerosol location profiles within a CFDC. Adapted from Rogers, (1988 and 1994).**

The air which flows through the annulus between the walls is comprised of a sheath and sample flow; the sheath air flowing closest to each of the walls with the sample air in laminar flow contained between the two sheath air streams (Figure 2). The aerosol sample is then exposed to the saturation region within the chamber and grows accordingly. At the base of the chamber is a Climet Optical Particle Counter (OPC) which counts the number of activated IN. The exhaust of the OPC is connected to a flow controller which controls the total flow rate through the CFDC system generated by a downstream air pump. The pump then re-circulates air through a series of filters and desiccant dryers to another flow controller which serves as the sheath air flow controller. The sheath air stream then enters into the CFDC through a series of "pin hole" orifices to constrain the aerosol sample flow. The full instrument schematic can be seen in Figure 3 and a photograph of the instrument is shown in Figure 4.

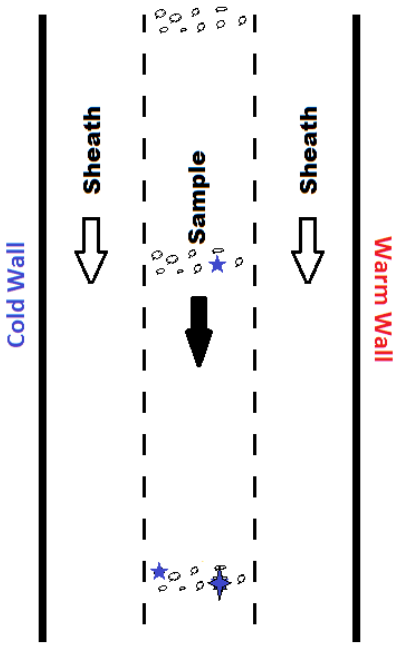


**Figure 2. The sheath and sample air flow within the CFDC annulus chamber.**

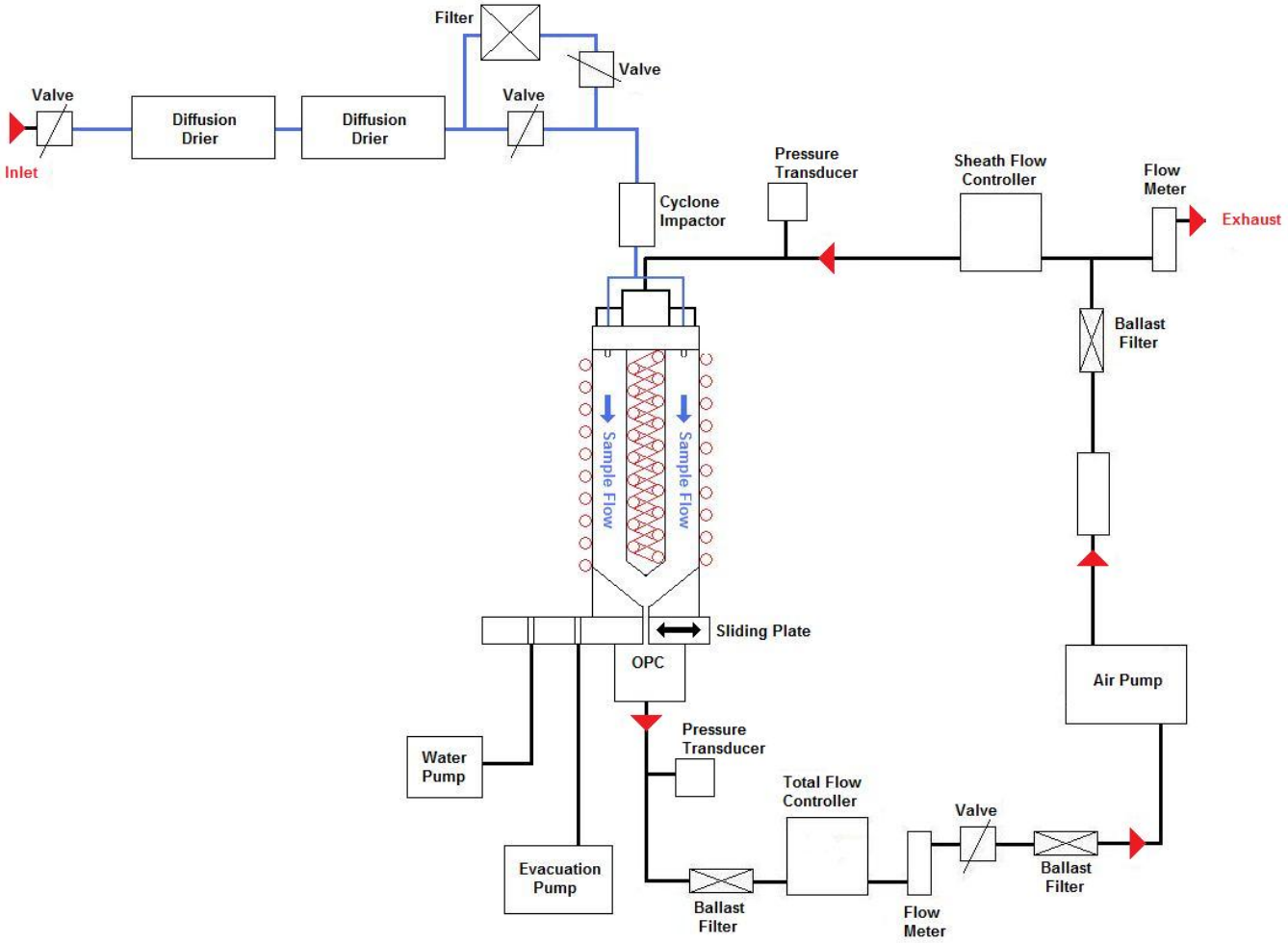


**Figure 3. Schematic of the CFDC including the inlet and recirculation system. A sliding plate is used to switch between conditioning, icing of the chamber and operational measurements.**

**Figure 4. Photograph of the fully constructed CFDC.**

## 2.2 CFDC Construction

A Solidworks rendering of the CFDC is shown in Figure 5 and is constructed from two 39" lengths of copper tubing, the outer wall of the chamber has a 4" diameter, and the inner wall of the chamber has a 3" diameter. The outer wall is wrapped with 3/8" copper tubing to make coils around the chamber for the refrigerant to flow through. These refrigeration coils are soldered to the outer wall. Similarly the inner wall has a series of coils wrapped inside of the 3" diameter tubing. A Delrin base holds the outer wall vertically, and has a cone shaped exit port at its base as seen in Figure 7. The inner wall has a stainless steel cone mounted to the bottom which has parallel angles to the cone shaped Delrin base of the outer wall. At the top of both chambers is a stainless steel manifold which has inlets for both the sample air (Marked in red on Figure 5 and Figure

6) and sheath air. The collar directs the sample air stream to a stainless steel focusing ring, while the sheath air is directed to a Delrin plate with "pin hole" orifices.

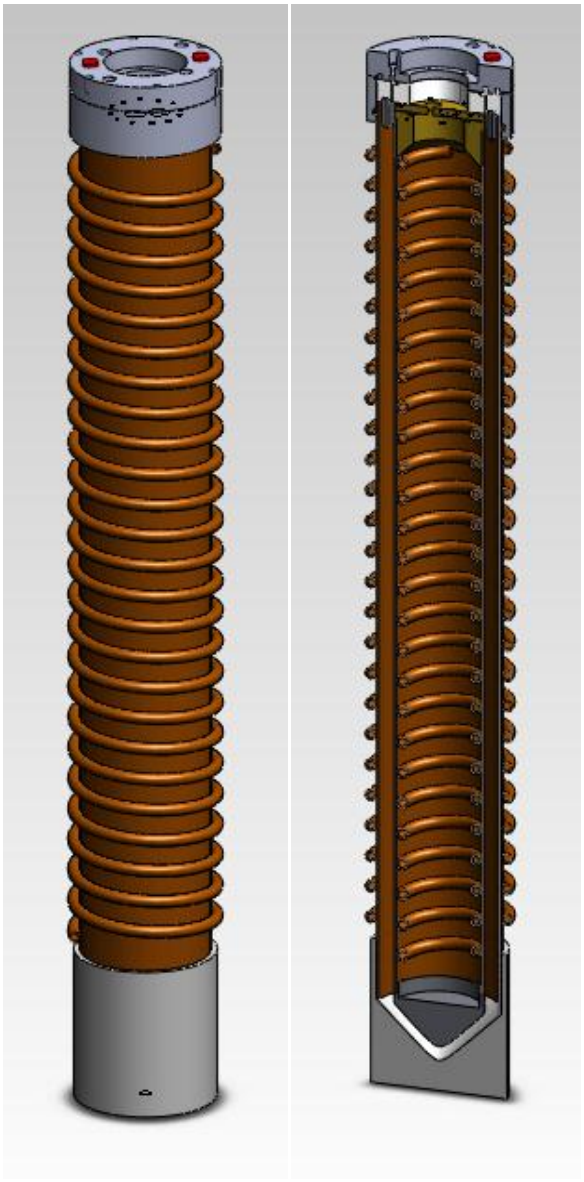

**Figure 5. Solidworks renders of the CFDC, the image on the left is the entire column. The image on the right shows a cross section of the chamber.**

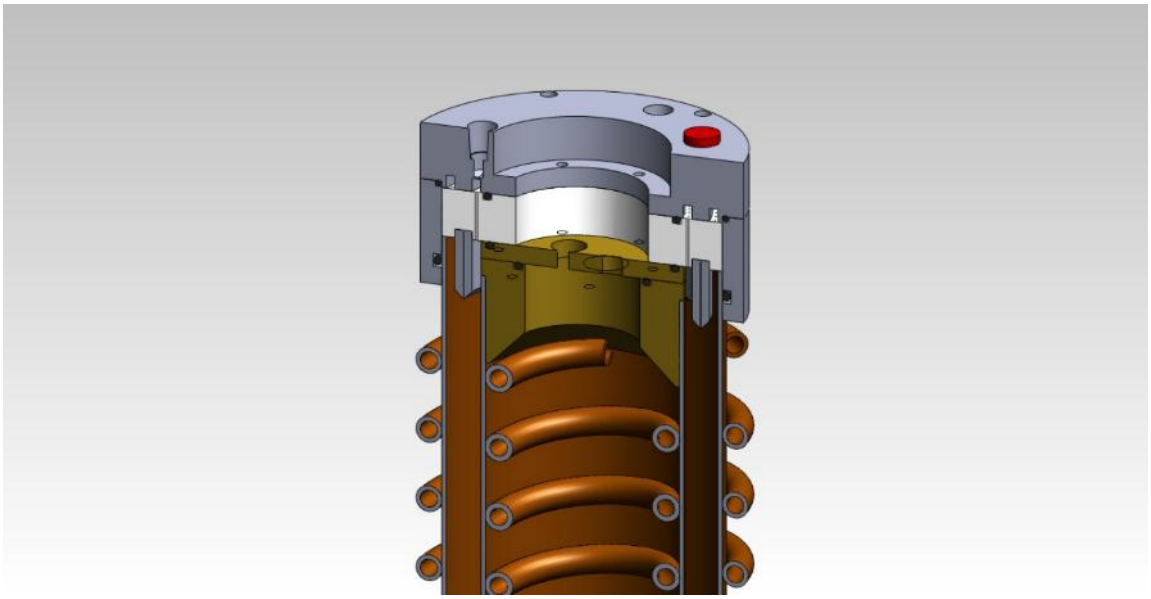

**Figure 6. An expanded view of the inlet manifold with the annular space of the walls, the knife edge inlet for the sample flow and inlets for the sheath flow.**

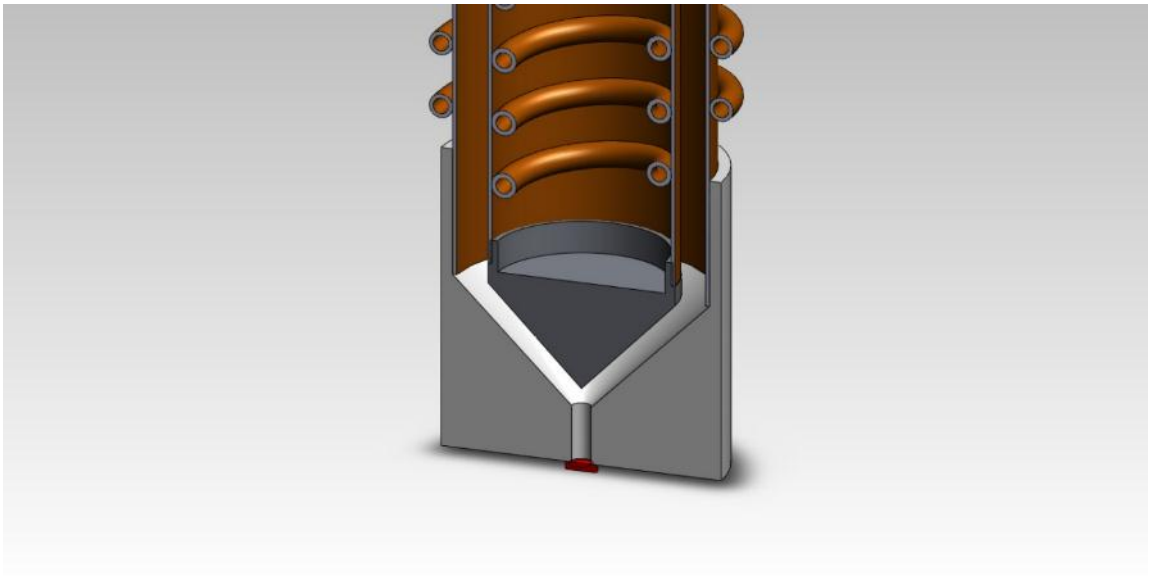

**Figure 7. The exit port at the base of the CFDC constructed out of Delrin. As the image shows there air moves through the annular space and exits out of a single exhaust port marked in red.**

## 2.3 CFDC Refrigeration System

The refrigeration system was designed and built specifically for this application. The system uses compressors to pump a refrigerant (SUVA) around the system. Cooling occurs when the liquid phase of the refrigerant boils and turns to vapor. Expansion valves are used above and below the chamber to control the flow and subsequently balance the boiling of the refrigerant at the coil – chamber wall interface. Each wall has its own independent compressor and isolated cooling pipes. A schematic of the cooling system is shown in Figure 8.

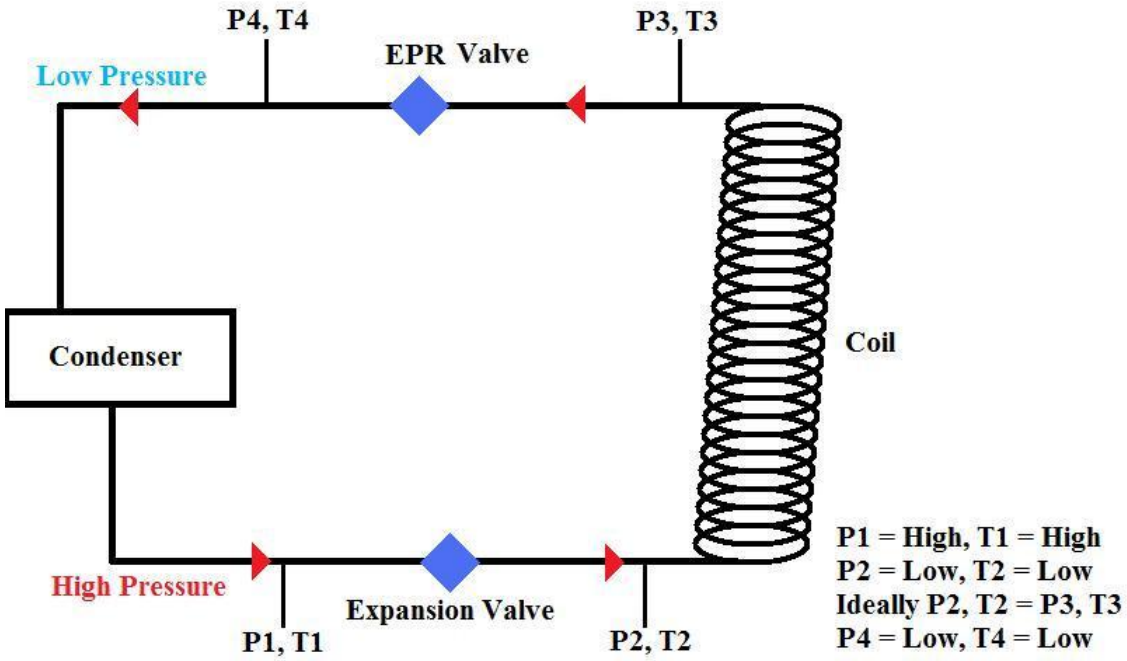


**Figure 8. Schematic of the CFDC refrigeration system, including relative pressures and temperature.**

The refrigeration system is similar to that of a residential AC system, as such the system must be evacuated and recharged when any modifications are made to the system. The following method should be used when evacuating and recharging the system:

Evacuation:

1. Connect the RED valve on the recovery tank to the RED valve on the recovery compressor, using the YELLOW high pressure line.
2. Connect the YELLOW manifold line to the BLUE valve on the recover compressor, and connect the RED line from the manifold to the high pressure side of the refrigeration system. Connect the BLUE line from the manifold to the low pressure side of the refrigeration system.
3. Ensure the CFDC refrigeration system valves are OPEN.
4. Open both the valves on the manifold. And the RED valve on the recovery tank and the RED valve on the recovery compressor.
5. Switch the recovery compressor ON and OPEN the BLUE valve slowly.
6. Pump down on the system till 10 in Hg is reached, leave at vacuum for 30 minutes.
7. Close the BLUE valve on the recovery compressor and switch OFF the recovery compressor.
8. Leave the system as refrigerant desorbs from the compressors and the vacuum decreases.

9. Switch ON the recovery compressor and slowly OPEN the BLUE valve to pump the refrigeration system down to 10 in Hg, leave for 30 minutes, CLOSE valve and switch OFF compressor. Observe vacuum.
10. CLOSE all valves when evacuation is complete.

Charging:

1. Make sure the system is under vacuum ~ 10 in Hg, if the system is not, evacuate with vacuum pump.
2. Connect the YELLOW line from the manifold to the RED valve on the SUVA 404A Tank, and the RED line of the manifold to the high pressure side of the refrigeration system and the BLUE line of the manifold to low pressure side of the refrigeration system. Place the SUVA valve on top of the scales, note tare scale.
3. Open the RED valve on the SUVA Tank, then the RED and BLUE valves on the manifold, allow the system to equilibrate.
4. Close the RED valve on the manifold.
5. Switch on the refrigeration system compressor, allow the compressor to draw in refrigerant from the low pressure BLUE manifold, monitor the scales till the desired amount of refrigerant is taken into the system. The manifold valves will also show the high and low pressure conditions.
6. Close the blue manifold valve and the SUVA tank valve.
7. Disconnect the manifold lines from the refrigeration system.

8. Run the refrigeration system and begin closing the refrigeration valves until low temperatures are met.

## 2.4 Temperature Profile of Chamber

As a good understanding of the temperature inside the chamber is essential for the calculation of ice saturation, several experimental tests were conducted to assess the chamber for thermal conductivity, hot spots, cold spots and temperature gradients due to:

- The contact between refrigerant coils and chamber wall
- Thickness of the copper walls
- Chamber construction

An additional goal of this characterization was to identify optimal placement points for operational thermocouple measurements on the operational CFDC.

A prototype test chamber was fabricated during the construction of the CFDC, this chamber was used to develop the method of winding the refrigeration coils around the inner and outer walls. The experiment to observe temperature gradient impacts was completed using this prototype chamber. Figure 9, shows the location of test thermocouples on the prototype chamber walls. Several thermocouples were mounted on the long vertical axis of both chamber walls to assess the vertical temperature gradient along the ice side of the walls. Two thermocouples were mounted a short distance apart on the ice side of the outer chamber wall, one at a point opposite where the refrigeration line is soldered to the outside of the chamber wall and one thermocouple mounted on the dead space between two refrigeration line coils to check for cold/warm spots due to the

position of the thermocouples on and off solder points of the refrigeration coils. For both the inner and outer chamber walls a cross pattern was placed near the base of the chamber to check for radial and vertical temperature gradients. In addition, on the inner wall, thermocouples were placed on the stainless steel cone at the base of the inner wall to estimate the difference in the thermal capacity of the stainless steel versus the copper walls. Finally, at the center of the cross on both walls, a thermocouple was placed on the refrigeration line side (non-ice side) of both walls. This was used to assess the variation in temperature from the active refrigeration coils on the outer wall through the wall, and then again on the inner wall. These thermocouples are marked on Figure 9 with the red and green boxes.

The refrigeration coils of the two walls were connected to two Thermo ULT 80 Chiller baths, which were circulating Syltherm XLT fluid. Next the set point temperatures of both baths were set to -20 °C and pumped throughout the chamber refrigeration coils. After the Syltherm XLT fluid within the chamber walls was brought into equilibrium the temperature measured by each of the thermocouples was recorded.

Figure 10 shows the vertical temperature profile along the ice wall side of both the inner and outer chamber. The walls are slightly warmer at the top of chamber due to the incoming relatively warmer air. At the bottom of the chamber there is large increase in the inner wall temperature, due to the high heat capacity of the stainless steel cone designed to direct air flow. Stainless steel has a higher heat capacity than copper and takes a longer time to cool.

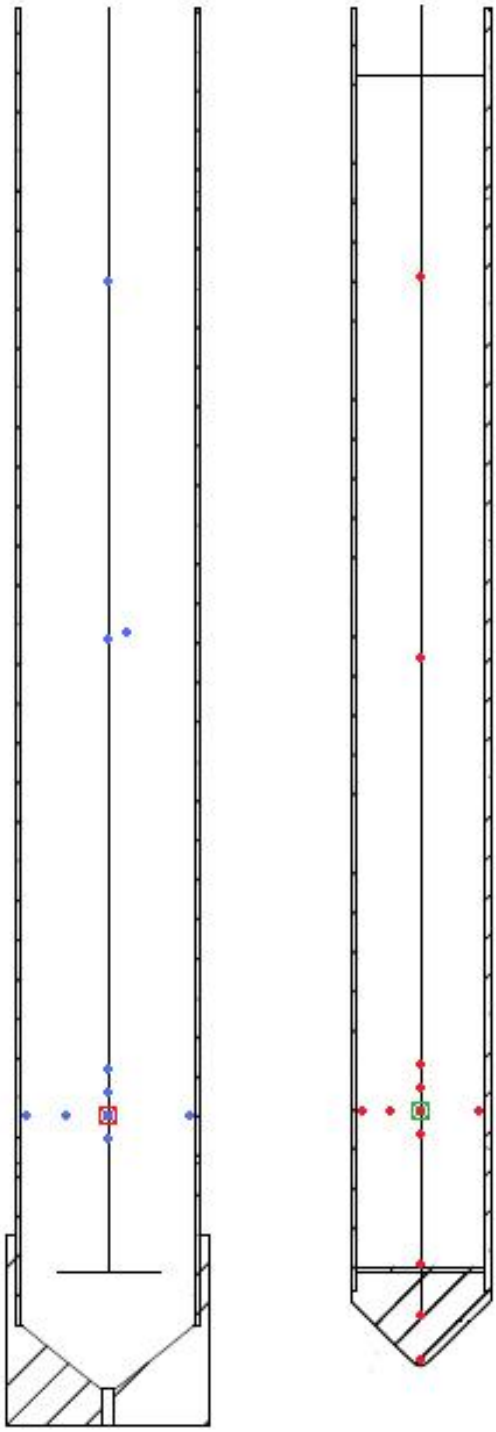

**Figure 9. Location of test thermocouples on the prototype chamber.**

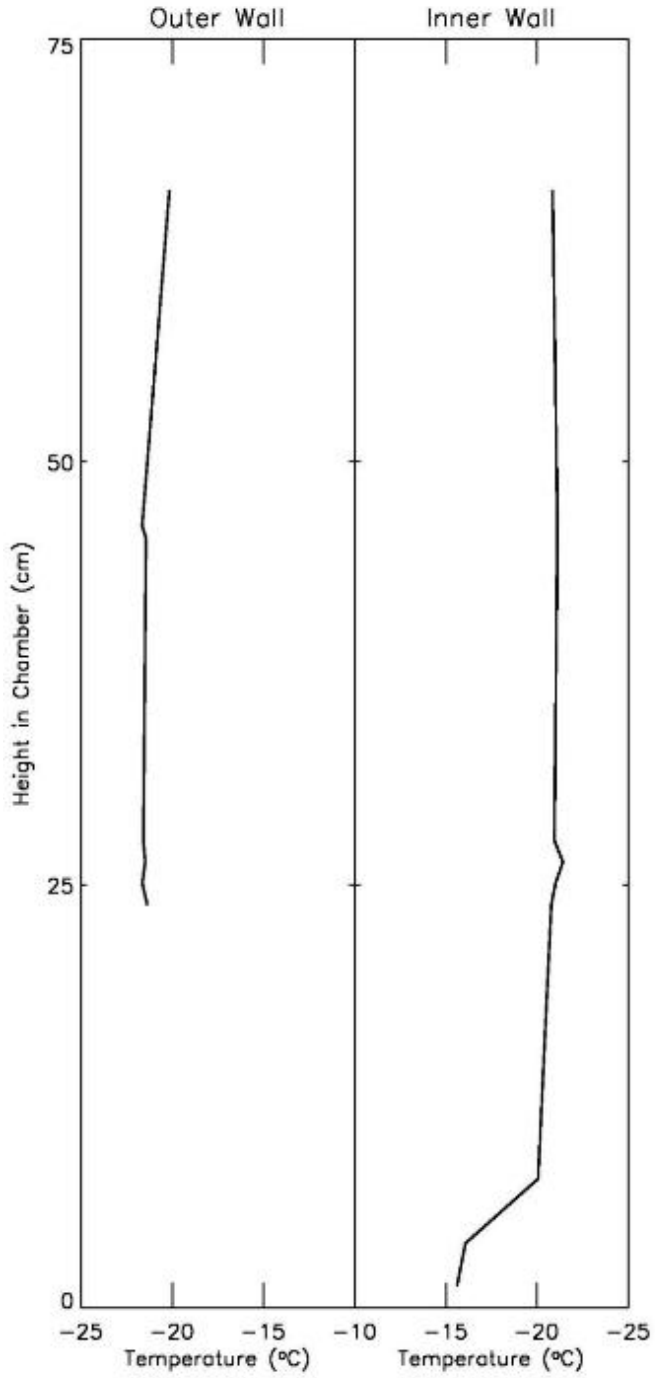


**Figure 10. Temperature profile along each wall of the chamber.**

Figure 11 shows additional results of the temperature gradient experiments, the top panel shows the temperature difference from the refrigerant coil side of the outer wall through the copper wall to the ice side of the outer wall, across the annulus volume to the ice side of the inner wall then finally through the copper wall to the refrigerant coil side of the inner wall. As the results show there is a slight difference in temperature either side of both walls of approximately ±0.5°C. The bottom panel shows the time series of all thermocouples in these experiments, generally it can be seen that the temperature is fairly constant over time for all thermocouples. However, it is clearly seen that there are two thermocouples significantly warmer than the rest, these measurements were taken on the stainless steel cone of the inner wall and show an approximate 8 °C warmer temperature.

The results of the thermocouple experiments have given some insight into the variation in temperature within the CFDC. For the operational CFDC the location of the thermocouples are shown in Figure 12. These thermocouples are not only used to measure the temperature within the chamber and derive the supersaturation and aerosol temperature, but they are also used to "drive" the CFDC and the data from each thermocouple is integrated into the labview software using the NI data acquisition system to control the valves used in the refrigeration system.

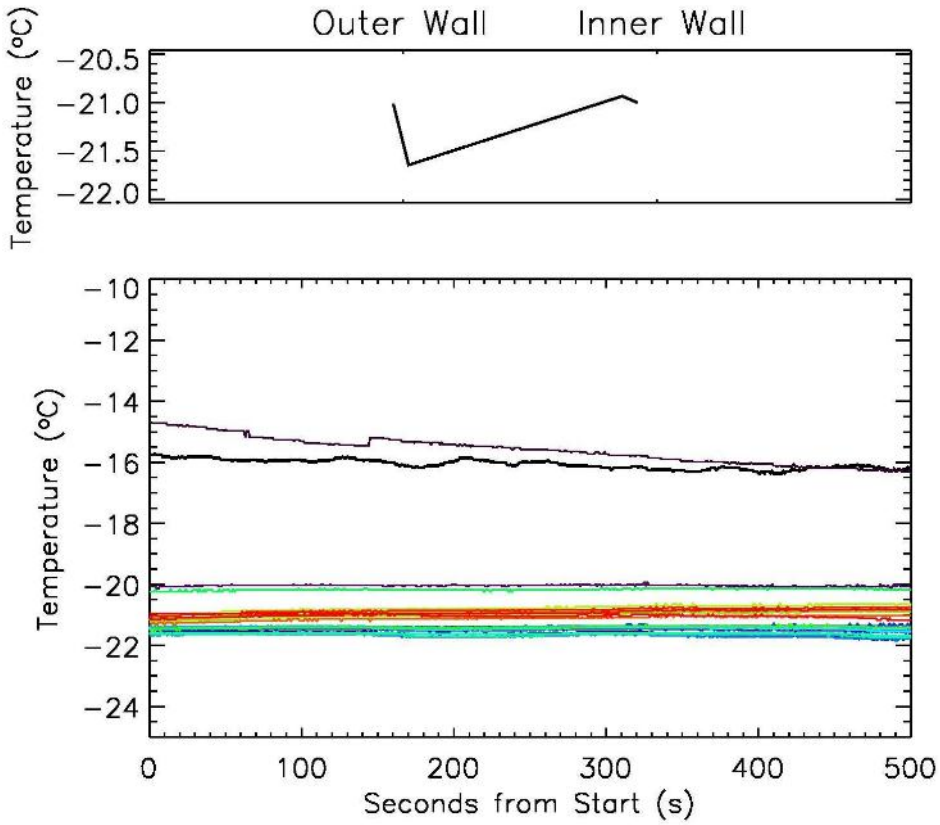


**Figure 11. Top plot is the temperature gradient through the thickness of the chamber walls. Bottom plot is the temperature time series for this test.**

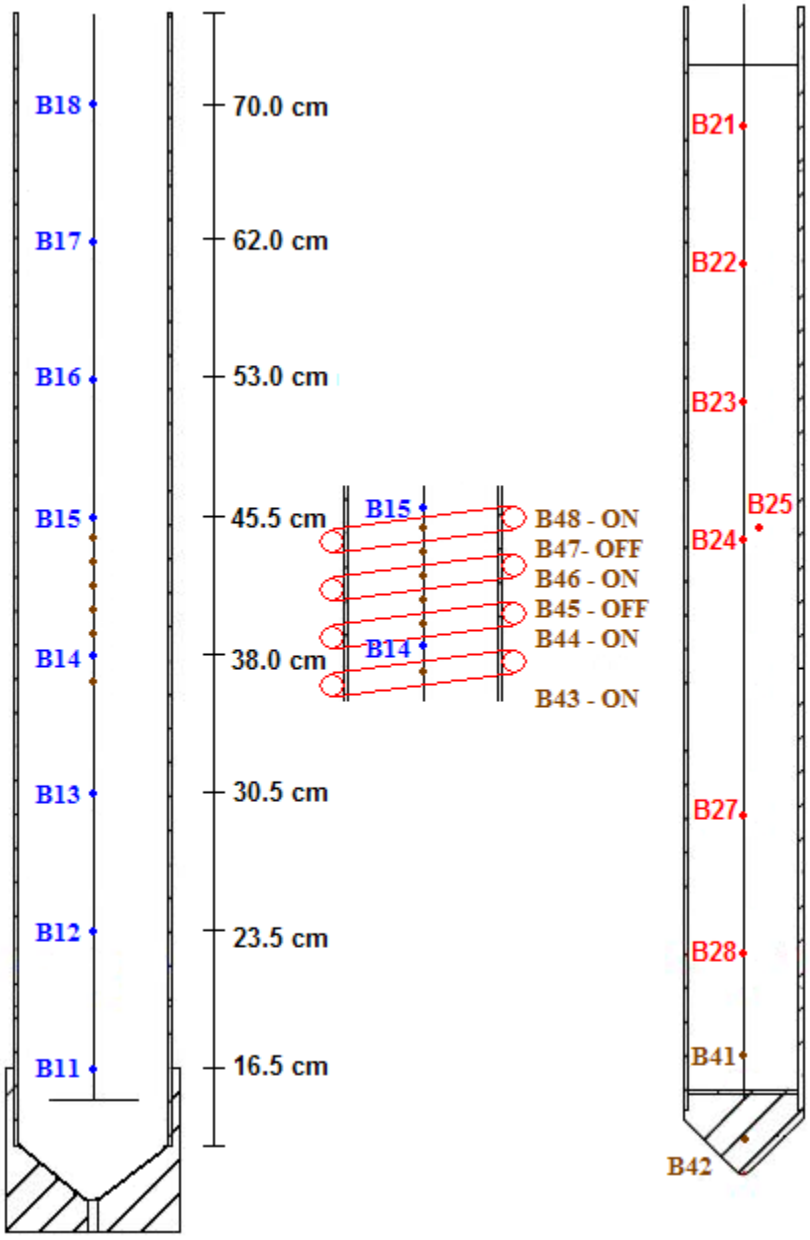


**Figure 12. Position of the thermocouples on the operational instrument. 6 additional thermocouples were added to measure on and off coil temperatures.**

2.5 Cyclone Impactor

A BGI Sharp Cut Cyclone (SCC) 0.732 sharp cut cyclone impactor is utilized directly up stream of the CFDC (Figure 3) to remove particles larger than a specified size, which is dependent on the flow rate passing through the cyclone. The cyclone removes any large particles by inertial separation, which stops them from entering into the CFDC so that they are not mistakenly counted as activated IN crystals by the OPC. Figure 13 shows the cut point diameter curve for the cyclone used on the inlet of the CFDC. For typical operational conditions, the sample flow rate entering the CFDC is between 1.6 and 1.8 L $min^{-1}$. This corresponds to a cut point diameter of 1.1 to 1.3 μm.

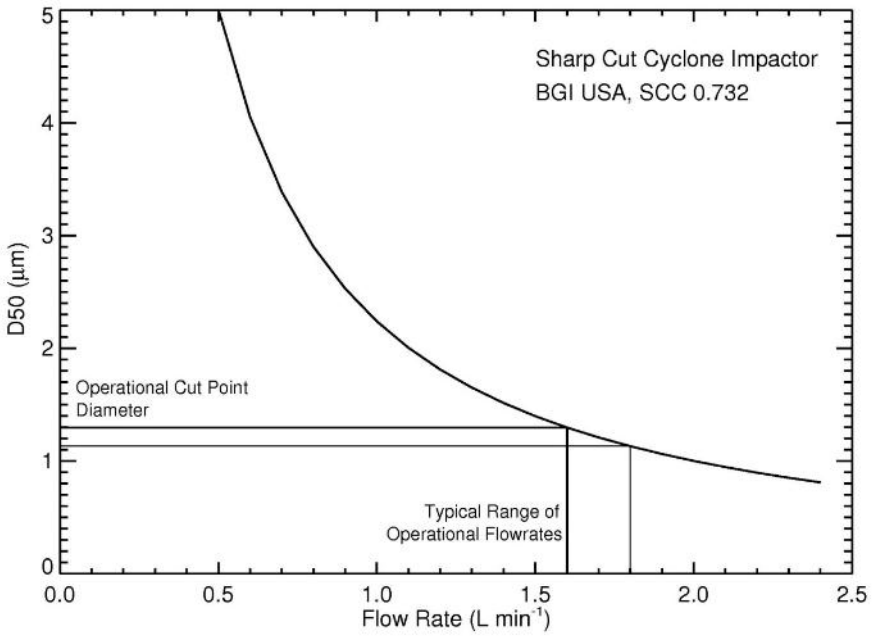


**Figure 13. Cut point diameter as a function of flow rate for the cyclone attached in line up stream of the chamber.**

## 2.6 Residence Time

The residence time of aerosol particles within the chamber was determined experimentally for the typical operational total flow rate of 8.0 L/min and sample flow rate of 1.6 L/min. This experiment was conducted using a TSI Condensation Particle Counter (CPC) 3025A to measure the total concentration exiting the base of the CFDC. A polydisperse distribution of ammonium sulfate particles were generated using a TSI 3076 Atomizer, these particles were dried using a desiccant dryer and then size selected by a TSI 3080 Electrostatic Classifier (EC) to produce a monodisperse size distribution. The monodisperse aerosol stream then entered a mixing chamber to reduce the total flow by directing it to a filtered exhaust and reduce the system pressure before entering the CFDC. The CFDC was also connected to the mixing chamber and air was sampled through the CFDC, initially the CFDC was set to filtered bypass, so no particles entered the chamber. Once a baseline was established for the filtered air, a 5 second injection of particles from the mixing chamber occurred. The CPC was then monitored to observe when the particles traveling through the CFDC arrived at the CPC. The results from this study are shown in Figure 14.

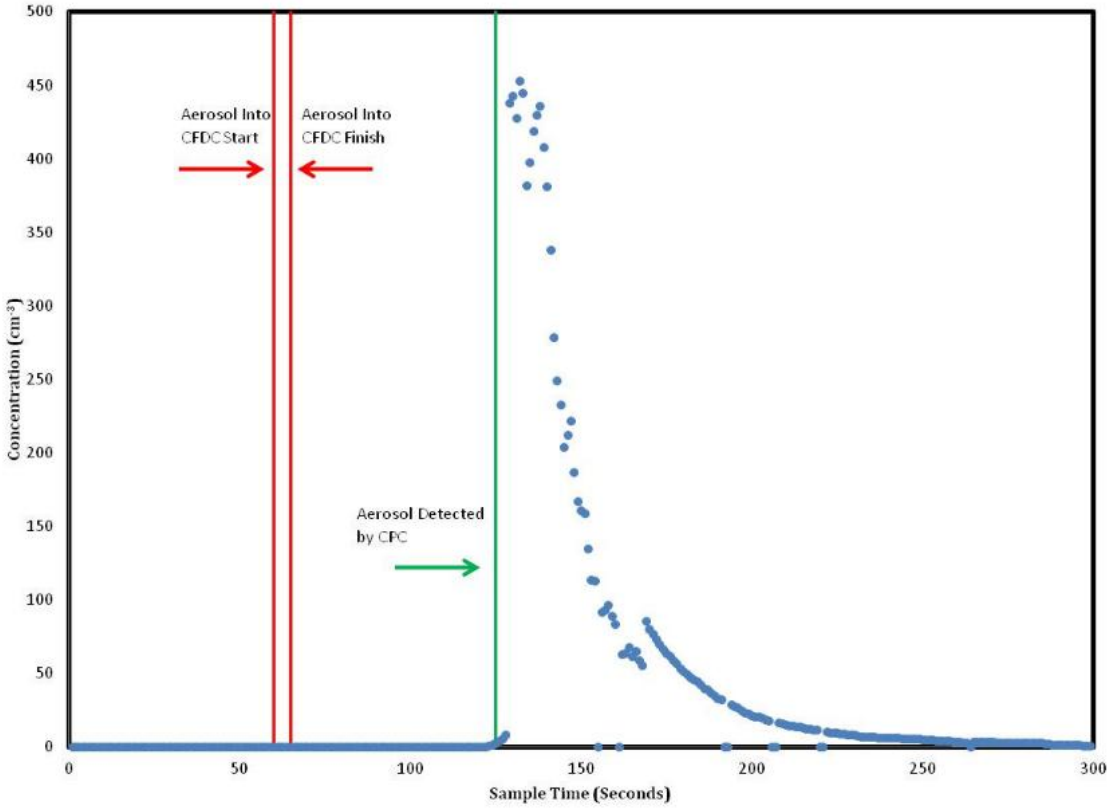


**Figure 14. Measured residence time of particles traveling through the CFDC. The red lines indicate aerosol injection period, green line indicates the start of CPC detection of particles.**

## 2.7 Pre-cooler Development

During laboratory experiments it was noted that the inlet manifold of the CFDC often froze due to the relatively humid air stream entering the chamber from the particle generating process. A pre-cooler instrument was developed to reduce the temperature of the aerosol entering the CFDC and remove any remaining water condensed on particles after atomization. A Solidworks schematic of the pre-cooler is shown in Figure 15. The

aerosol stream enters the pre-cooler traveling through a stainless steel tube. This tube is surrounded by an acrylic tube sheath which contains chilled Syltherm XLT fluid, the fluid is circulated throughout the sheath by an independent chiller bath. The pre-cooler response curve as a function of pre-cooler temperature are shown in Figure 16, the pre-cooler was set to three temperatures to test the response in relative humidity reduction. The set point temperatures for the pre-cooler were 10 °C, 0 °C and -10 °C, the relative humidity was measured on the sample inlet and the exhaust on the pre-cooler using two RH probes. The sample flow rate through the pre-cooler was controlled at 2 L/min with the variation in the air sample humidity provided by a dry air and bubbler system. For a pre-cooler temperature of 10 °C the results show that over the range of test inlet humidity's (20 % through 70 %) the exhaust humidity can be reduced to 40 %. At 0 °C set point temperature the exhaust RH can be reduced down to approximately 20 % for inlet humidity's up to 70 %, finally for a set point temperature of -10 °C the exhaust RH can be reduced down to approximately 10 %. For all laboratory tests henceforward using the pre-cooler, a set point temperature of -10 °C will be used.

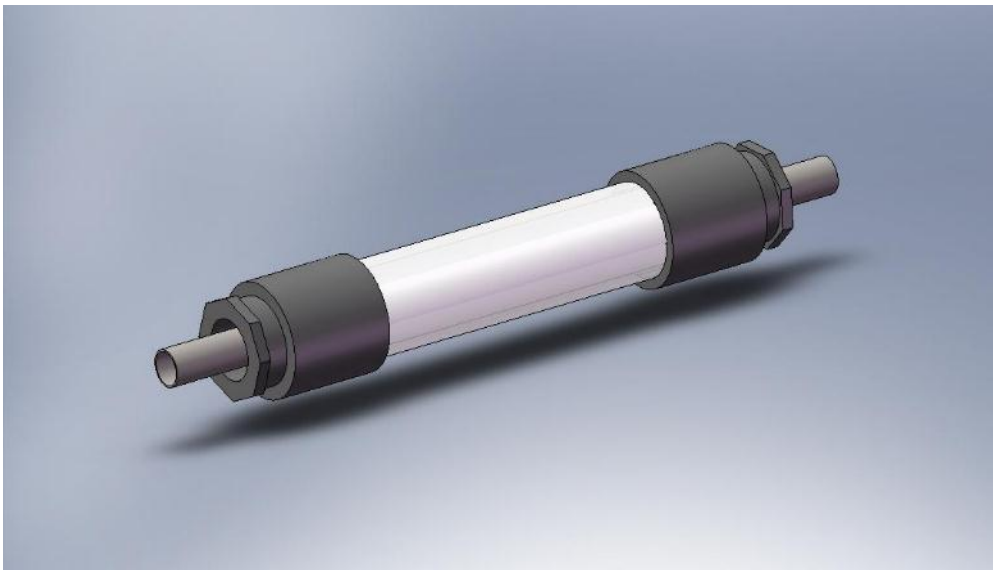

**Figure 15. Solidworks schematic of the pre-cooler.**

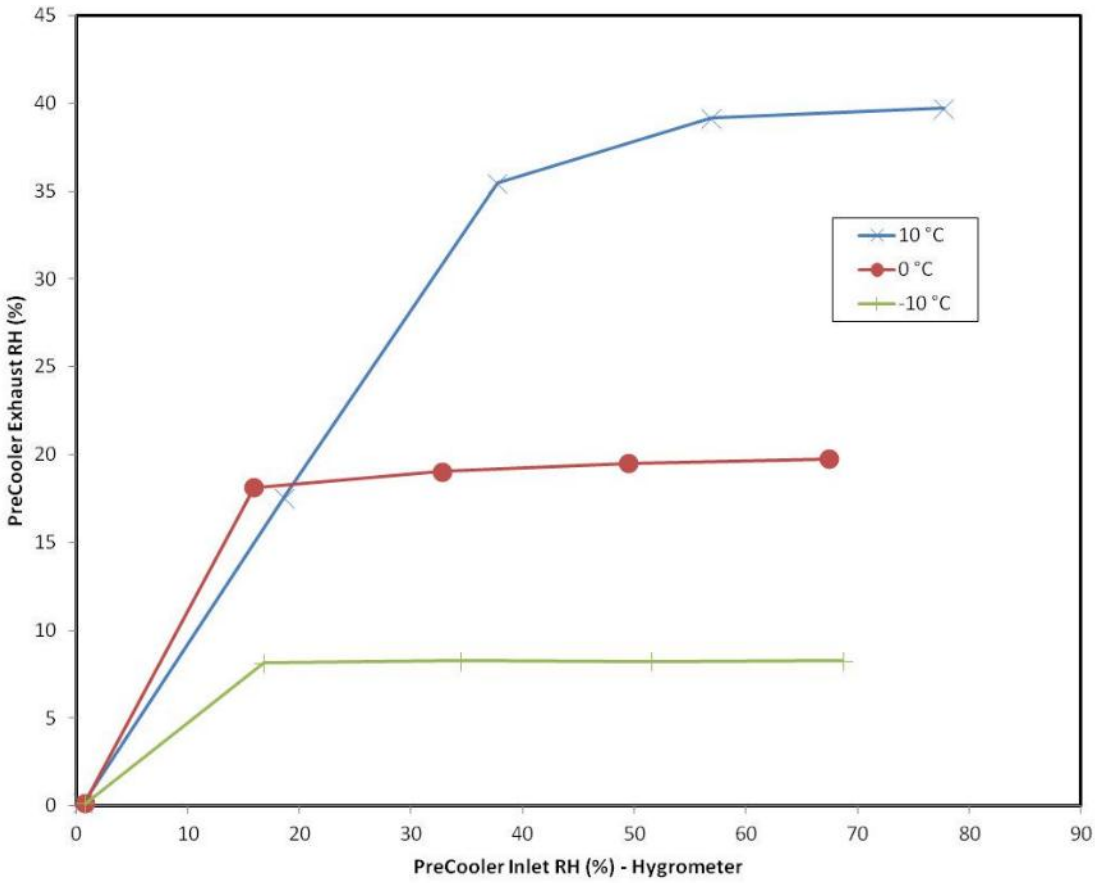


**Figure 16. Response curves for pre-cooler exhaust relative humidity as a function of inlet relative humidity and temperature.**

## 2.8 CFDC Characterization

After the CFDC was constructed measurements of the ice nucleation ability of various particles were completed as part of the instrument characterization. This study was designed to identify typical supersaturation and temperature conditions under which IN particles nucleate and produce ice crystals. The setup for these experiments is shown in Figure 17. A polydisperse distribution of aerosol particles was generated using a TSI

3076 Atomizer. The aerosol stream from the atomizer then passed through a desiccant dryer to remove water from the particles within the distribution. The now dried polydisperse distribution enters a small mixing chamber which has an additional intake of dry compressed nitrogen with a flow rate of 2 L/min, this air stream further dries out the polydisperse particles and also acts to dilute the number concentration of particles within the air stream. A HEPA filtered exhaust line is attached to the small mixing chamber, allowing for a reduction in pressure of the system by removing excess air. A separate exhaust port on the small mixing chamber is used to direct the diluted dry polydispersed air to a TSI 3080 Electrostatic Classifier (EC). The EC produces a monodisperse distribution of particles of one particular diameter based on the electrostatic mobility of the particles within the incoming polydispersed distribution. The diameter of the particles generated by the EC are in the sub-micron range. The size selected classified particles then pass through the pre-cooler which is set to a cooling temperature of -10 °C. After passing through the pre-cooler the particles are injected into a larger mixing chamber, this chamber has an additional inlet with a HEPA filter to provide pressure relief within the system. The CFDC and a TSI 3025A Condensation Particle Counter (CPC) then draw sample air from the mixing chamber at a flow rate of 2 L/min and 1.5 L/min respectively. The CPC provides a total concentration of particles within the chamber and the CFDC potentially activates these particles depending on the operational conditions within the chamber.

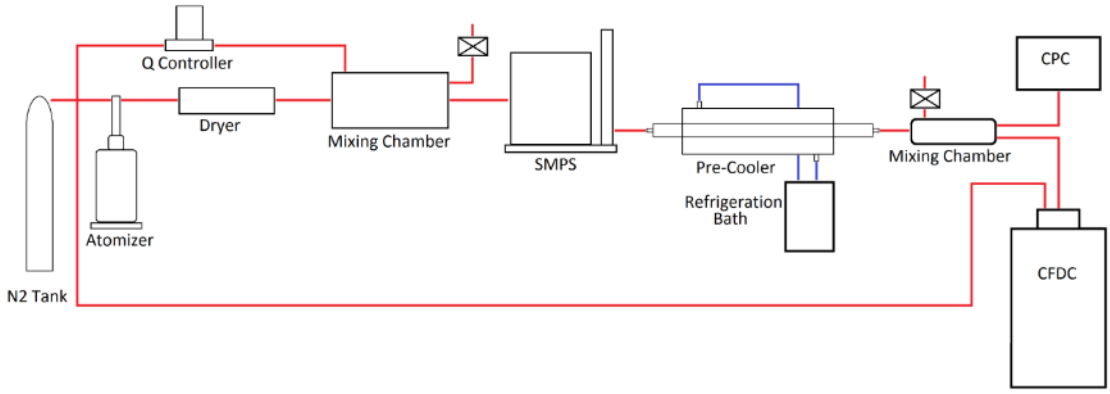


**Figure 17. Experimental setup for CFDC ice nucleation calibration.**

An example of the results for the instrument characterization are shown in Figure 18. A solution of silver iodide and ammonium sulfate was used in the atomizer and the EC was set to classify particles into a monodisperse distribution centered on a diameter of 90 nm, using a sheath flow rate of 8 L/min and a sample flow rate of 0.8 L/min. The pre-cooler was set to an operational temperature of -10 °C. The results of several ice nucleation experiments are shown in Figure 18, these experiments were conducted for ice nucleation temperatures ranging from -25 °C down to -36 °C, and supersaturations with respect to ice ($SS_{ice}$) from 0 % to 35 %. Panel A of Figure 18 shows the concentration of activated IN as function of $SS_{ice}$ (colored stars). The color of the symbols indicate the temperature of the aerosol stream where nucleation occurred. Each data point shown is for the total number of ice crystals measured in a fixed period of 3 minutes. In addition, the average concentration of condensation nuclei as measured by the CPC (red diamonds) is also shown for the same measurement periods. As the figure shows, the concentration of nucleated ice crystals increases with increasing $SS_{ice}$.

However, there is no observable correlation between the IN concentration with the aerosol temperature. Panel B of Figure 18 shows the IN/CN ratio as a function of $SS_{ice}$, this parameter gives a better indication of the nucleation ability of these particles by normalizing the activated IN concentration to the total aerosol concentration. The nucleation observed during these experiments likely occurred through depositional and condensation freezing mechanisms.

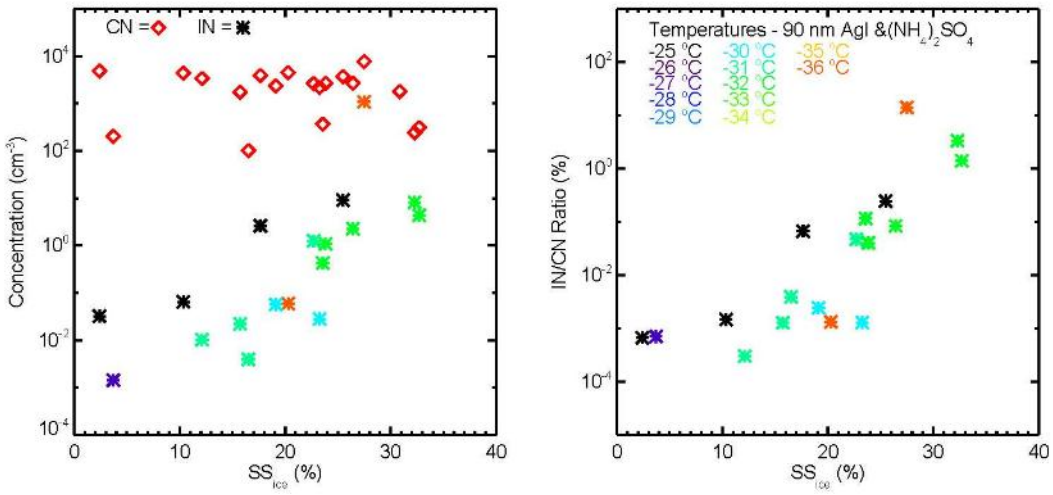


**Figure 18. Silver iodide ice nucleation measurements.**

# 3. ICE NUCLEATION IN THE ARCTIC

Aerosol-cloud interactions are not well understood especially in mixed phase and fully glaciated clouds found in the polar atmosphere. Compared to warm clouds, the interactions in mixed phase and ice clouds between aerosol, liquid water droplets and ice crystals are more complex. The concentration of Ice Nuclei (IN) in polar regions is typically very low, making accurate IN measurements challenging (Prenni et al., 2008; Verlinde et al., 2007). The North Slope, Alaska (NSA) is an optimum location for the measurement of stratifrom mixed phase and fully glaciated clouds, this region also has a strong seasonal variation in aerosol concentration and type. Previous measurement of Arctic IN concentrations have shown a large variation in both spatial and temporal dimensions (McFarquhar et al., 2011; Prenni et al., 2006; Prenni et al., 2008; Rogers et al., 2001a; Verlinde et al., 2007). In addition, there is a lack of convincing evidence on the cause of these variations and whether fundamental particle properties such as chemistry or size of the aerosol dominate these changes.

One of the previous studies conducted in the Arctic was the Mixed-Phase Arctic Cloud Experiment (M-PACE) located near Barrow, AK and took place during the fall 2004 (Prenni et al., 2008; Verlinde et al., 2007). At this time of the year the North Slope Region of the Arctic is considered "pristine" with very few cloud drops observed. During the M-PACE campaign there were approximately 10 instruments on board the University of North Dakota, Citation aircraft, measuring the atmospheric state, aerosol properties and cloud microphysics.

## 3.1 Indirect and Semi-direct Aerosol Campaign

The Indirect Semi-Direct Aerosol Campaign (ISDAC) took place in April 2008, in the vicinity of the ARM Climate Research Facility (ACRF), Barrow, Alaska. The CFDC, along with a suite of other atmospheric instruments (~40 instruments in total) were onboard the NRC Convair 580 aircraft, which flew 29 sorties from Fairbanks, Alaska to and around the ACRF site at Barrow. ISDAC was the first field campaign for the Texas A&M CFDC instrument (McFarquhar et al., 2011). These instruments measured the atmospheric state, the aerosol properties, cloud microphysics and the radiative budget of the atmosphere. This chapter focuses on the IN measurements made by the Texas A&M Continuous Flow Diffusion Chamber (CFDC) during ISDAC.

The Intense Observation Period (IOP) of ISDAC was in the Arctic spring season, during which time the Arctic region was expected to be much more polluted than during the fall season during which the M-PACE project occurred. The increased pollution originates due to significant emissions from biomass burning in both Asia and Alaska at this time of year. At the start of the ISDAC the Beaufort Sea was packed with sea ice, which slowly broke up over the course of the field project.

There were four primary science questions addressed during ISDAC (McFarquhar et al., 2011):

1. How do properties of the arctic aerosol during April differ from those measured during the M-PACE in October?

2. To what extent do different properties of the arctic aerosol during April produce differences in the microphysical and macrophysical properties of clouds and the surface energy balance?
3. To what extent can cloud models and the cloud parameterizations used in climate models simulate the sensitivity of arctic clouds and the surface energy budget to the differences in aerosol between April and October?
4. How well can long-term surface-based measurements at the ARM Climate Research Facility provide retrievals of aerosol, cloud, precipitation, and radiative heating in the Arctic?

The CFDC instrument provides critical support for goals 1 and 2 of the list of ISDAC science questions. In addition, two CFDC specific goals were also proposed:

5. Identify extreme ice nucleation events and under what conditions they occur?
6. Can the main forcing of ice nucleation be identified, and thus be used to predict ice nucleation - composition versus particle size.

The CFDC was located inside the aircraft. Two inlets were mounted to the fuselage of the Convair 580 aircraft, one is a direct aerosol sampling inlet and the second is a Counterflow Virtual Impactor (CVI). These inlets and the instruments each inlet is connected too are shown in Figure 19. Switching between inlets was determined by the flight manager and was typically done during the transitioning from clear air (aerosol inlet) to cloud (CVI). The air stream travels from the inlets to the suite of instruments sampling from that line. Upstream of the CFDC, the incoming airstream passes through

a cyclone impactor to prevent particles with D > ~1.5 μm from entering into its chamber. The airstream is then exposed to the chosen operating conditions. All particles which have nucleated and grown to be ice crystals with D > 5 μm within the chamber are counted at the base of the CFDC by the OPC.

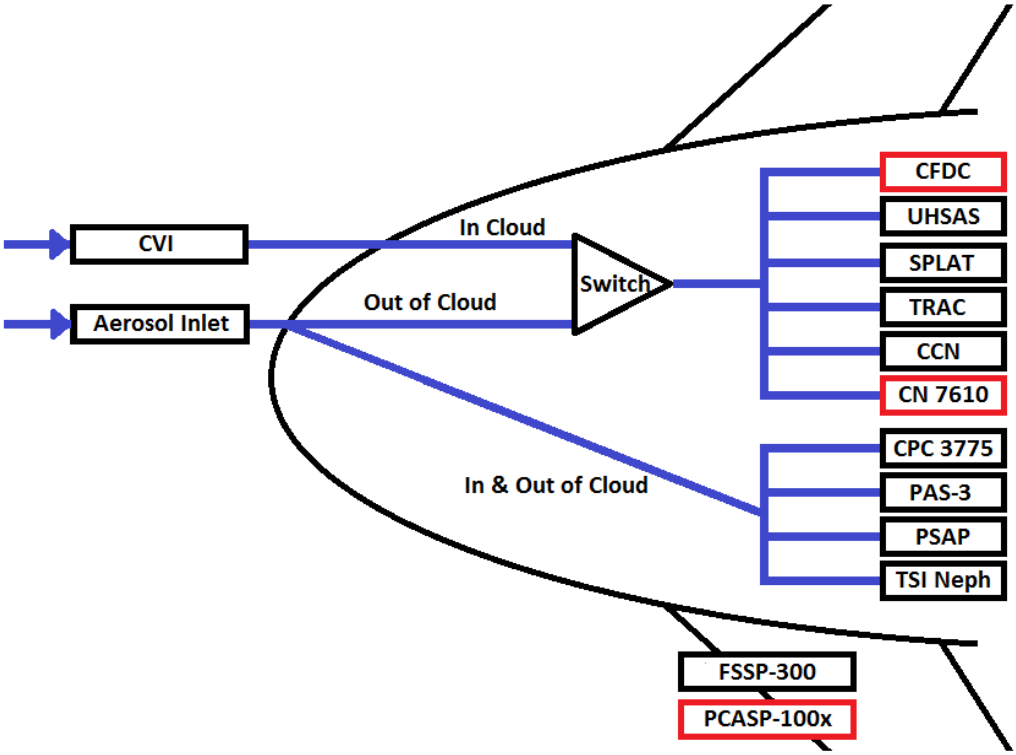


**Figure 19. Schematic of the instruments and inlets onboard the Convair 580 aircraft.**

## 3.2 Indirect and Semi-direct Aerosol Campaign – Overview

The ISDAC was a very successful first deployment of the CFDC. Unlike many other instruments onboard the Convair 580 aircraft, the CFDC was in operation for every sortie which occurred during the project. The CFDC successfully measured IN concentrations over a broad range of instrumental operating conditions, ambient environmental conditions and aircraft maneuvers.

An overview of the average IN concentration measured during the ISDAC project for all flights between 8 and 28 April is shown in Figure 20 and published in McFarquhar et al. (2011). The data has been filtered to show only data collected when sampling from the ambient inlet. Four data sets are shown, the upper average IN concentrations below water saturation (−10% to 0% $SS_w$) (solid diamonds) and above water saturation (0% to +10% $SS_w$) (solid triangles). In addition the lower average IN concentration for both below water saturation (−10% to 0% $SS_w$) (open diamonds) and above water saturation (0% to +10% $SS_w$) (open triangles) are also shown. The data collected by the CFDC during times where the IN concentrations are below the CFDC detection threshold are not included in the calculated averages shown in Figure 20, these averages represent the upper limit of the CFDC measured IN concentration. The lower limit of the IN concentration is calculated by assuming a concentration of zero for any measurements made below the instrument detection limit. The sorting by water saturation allows the differentiation of the results by heterogeneous nucleation mechanisms, data collected below water saturation (−10% to 0% $SS_w$) represents ice

crystals formed by deposition freezing whereas data collected above water saturation (0% to +10% $SS_w$) include all ice crystals nucleated by immersion, condensation and depositional freezing. It is unlikely that contact freezing will occur within the CFDC as the flow through the instrument is laminar and no internal mixing will occur. The results were also filtered to only include IN concentrations which occurred when the CFDC aerosol processing temperature was between -10 °C and -30 °C. The results show that there is a large variation in IN concentration under the different nucleation conditions, from 0.001 $L^{-1}$ up to ~ 20 $L^{-1}$. In some cases there were short time periods where the IN concentration was as high as 100 $L^{-1}$. Significant IN concentrations were observed with $SS_{water}$ below 0 % indicating that depositional nucleation was occurring. In addition, nucleation was often higher for $SS_{water}$ above 0 %, which is expected due the additional nucleation mechanisms which can occur under these conditions. However, the nucleation could not be strictly related to the individual freezing mechanism due to the high variability in operating conditions.

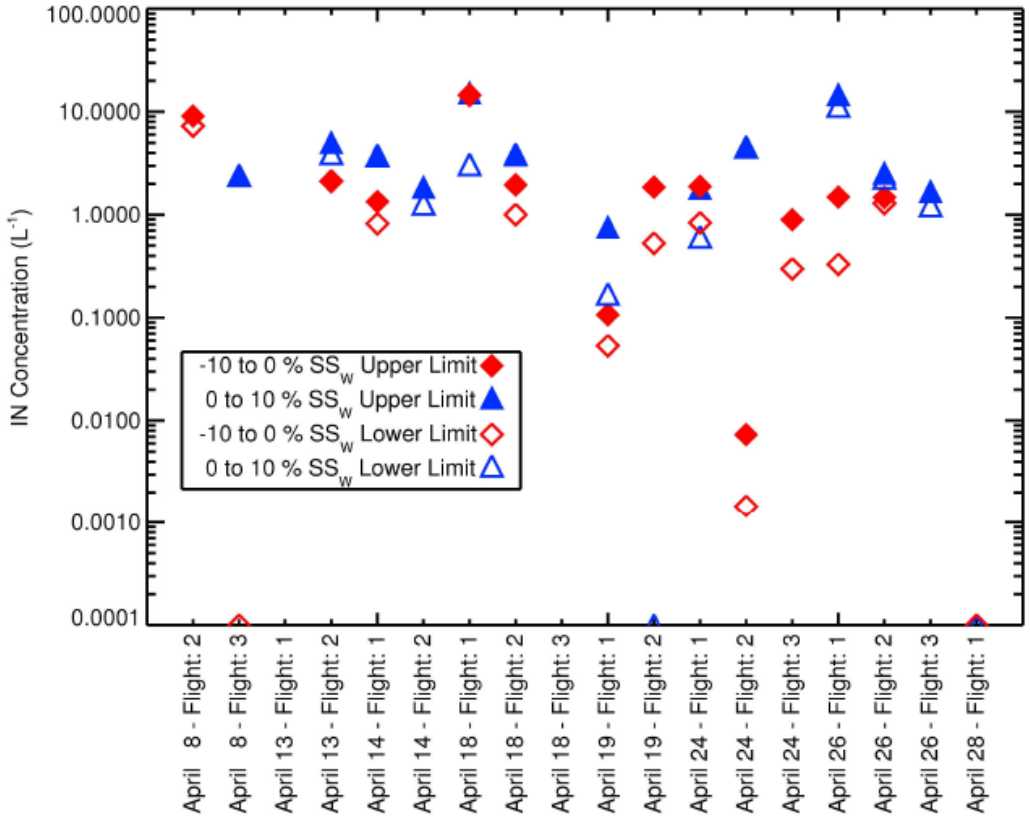


**Figure 20. Average IN concentrations measured below (solid diamonds; from −10 % to 0 % $SS_{water}$) and above water saturation (triangles; from 0% to +10% $SS_{water}$) as function of flight number. In addition, lower limits to the IN concentrations below (open diamonds; from −10% to 0% $SS_{water}$) and above-water saturation (triangles; from 0% to +10% $SS_{water}$) are shown. Data in the figure were collected by sampling on the ambient inlet during clear-air conditions (McFarquhar et al., 2011).**

## 3.3 Indirect and Semi-direct Aerosol Campaign – Extreme Events

The overview of the data (Figure 20) collected during ISDAC depicts high variation in ice nucleation throughout the Arctic region. In addition, IN concentrations in the Arctic are very low, making accurate IN measurements a challenge. The data provide

initial interpretation of extreme ice nucleation events in the Arctic spring, partially satisfying Goal 5 listed above. However, it does not examine the forcing behind the nucleation events, and the question posed in Goal 6 still remains: "Can the main forcing of ice nucleation be identified, and thus be used to predict ice nucleation - composition versus particle size". In order to answer this question, each aircraft sortie was analyzed and a time series of the total IN concentration, nucleation temperature and supersaturation was produced. The size distribution measured by the PCASP and cloud phase as determined by the methods discussed in (McFarquhar et al., 2007), were synchronized with the CFDC data and compared to the CFDC IN concentrations. A number of sorties were identified from the full ISDAC campaign which showed a strong correlation between high ice nucleation concentrations and either change in particle size or a change in composition and are listed in Table 1. Three of these sorties were of particular interest and are highlighted in green in Table 1, these interesting events were all sampled through the ambient aircraft inlet during ambient air (flight 31), liquid phase cloud (flight 25) and fully glaciated cloud (flight 24) events.

**Table 1. Summary table of ISDAC sorties and ice nucleation conditions and potential forcing.**

| Flight Number | Cloud Phase | Inlet Type | Altitude (m) | Water Saturation Condition | | Potential Forcing |
|---|---|---|---|---|---|---|
| 16 | Mixed | CVI | < 2000 | -10 % < SS < 0 % | | Size |
| 19 | Ice | CVI | 4000 - 6000 | -10 % < SS < 0 % | 0 % < SS < 10 % | No PCASP |
| 23 | Ice | CVI | 4000 - 6000 | | 0 % < SS < 10 % | Size |
| 23 | Mixed | CVI | 4000 - 6000 | -10 % < SS < 0 % | 0 % < SS < 10 % | Size |
| 24 | Ice | CVI | > 6000 | -10 % < SS < 0 % | | Composition |
| 24 | Ice | Ambient | > 6000 | -10 % < SS < 0 % | 0 % < SS < 10 % | Composition |
| 25 | Liquid | Ambient | ≈ 1500 | -10 % < SS < 0 % | | Size |
| 27 | Ice | CVI | ≈ 2000 | | 0 % < SS < 10 % | Composition |
| 28 | Ice | CVI | 1500 - 4000 | -10 % < SS < 0 % | 0 % < SS < 10 % | Composition |
| 29 | Ice | Ambient | 2000 - 3500 | | 0 % < SS < 10 % | Composition |
| 31 | Clear | Ambient | ≈ 1000 | -10 % < SS < 0 % | | Composition |
| 31 | Mixed | CVI | < 1000 | -10 % < SS < 0 % | 0 % < SS < 10 % | Size |
| 32 | Ice | CVI | > 6000 | | 0 % < SS < 10 % | Size |
| 33* | Clear | Ambient | < 2000 | -10 % < SS < 0 % | | Conditions |
| 33 | Mixed | CVI | ≈ 2000 | | 0 % < SS < 10 % | Conditions |

* Homogeneous Flight

The time series for each of the three highlighted flights are shown in Figure 21, Figure 23 and Figure 25. The IN concentration (purple diamonds) is shown in the top panel of each figure, additionally shown in this panel are the cloud phase (black triangles) and the cumulative PCASP size distribution for particles larger than 0.124 μm (red solid line), 0.459 μm (green solid line) and 0.939 μm (blue solid line). The middle panel shows the altitude of the aircraft (black solid line) and the IN/CN ratio (black stars), providing an indication of the fraction of total aerosol particles which have nucleated. The bottom panel shows the operating conditions of the CFDC, the $SS_{ice}$ (purple solid line), $SS_{water}$ (red solid line) and the aerosol temperature within the chamber (blue solid line).

During flight 34 of ISDAC the aircraft flew through a plume of aerosol during a clear air transect. This plume of aerosol had a very different composition to the surrounding air mass and was preferential for ice nucleation. This high nucleation event can be seen in the time series of IN concentration (purple diamonds) between 00:02 UTC and 00:07 UTC in the top panel of Figure 21. During this period the IN concentration increases dramatically from around 1 $L^{-1}$ to approximately $1x10^4$ $L^{-1}$, however, the PCASP size distribution shows no change in the respective particle concentration of the 0.124 μm, 0.459 μm and 0.939 μm particle diameters. In addition, the aircraft was traveling on a constant altitude leg, the $SS_{ice}$ is approximately 35 % and the aerosol nucleation temperature averaged approximately -25°C. The full aerosol size distributions as measured by the PCASP and the CFDC OPC are shown in Figure 22 for 1 minute intervals of the high IN event. As the figures show the PCASP size distribution

remains relatively constant over the interval, while the CFDC OPC data shows no nucleation occurring prior to entering the plume at 00:02 UTC, but by 00:04 UTC a broad distribution of activated IN particles measured by the OPC can be seen, these activated IN particles quickly disappear as the aircraft exits the plume around 00:07 UTC. As the PCASP measured size distributions shows no change in the particle size distribution during this nucleation interval, the high nucleation event can be attributed to a change in the composition of the aerosol within the plume transected by the aircraft.

The second example of a high ice nucleation event is for Flight 24 in which the aircraft was on a transit leg from Barrow, AK to Fairbanks, AK. The time series of the high IN event is shown in Figure 23 and occurred between 01:40 UTC and 01:45 UTC, shortly after reaching a cruising altitude of 7000 m. During this time the aircraft was located within a fully glaciated cloud and was sampling using the ambient aerosol inlet. Therefore any ice crystals entering the aircraft inlet were heated, melted and the liquid water evaporated leaving the ice crystal residual behind. As Figure 23 shows, the total IN concentration reaches a maximum of approximately $1x10^4$ $L^{-1}$ during the event, while the PCASP size distribution remains constant. However, during this event the CFDC operation conditions were not in a steady state, with both the $SS_{ice}$ and $SS_{water}$ increasing while the CFDC processing temperature was cooling to approximately -30 °C. The increase in chamber saturation typically allows for an increase in the potential for IN to nucleate, which may of contributed to the high nucleation event. However, the peak IN concentration quickly drops back down to background levels while the $SS_{ice}$ and $SS_{water}$ are still increasing, indicates that more than just the CFDC operating conditions are

forcing the nucleation event. Again the 1 minute average PCASP size distributions measured during the nucleation event can be compared to the CFDC OPC size distribution (Figure 24). The PCASP data shows a relatively constant size distribution across the size range from 0.1 μm to 5 μm over the period of the nucleation event (01:40 to 01:45 UTC). The CFDC OPC shows the activation of very few particles, at 01:40 UTC, then as the aircraft enters the plume the sampled aerosol particles begin to nucleate as shown in the broadened distribution of ice crystal sizes at 01:41 UTC. The activation of these IN continues through 01:44 UTC with increasingly larger ice crystals being generated. As the aircraft exits the plume the CFDC activated ice crystal distribution drops to zero. This data again indicates that the ice nucleation occurring during this event was driven by the composition of the preexisting IN which were removed from any ice crystals occurring in the atmosphere by evaporation as they passed through the ambient air inlet prior to entering the CFDC.

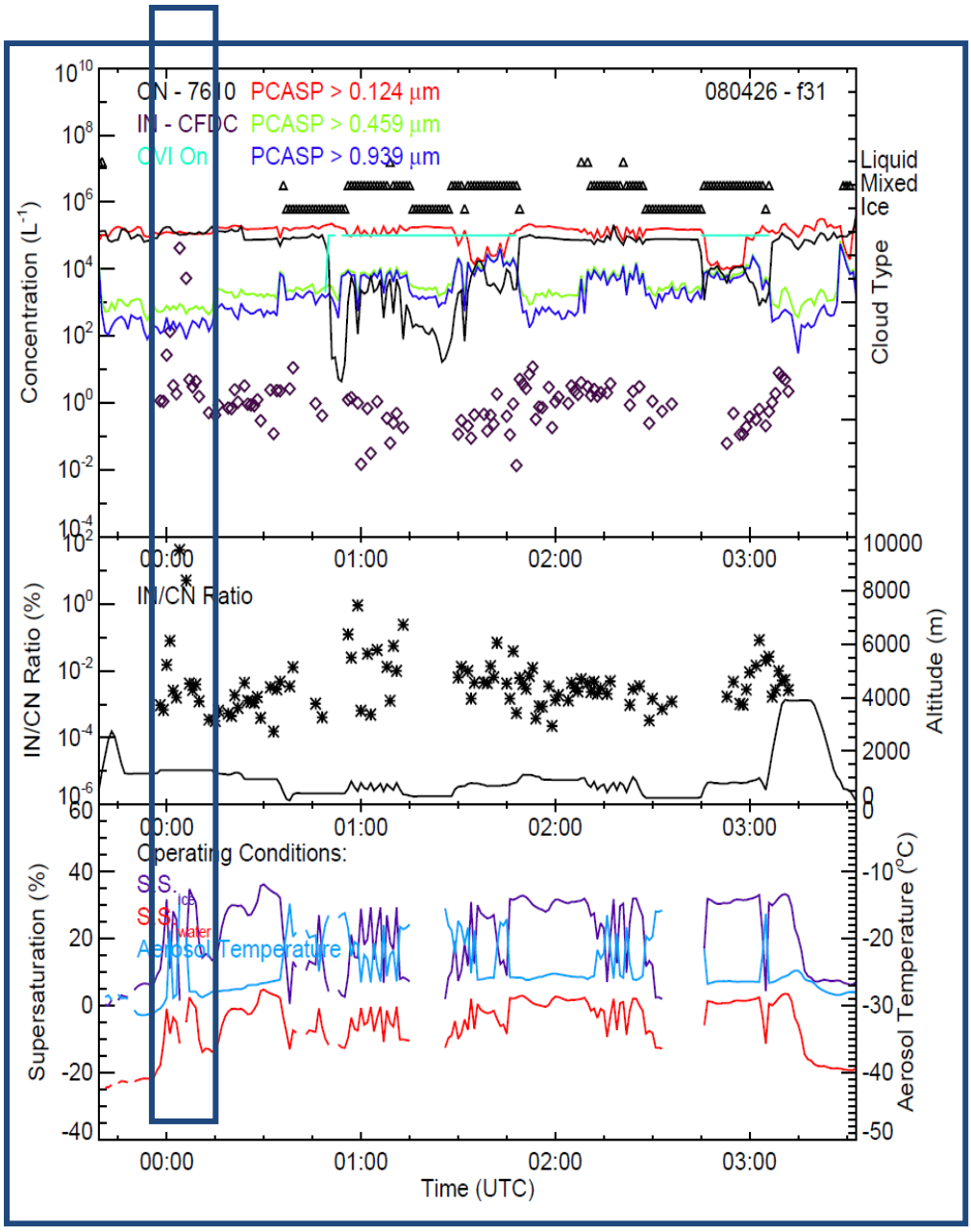


**Figure 21. Time series of IN concentration, PCASP size distribution, cloud phase, altitude, and CFDC operating conditions for flight 31.**

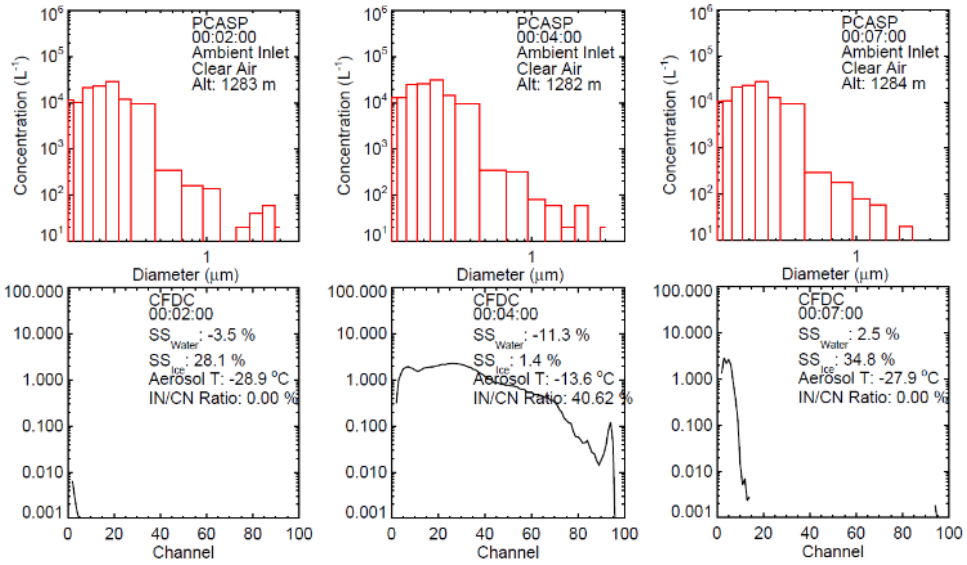


**Figure 22. Full aerosol size distributions measured by the PCASP (top panels) and the CFDC Climet (bottom panels) for clear air during flight 31.**

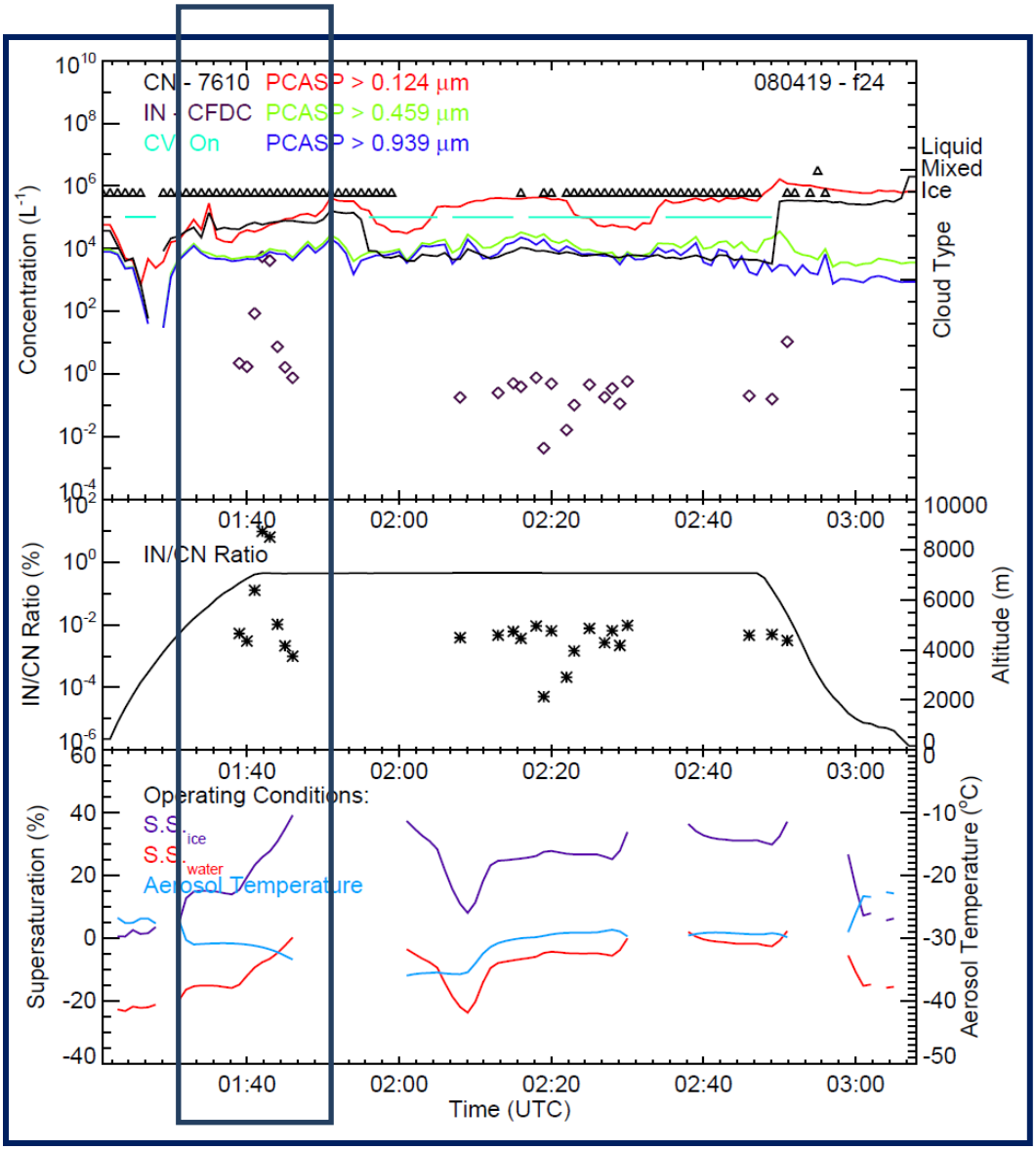


**Figure 23. Time series of IN concentration, PCASP size distribution, cloud phase, altitude, and CFDC operating conditions for flight 24.**

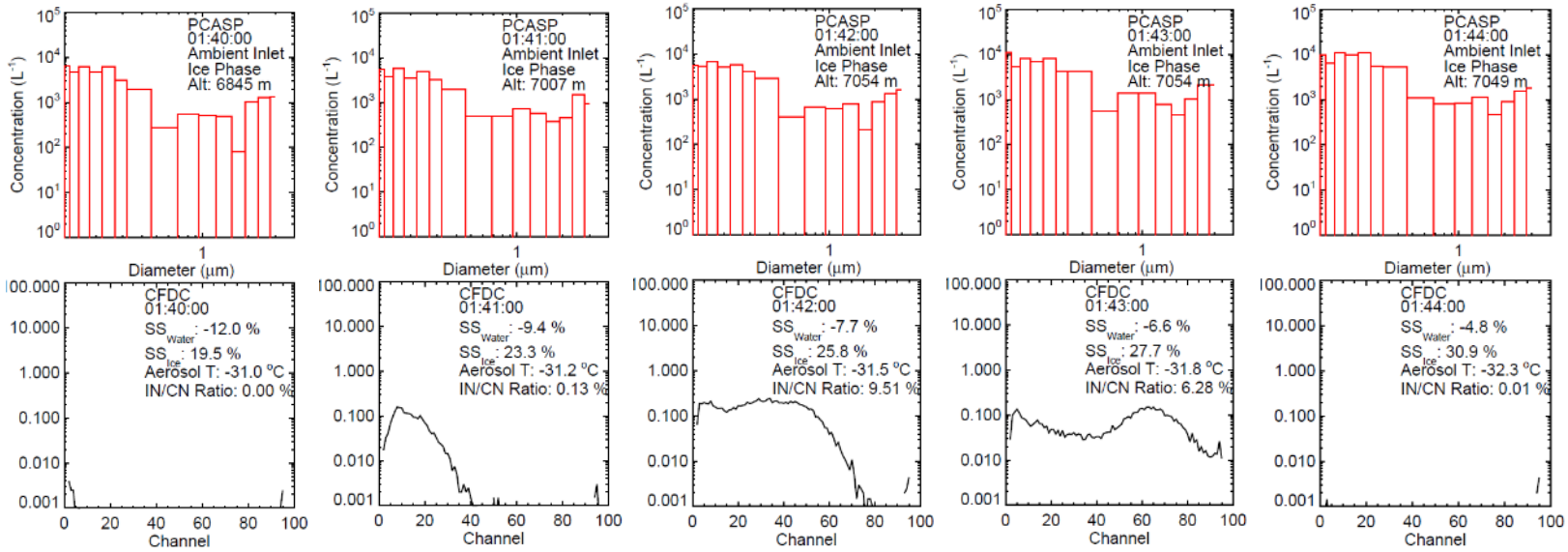


**Figure 24. Full aerosol size distributions measured by the PCASP (top panels) and the CFDC Climet (bottom panels) for a fully glaciated cloud during flight 24.**

The final nucleation event of interest occurred during Flight 24 between 23:17 and 23:24 UTC. This event was the longest lasting of all the nucleation events identified in Table 1. The PCASP data shows a change in the ambient size distribution during the event, specifically an increase in the concentration of particles larger than 0.939 μm. The number concentration of activated IN was as high as $1x10^3$ $L^{-1}$ during the nucleation event, which had CFDC operational conditions of approximately $SS_{water}$ = -15 %, $SS_{ice}$ = 14 % and aerosol nucleation temperature of -28.5 °C. This nucleation event was driven by the change in IN diameter which can be seen in the PCASP and CFDC OPC 1 minute average size distributions in Figure 26. The PCASP size distribution for the first interval (23:17 UTC) exhibits a distinct decrease in the number concentration per bin for particle diameters larger than 0.459 um, often referred to as the tail of the distribution. The next interval (23:18 UTC) does not exhibit this decreasing tail but instead shows a slight increase in number concentration for the larger particle sizes. This trend in the size distribution continues until 23:23 UTC at which point the PCASP size distribution reverts back to having a decreasing tail similar to that of the 23:17 UTC. The CFDC OPC distribution shows a direct correlation in the increase of activated IN as the PCASP distribution increases at larger sizes. The distribution of activated IN has completely dissipated by 23:24 UTC indicating that the aircraft had moved out of the region of efficient IN.

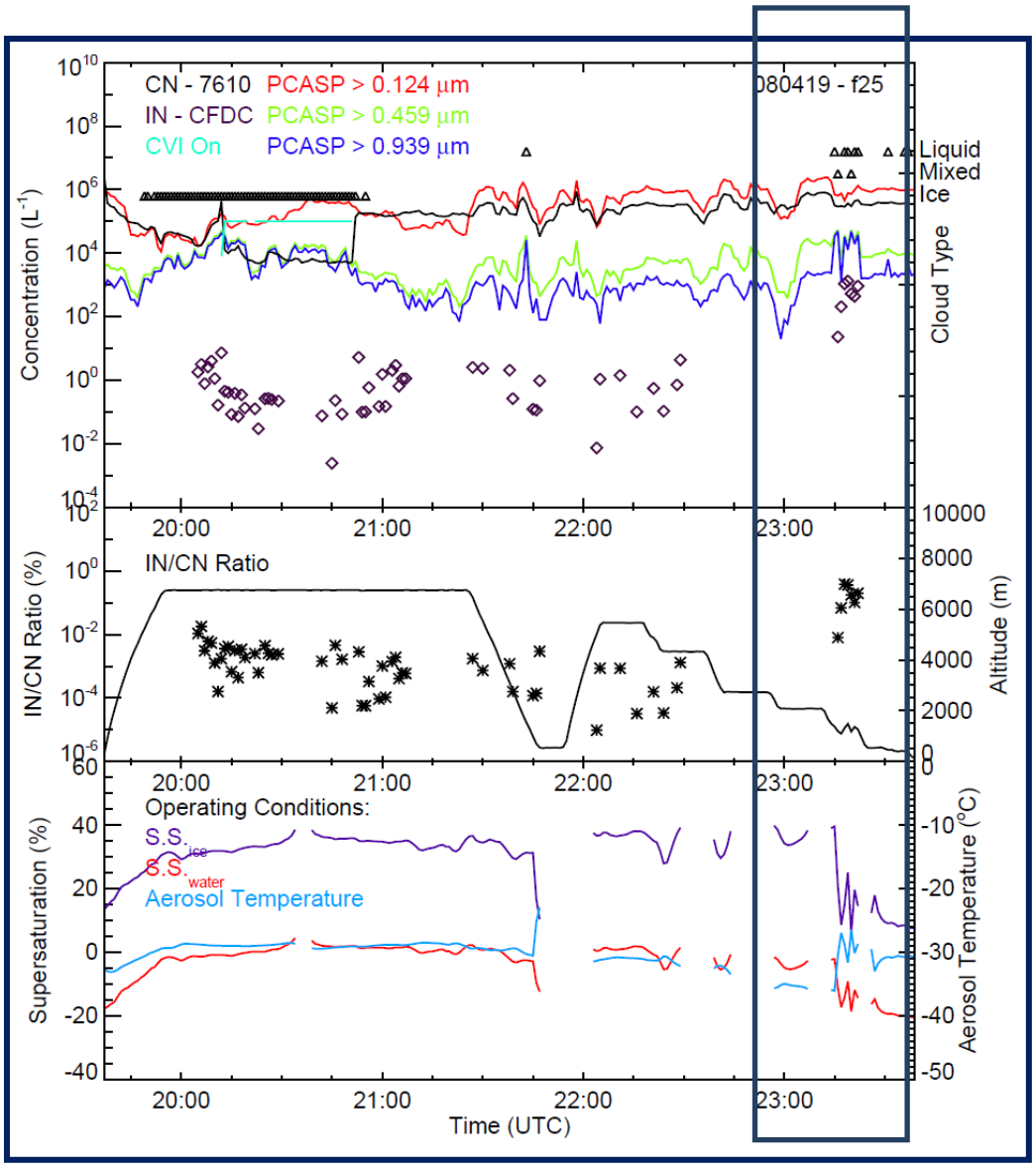


**Figure 25. Time series of IN concentration, PCASP size distribution, cloud phase, altitude, and CFDC operating conditions for flight 25.**

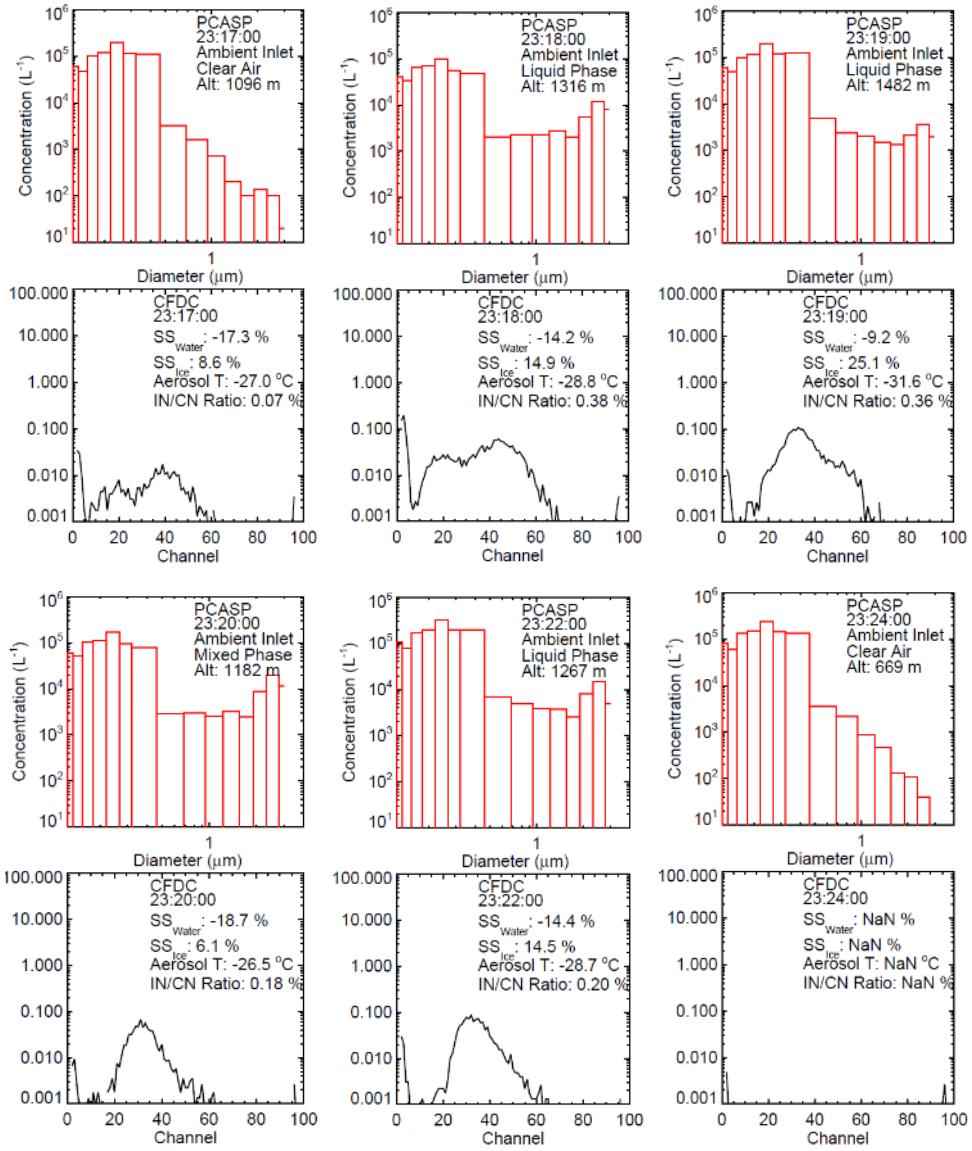


**Figure 26. Full aerosol size distributions measured by the PCASP (top panels) and the CFDC Climet (bottom panels) for a fully glaciated cloud during flight 25.**

# 4. CLOUD AND AEROSOL SPECTROMETER WITH POLARIZATION - MK I*

A new optical particle counter (OPC) was acquired by Texas A&M University. This instrument was a prototype constructed by Droplet Measurement Technologies, with beta testing provided by Texas A&M University. This OPC is based on the forward and backward scattering capability of the Cloud and Aerosol Spectrometer (CAS) sensor of the Cloud Aerosol and Precipitation Spectrometer (CAPS) (Baumgardner et al., 2011; 2001). However, this new instrument has two key features which set it apart from the CAS. First, in addition to forward and backward scattering intensity, the polarized backscattering intensity is also measured. Second, data is collected on a single particle basis which provides a measure of particle-by-particle variability and single particle optical properties.

The following section discusses this instrument, experimental data and the development of a new analysis technique. This work was the basis for the following published journal article: "Glen, A., Brooks, S. D., 2013. A new method for measuring optical scattering properties of atmospherically relevant dusts using the Cloud and Aerosol Spectrometer with Polarization (CASPOL). Atmospheric Chemistry and Physics, 13, 1345-1356, doi:10.5194/acp-13-1345-2013".

---

* Reprinted with permission from "A new method for measuring optical scattering properties of atmospherically relevant dusts using the Cloud and Aerosol Spectrometer with Polarization (CASPOL)" by Glen, A. and Brooks, S. D., Atmospheric Chemistry and Physics, 13, 1345-1356, 2013, Copyright 2013 by Author(s), CC Attribution 3.0 License.

As atmospheric aerosols have major impacts on regional and global climate through scattering and absorption of solar radiation. A new instrument, the CASPOL measures light scattered by aerosols in the forward (4° to 12°) and backward (168° to 176°) directions, with an additional polarized detector in the backward direction. Scattering by a single particle can be measured by all three detectors for aerosols in a broad range of sizes, 0.6 μm < diameter < 50 μm. The CASPOL is a unique measurement tool, since unlike most in-situ probes, it can measure optical properties on a particle-by-particle basis. In this study, single particle CASPOL measurements for thirteen atmospherically relevant dusts were obtained and their optical scattering signatures were evaluated. In addition, Scanning Electron Microscopy (SEM) was used to characterize the shape and morphology of each type of dust. The total and polarized backscatter intensities varied with particle size for all dust types. Using a new optical signature technique all but one dust type could be categorized into one of three optical scattering groups. Additionally, a composite method was used to derive the optical signature of Arizona Test Dust (ATD) by combining the signatures of its major components. The derived signature was consistent with the measured signature of ATD. Finally, calculated backscattering cross sections for representative dust from each of the three main groups were found to vary by as much as a factor of 7, the difference between the backscattering cross sections of white quartz ($5.3 \times 10^{-10}$ $cm^{-2}$) and hematite ($4.1 \times 10^{-9}$ $cm^{-2}$).

## 4.1 Cloud and Aerosol Spectrometer with Polarization (CASPOL)

The first objective of this study was to test the ability of the newly designed CASPOL instrument to detect forward, total and polarized backscattered light from spherical particles, and various types of non-spherical dusts generated in the laboratory. The second objective was to determine the feasibility of using the CASPOL to differentiate between the optical properties of various types of non-spherical dusts. Single particle CASPOL measurements for a collection of atmospherically relevant dusts were obtained. The optical signatures of the dusts were evaluated to test whether dusts from certain source locations had unique signatures which could be used to determine dust type sampled during in-situ measurements. In addition, differences in optical scattering provide insight into potential differences in aerosol direct effects on climate.

The CASPOL employs a linearly polarized laser to provide a collimated incident beam of light at a wavelength of 680 nm (Figure 27). There are four detectors in the instrument, with collection angles of 4° to 12° for the forward detectors and 168° to 176° for the backward detectors, as seen in Figure 27.

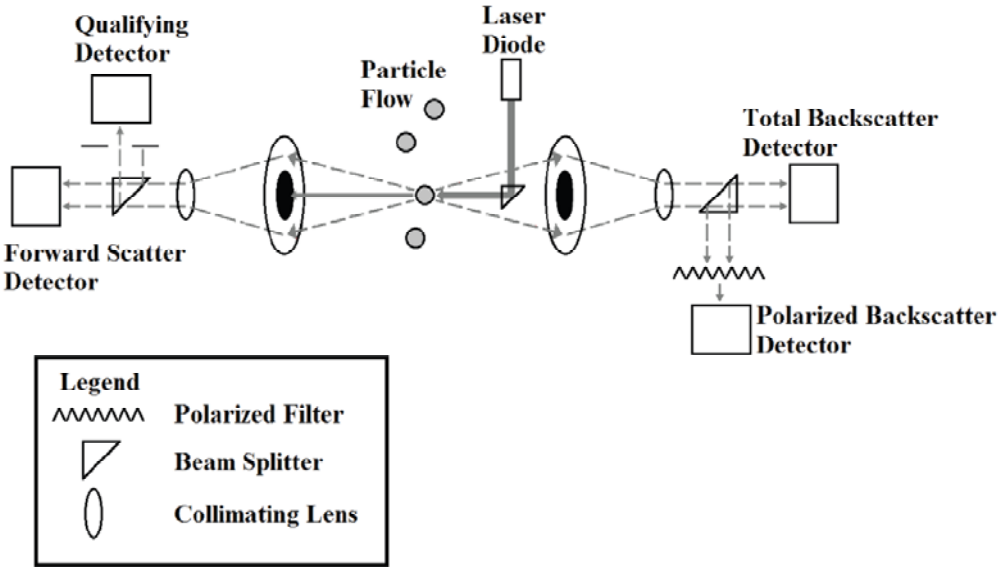


**Figure 27**. **Schematic of the CASPOL instrument (DMT, 2011).**

The particle's water equivalent optical diameter is determined from the primary forward scattering signal. Note that in this manuscript, diameter refers to the water equivalent optical diameter, not the geometric diameter. The CASPOL can measure light scattering from particles over a size range of 0.6 µm to 50.0 µm in diameter. Light scattered in the backward direction passes through a beam splitter which directs light to two independent detectors. One of the backward detectors measures the total backscatter intensity. The intensity of scattered light in the backward direction gives insight into particle shape, as it is more dependent on shape than scattering in the forward direction is. The second backward detector measures perpendicularly polarized backscatter intensity over the same angles as the total backward detector. The polarized backscatter detector is used in conjunction with the total backscatter detector to calculate the

polarization ratio. The polarization ratio, δ, used in this paper is defined in Equation 1 below.

$$\delta_{168^\circ}^{176^\circ} = \frac{Polarized \quad Backscatter \quad Intensity}{Total \quad Backscatter \quad Intensity} \qquad \text{Equation 1}$$

Since the collection angles of light in the backward direction are not quite at 180° and the prototype CASPOL instrument used here employs a total backscattering detector rather than a parallel polarized light detector, the resulting polarization ratio differs from the depolarization ratio used by the lidar community. Similar to the lidar depolarization ratio, the theoretical polarization ratio for a spherical liquid droplet is approximately zero. Finally, there is an additional detector in the forward direction which is used as a qualifier. The qualifier detector has an optical mask which restricts scattered light from particles that are further than 0.75 mm from the center of focus of the laser beam (DMT, 2011). Particles which are within the depth of field (± 0.55 mm either side of the center of focus) are measured using the qualifier detector. The beam splitter which separates the two detectors is split with 70% of the light delivered to the qualifier and 30% delivered to the forward scattering detector. Each time the qualifier detector signal exceeds the forward scattering detector signal, the peak amplitude of the scattered light signal is recorded and counted as a particle.

## 4.2 CASPOL Size Calibration

To calibrate the CASPOL particle sizing, a TSI 3450 Vibrating Orifice Aerosol Generator (VOAG) with a 20 μm diameter orifice was used (Figure 28). A series of calibration experiments were performed on particles ranging from 2 μm to 19 μm diameter. The VOAG generates a monodisperse distribution of spherical particles by forcing a suspension of olive oil and isopropyl alcohol through a small orifice powered by a motorized syringe. During operation, an AC signal generator is used to induce oscillation in a piezoelectric ceramic disk. The oscillation is transmitted directly to the orifice causing breakup of the otherwise cylindrical jet of solution. The mean particle diameter generated by the VOAG depends on the initial concentration of the solution, the frequency of oscillation, the syringe feed rate, and the orifice diameter (Liu et al., 1974). The theoretical VOAG diameter, $D_p$ is calculated by Equation 2 (TSI, 2002):

$$D_P = C^{\frac{1}{2}}\left(\frac{6Q}{\pi f}\right)^{\frac{1}{3}} \qquad \text{Equation 2}$$

where C is the volumetric concentration of solute in the solution, Q is the syringe flow rate of the solution and f is the frequency of oscillation.

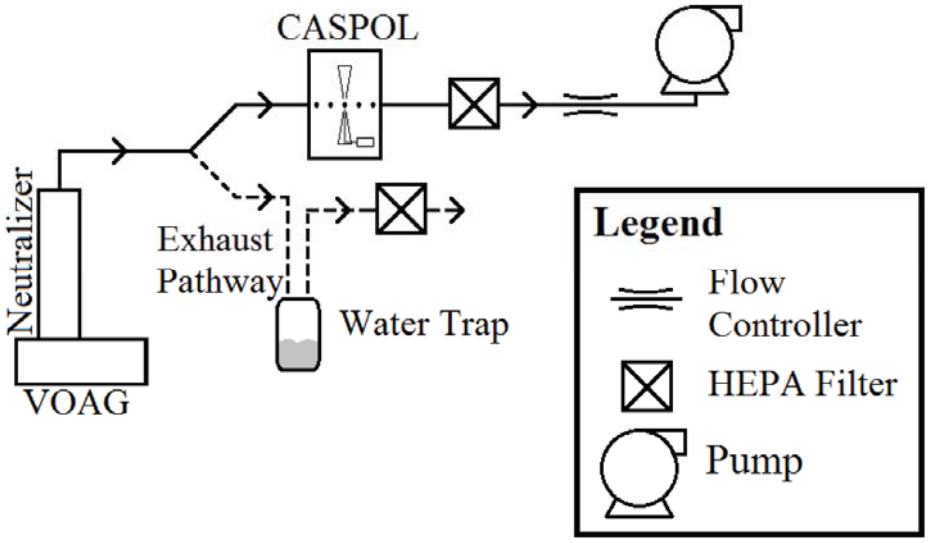


**Figure 28. Experimental setup used to calibrate the CASPOL using a TSI Vibrating Orifice Aerosol Generator (VOAG).**

Individual droplets escaping the orifice are transported through the VOAG neutralizer and chamber by a dispersion flow of filtered air which also acts to evaporate the isopropanol, leaving pure olive oil droplets, with a refractive index of 1.46 (Yunus et al., 2009). Next the flow of particle-laden air is distributed between two pathways. The first pathway leads to the CASPOL at a flow rate of 1.2 L $min^{-1}$ controlled by a mass flow controller (Alicat Scientific Inc, MCP-20SLPM) and pump. The second pathway is an exhaust to reduce the air flow rate and pressure of the system. Near-monodisperse distributions of particles were generated by the VOAG and sampled by the CASPOL over the broad size range, 0.6 μm to 50 μm.

## 4.3 Measurements of the Optical Scattering Signatures of Atmospheric Dust Particles

To measure the scattering properties of the dust samples, experiments were conducted using the setup shown in Figure 29. These experiments used a Topas Solid Aerosol Generator 410 (SAG) to generate a polydisperse distribution of dust. The SAG allows the dust to be aerosolized without the need of a suspension liquid such as water, ensuring the aerosol particles are completely dry. Within the SAG, a rotating scraper evenly fills sample spaces in a toothed conveyor belt. The belt then transports the individual amounts of sample to an ejector nozzle which aerosolizes the sample by means of a high pressure dry nitrogen inlet.

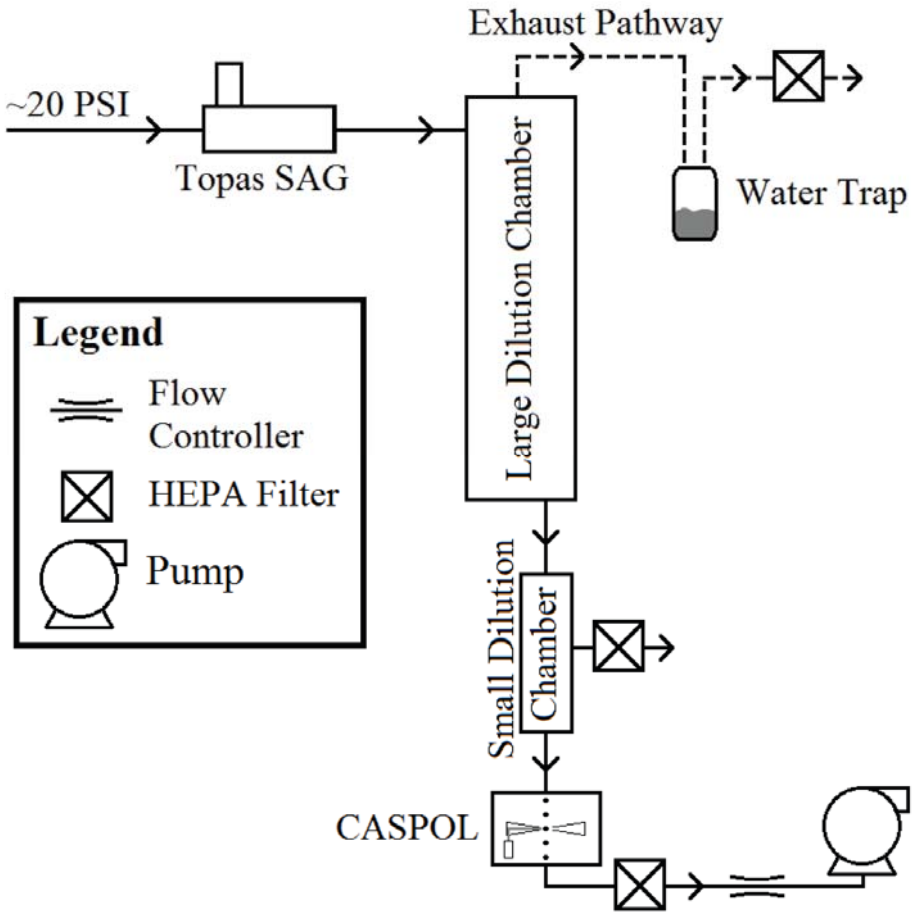


**Figure 29. Experimental setup for CASPOL dust measurements.**

All of the dusts were generated using the same control settings for the input pressure of 20 psi, a preparation rate set at 3 (dictating how fast the dust scraper rotates and deposits dust on the belt) and a belt speed set at 0.3% of maximum speed. Thus, any observed differences in aerosol size distributions reflect the intrinsic differences in dust samples rather than operating conditions. The aerosolized dusts were directed to a large dilution chamber, which allowed for a reduction in particle concentration and total flow of the aerosol stream by removing air via the exhaust pathway. At the output of the large

dilution chamber is a smaller dilution chamber with two outlets, one for sampling and one for a filtered exhaust outlet allowing the system to be kept at near ambient atmospheric pressure (Figure 29). Next, the CASPOL drew aerosol-laden air from the sample line at a flow rate of 1.2 L $min^{-1}$, identical to the calibration flow rate. CASPOL data was recorded for each single particle. The CASPOL's single particle temporal resolution is 5 ms. The sampling time varied from ~30 minutes to 100 minutes, to ensure that at least ~$10^5$ particles were sampled per experiment. Additionally, during the experiments, samples of each dust were diverted from the CASPOL aerosol stream and directed to a single stage PIXE impactor for subsequent imaging using Scanning Electron Microscopy (SEM), as discussed further in Section 4.4.

The thirteen dust types included in these experiments and their sources are listed in Table 2. Eight of these were commercially available single component samples. The last commercially available sample, Arizona test dust, is a well characterized multi-component specimen primarily composed of three components, montmorillonite, kaolinite and hematite in weight percentages of ~45, 45, and 10% respectively, as described by the manufacturer (Powder Technology Inc.). In addition, four dust field samples collected from ground sites around the world, including two from different locations in Saudi Arabia and two from different locations in New Mexico, USA were used. The latitude and longitude of each field sampling location is included in Table 2. Values of the refractive indices of the commercial dusts reported in the literature are also listed in the table. Reported values for the real component of refractive index range from 1.49 for zeolite to 2.31 for hematite (Kerker et al., 1979; Li et al., 2010). The imaginary

part of the refractive index is small for most of these dusts (Curtis et al., 2008), with the exception of hematite and magnetite which are strong absorbers of visible light.

## 4.4 Scanning Electron Microscopy (SEM)

Scanning Electron Microscopy (SEM) was used to observe particle morphology using a JEOL 6400 microscope. During approximately 30 minutes of each CASPOL experiment, a sample was collected on an aluminum foil disk mounted on a PIXE 0.5 μm impactor stage. Particles were subsequently taken to the Microscopy and Imaging Center on the Texas A&M University Campus for SEM analysis. In preparation for SEM analysis which requires electrical conductivity, samples were vapor stabilized using osmium tetroxide and then sputter coated with gold and platinum (Ellis and Pendleton, 2007). SEM images were taken at a resolution of 3.5 nm for all dust types and these images were used to identify differences and similarities in particle shape.

**Table 2. Properties of the dust type included in this study.**

| | Refractive Index | | | Primary Mode | Secondary Mode | Aspect Ratio | | | |
|---|---|---|---|---|---|---|---|---|---|
| | Real | Complex | Source** | Diameter (μm) | Diameter (μm) | Mean | St.Dev | Group | Reference |
| Arizona Test Dust | 1.51 | $1.02x10^{-3}$ | 33.38 N, -112.31 E | 2.0 | 0.61 | 1.5 | 0.3 | - | Powder Technology Inc |
| Hematite | 2.31 | | Sigma Aldrich | 2.0 | 0.61 | 2.4 | 1.4 | A | Kerker et al., 1979 |
| Kaolinite | 1.57 | $6.60x10^{-3}$ | Sigma Aldrich | 2.0 | 5.0 | 1.5 | 0.4 | A | Arakawa et al., 1997 |
| Gypsum | 1.61 | $0.01x10^{-3}$ | Sigma Aldrich | 0.61 | 1.5 | 2.3 | 0.4 | B | Ivlev and Popova.,1973 |
| Quartz | 1.54 | $0.01x10^{-3}$ | Fluka | 0.61 | 1.5 | 1.9 | 0.7 | B | Filmetrics Database |
| Red New Mexico | * | | 35.82 N, -106.62 E | 0.61 | 1.5 | 1.5 | 0.5 | B | |
| Red Saudi Arabia | * | | 24.37 N, 46.25 E | 0.61 | 1.5 | 2.0 | 0.5 | B | |
| White Quartz | 1.54 | $0.01x10^{-3}$ | Sigma Aldrich | 0.61 | 1.5 | 1.7 | 0.2 | B | refractiveindex.info Database |
| White Sands | * | | 32.88 N, -106.35 E | 0.61 | 1.5 | 1.9 | 0.7 | B | |
| Magnetite | 2.15 | | Aldrich Chemicals | 1.5 | 0.61 | 1.8 | 0.7 | C | Schlegel et al, 1979 |
| Montmorillonite | 1.53 | $1.47x10^{-3}$ | Sigma Aldrich | 0.61 | 1.5 | 1.6 | 0.3 | C | Arakawa et al., 1997 |
| Yellow Saudi Arabia | * | | 25.27 N, 46.67 E | 1.5 | 0.61 | 1.5 | 0.2 | C | |
| Zeolite | 1.49 | | Sigma Aldrich | 0.61 | 1.5 | 1.2 | 0.1 | C | Li et al., 2010 |

*** Indicates field collected sample with no measurement of refractive index.**

**** The source of the sample is included for commercially available dusts, for field samples the source is listed as the location of collection.**

## 4.5 CASPOL Size Calibration Results

Results of the CASPOL size calibration are shown in Figure 30. In general, diameters measured by the CASPOL for olive oil particles are in good agreement with those chosen by the VOAG operating conditions. The uncertainties shown in Figure 30 for the VOAG diameters are based on the uncertainty in the theoretical calculation of the VOAG generated particle diameters, as described in the instrument manual (TSI, 2002). The uncertainties in the CASPOL diameters are the standard deviations from the mean diameter of the log normal size distributions fitted to the CASPOL measured calibration particle size generated by the VOAG. At diameters less than 10 μm, the agreement between the VOAG and CASPOL is within 25%. At particle diameters larger than 13 μm there is some deviation between the CASPOL and the VOAG. This may be due to a combination of factors. At relatively large particle sizes, the VOAG has been known to miss-size particles, with actual particle size not being accurately predicted by theory (Peters et al., 2008). This may be due to the increase in the surface stress of the droplet at larger volumes which causes a deformation of a particle from spherical to non-spherical and subsequently induces breakup. Also, the manufacturer's size calibration of the CASPOL is based on water equivalent particles. Due to the differences in refractive indices between water and olive oil, diameters of oil droplets determined in our calibration will be overestimated by as much as ~30%. For example a 1.9 μm oil particle has a water equivalent diameter of 2.5 μm.

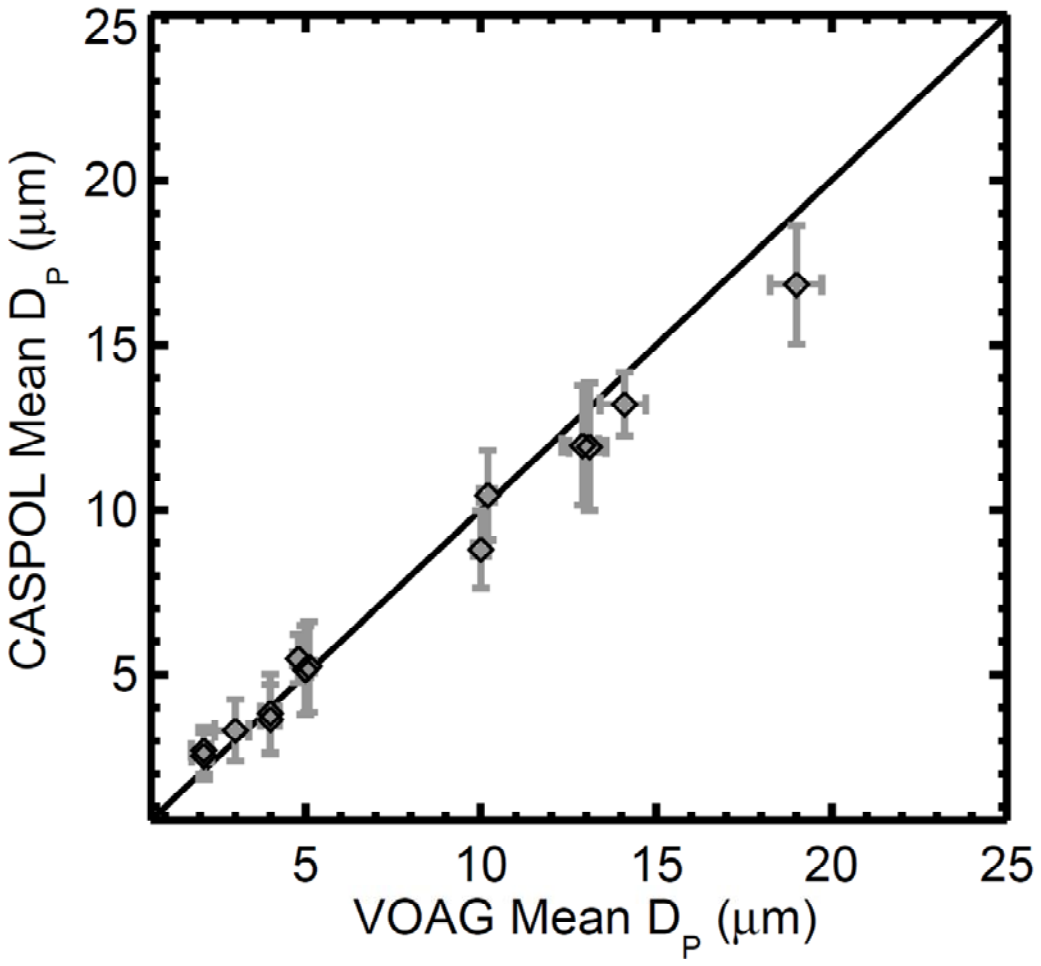


**Figure 30. Size calibration of the CASPOL. The theoretical VOAG mean particle diameter is on the abscissa and the measured CASPOL mean diameter is on the ordinate. The error bars represent measurement uncertainties in both determinations of diameters.**

4.6 Optical Scattering of Atmospheric Dust Particles

The average total backscatter intensity and polarization ratio of all the particles per size channel, are shown in Figure 31, Panels A and B respectively. In general, the total backscattering intensity increased with size for all of the dust types. However,

variations in total backscatter intensity of up to a factor 3 were observed depending on particle composition. At most diameters, red Saudi Arabian dust had the lowest total backscatter intensity and the hematite had the highest. The observed variation in total backscatter intensity proved to be helpful in categorizing aerosol types as discussed further below.

Figure 31, Panel B shows that particles in the submicron sizes have the largest values of polarization ratio. For submicron particles, the polarization ratio ranged from ~1.0 for kaolinite to ~2.0 for montmorillonite. The polarization ratio in the figure shows a reduction with increasing particle diameter, suggesting that larger particles may be more spherical. Also, as the particle diameters increase, the variation between the polarization ratios of various dusts is reduced. It should be noted that polarization ratio values greater than unity were observed; this is a result of an instrumental artifact in this prototype unit and will be addressed in revised versions of the instrument by DMT.

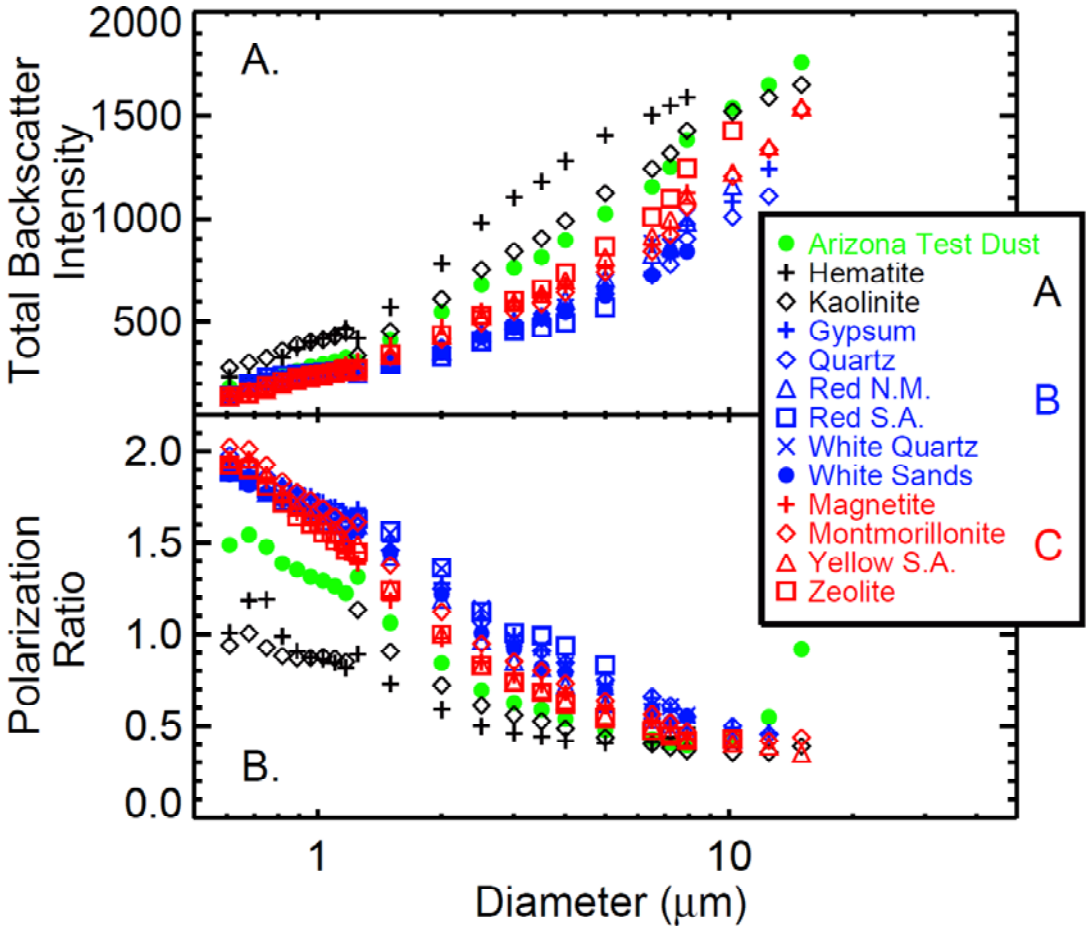


**Figure 31. Total backscatter intensity and polarization ratio as a function of particle diameter for all dust types. Individual dust types identified as members of optical scattering groups A, B, and C are represented by black, blue, and red symbols, respectively. Data for Arizona test dust, the one outlier in the study, is represented by green circles.**

Based on these raw data, the thirteen dust samples were sorted into three groups, with only one outlier. Groups A through C aptly describe the characteristics of all dust types except Arizona test dust, which is further discussed below. In Figure 31 the group identifications for each individual dust type are denoted by the color of the symbols in the legend. We note that the standard deviation in measurements of both the total

backscatter intensity and polarization ratio show significant overlap between dust types (not shown). To illustrate the range of total backscatter intensity values obtained for a single particle size, the distribution of total backscatter intensity as a function of dust type for one size channel of the CASPOL (2.5 μm to 3.0 μm) is shown in Figure 32. The 2.5 to 3.0 μm size channel was chosen as a good representative diameter since dust in this size range is transported globally (Prospero et al., 1970). In Figure 32, the abscissa denotes the type of dust and the ordinate shows the relative total backscatter intensity, displayed in arbitrary units (a.u.). The legend indicates the percentage of the total number of particles in the 2.5 to 3.0 μm size channel for that particular dust type which have the given total backscatter intensity.

The deviation in total backscatter intensity amongst particles within a single diameter bin is an indication of the degree of variation in the characteristics, specifically shape and surface roughness, of the individual particles within a single composition and size. Variation in the total backscatter intensity may also arise from differences in the particle orientation when passing through the CASPOL sampling region. As Figure 32 shows, differences were observed in both the mean total backscatter intensity and the spread in intensity for various dust types. For particles in the 2.5 to 3.0 μm size channel, the mean total backscattering intensity varied by more than a factor of 3 from a low of 280 a.u. for white sands to a high of 900 a.u. for hematite. The plots in Figure 32 provide a more robust differentiation between groups A, B, and C. Members of Group A, hematite and kaolinite have the majority of particles at total backscatter intensities above 500 a.u., with very large variability in total backscatter intensity, and no discernible peak

intensity. Based only on these backscatter plots, Arizona test dust data was not discernible from members of Group A. Group B data is characterized by high peak frequencies (above 7% of the total), and peak total backscatter intensities less than 400 a.u.. This group also has the lowest standard deviation in total backscatter intensity for a single size. Data from members of Group C features peak total backscatter intensities of less than 500 a.u., with peak frequencies less than 5% of the total particles in the 2.5 to 3.0 μm channel.

Overall, these results indicate that particle size is influential but not the dominant factor in the total backscattering intensity. Other particle properties such as composition, refractive index, morphology, and orientation may also play a significant role in determining the intensity of backscattered light from a particle of given size. To further develop a systematic characterization of the dust samples into the listed groups, a new analysis was developed and is discussed in Section 4.9.

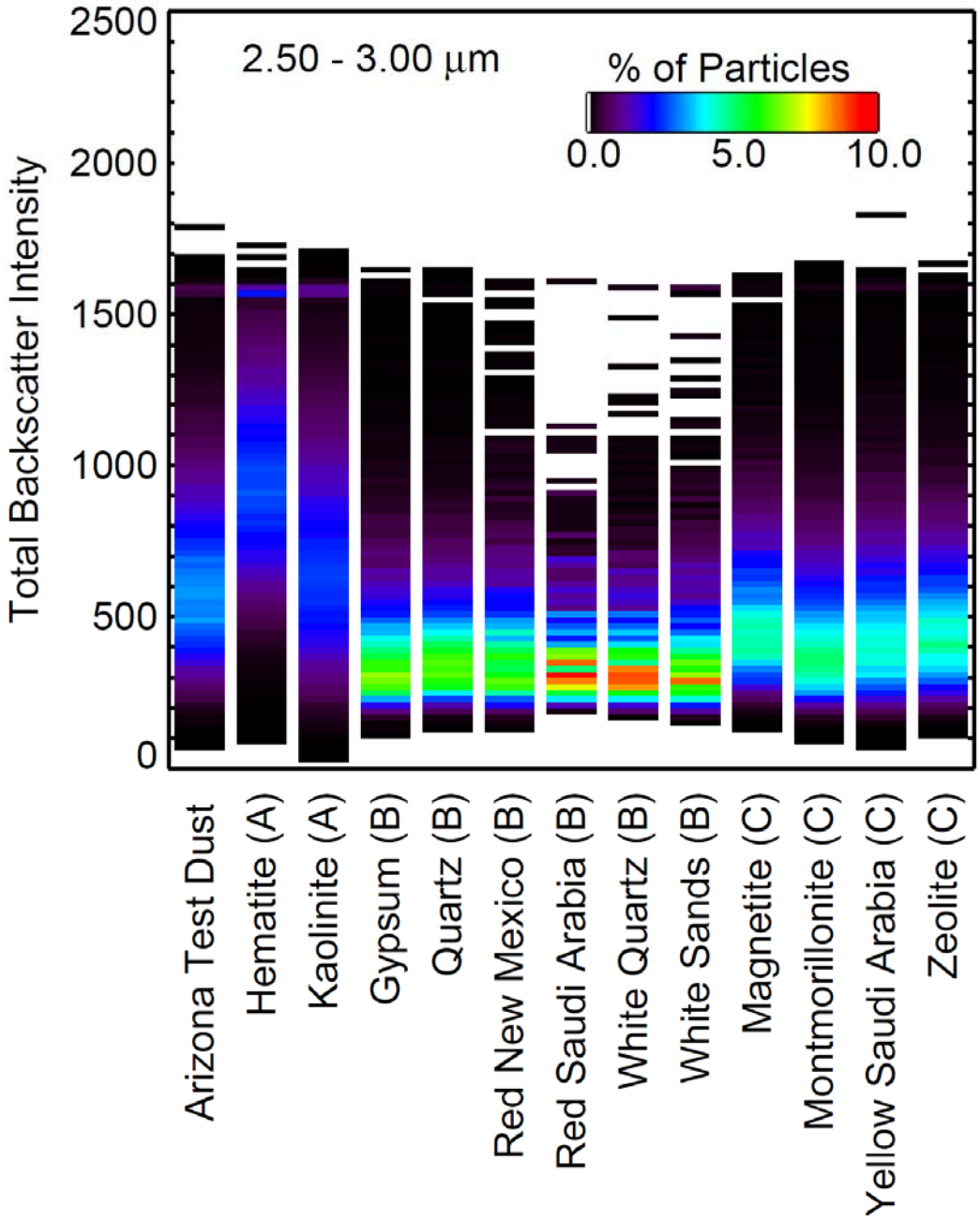


**Figure 32. For the 2.5 µm to 3.0 µm CASPOL channel, the percentages of particles which have a given total backscatter intensity are shown for each dust type.**

## 4.7 Size Distributions of Characteristic Dusts

Size distributions based on CASPOL forward scattering measurements of at least $10^5$ particles were obtained for each dust type. The average size distributions measured by the CASPOL are shown in Figure 33 for hematite (Panel A), white quartz (Panel B) and zeolite (Panel C). As seen in Figure 33, the shape of the size distributions varied depending on the composition of the sample. All of the thirteen dust types produced size distributions with multiple modes. The primary and secondary mode diameter for all of the dust distributions are shown in Table 2. Eight of the thirteen samples generated by the SAG produced size distributions with a primary mode in the 0.6 μm channel and a strong secondary mode at 1.5 μm. The remaining five dust types have a dominant mode at either 1.5 μm or 2.0 μm, with a smaller mode at 0.6 μm. Four of the dusts, Arizona test dust, montmorillonite, yellow Saudi Arabia and zeolite display a third mode in the CASPOL measured size distributions between 4.5 and 5.0 μm. The two dusts in Group A, hematite and kaolinite have different size distributions, as hematite has a primary mode at 2.0 μm and a secondary much lower concentration mode at submicron sizes. Kaolinite has a primary mode at 2.0 μm and a secondary mode with a similar concentration to the primary at 5.0 μm. Group B were more consistent with the same mode diameters of the bimodal distribution for all dusts. Gypsum, red New Mexico, red Saudi Arabia, white quartz and white sands all have lower average concentrations with most size bins having concentrations below 300 $L^{-1}$. However, the standard quartz sample has concentrations of nearly double those measured for the other five dusts in

this group. Dusts in Group C all had very similar size distributions which have mode diameters at 0.6 μm and 1.5 μm. In summary, Groups B and C have defining size distribution characteristics but Group A does not.

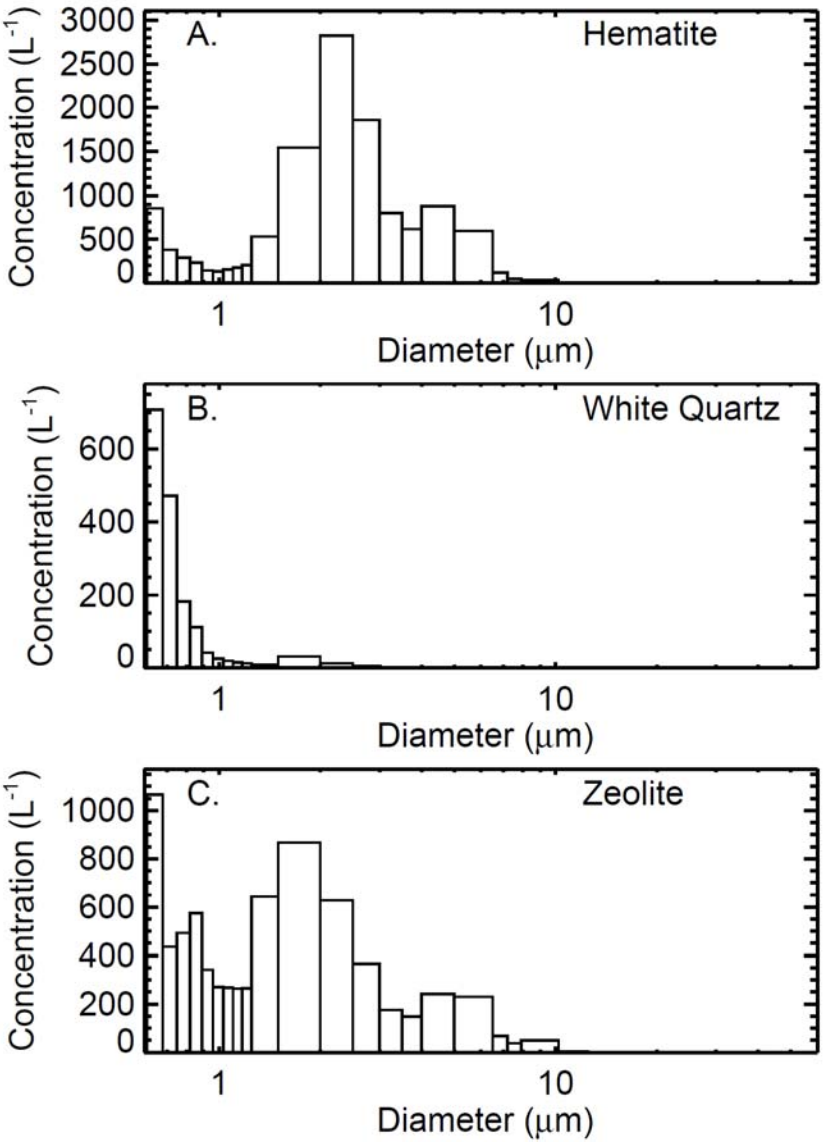


**Figure 33. Average particle size distributions as measured by the CASPOL for three dust types: hematite, white quartz and zeolite.**

## 4.8 Particle Shape Using Scanning Electron Microscopy

High resolution SEM images for the three representative aerosols are shown in Figure 34. In each case, particle size ranges from submicron to supermicron in diameter. Hematite samples have long aggregates of supermicron size particles comprised of smaller more spherical submicron particles. Similarly, kaolinite is composed of smaller elongated spheroids clumped together to form larger supermicron particles. Gypsum particles are present as supermicron particles consisting of submicron blocks with round edges. The zeolite particles are very cubic and have individual particles clumped together to form agglomerates. Both quartz and white quartz samples are more irregularly shaped. Magnetite shows long chain aggregates and clumps of elongated spheroids. The montmorillonite sample has irregularly shaped spheroids. The average and standard deviation in aspect ratios for each dust were estimated using ImageJ software to analyze the SEM images (Table 2). The images do not yield any distinctive similarities for dust types allocated to the same groupings, indicating that shape and size are not the only determining factors in the optical scattering properties.

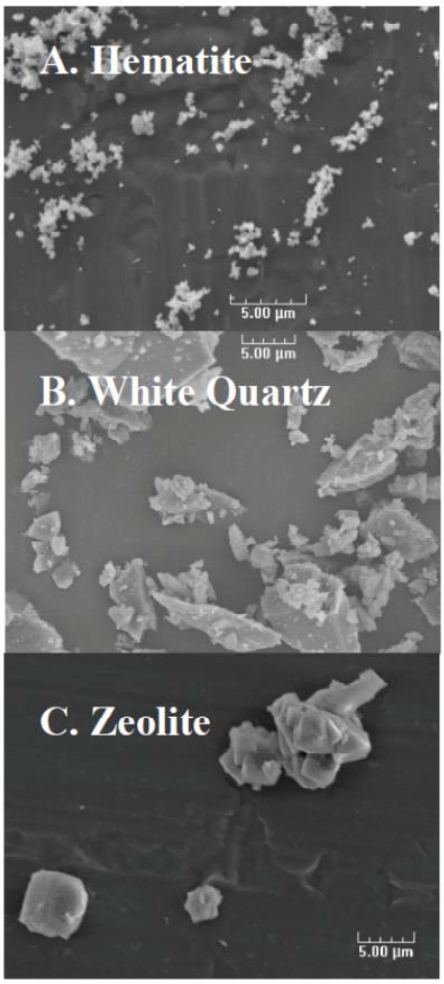


**Figure 34. SEM images of hematite, quartz, and zeolite particles are shown in panels A, B, and C respectively.**

4.9 Categorization of Dust Types from Optical Signatures

A new strategy using the optical properties of each dust type to categorize the dust groupings was developed. The range of each variable, forward scattering, total backscatter and polarization ratio, was discretized and the frequency of particles which had intersecting values was placed in each discretized bin. This analysis was completed

for all the dust samples. For example, Figure 35 shows the signature of total backscatter intensity vs. polarization ratio for the representative dusts. Similarly, the total backscatter to forward scatter ratio vs. the polarized backscatter to forward scatter ratio is shown in Figure 36. Both sets of optical signature figures are for the same three dusts (hematite, white quartz and zeolite), chosen to be representative of Groups A, B and C and shown in the figure Panels A, B and C respectively. Inspection of these signatures can provide a means to classify each sample into the optical category A, B, or C with certainty and without the aid of any auxiliary information. Signature details for each dust type are summarized in Table 3.

**Table 3. Rules for differentiating between dust groups A, B, and C.**

| Total Backscatter Intensity vs. Polarization Ratio | | | |
|---|---|---|---|
| | **Group A** | **Group B** | **Group C** |
| **Shape** | **Steep Curve** | **Linear Decrease** | **Shallow Curve** |
| **Polarization Ratio** | **< 1.0** | **> 1.0** | **0.75 < P.R. < 2.5** |
| **Total Backscatter Intensity** | **500 < B.S. < 1700** | **< 400** | **< 600** |
| **Maximum Intensity (%)** | **> 0.5** | **> 0.3** | **< 0.2** |

| Total Backscatter/Forward Ratio vs. Polarized Backscatter/Forward Ratio | | | |
|---|---|---|---|
| | **Group A** | **Group B** | **Group C** |
| **Shape** | **Cluster** | **Linear Increase** | **V shaped** |
| **Polarized Backward/Forward Ratio** | **< 0.2** | **> 0.4** | **< 0.4** |
| **Total Backscatter Intensity/Forward Ratio** | **< 0.4** | **> 0.3** | **< 0.3** |
| **Maximum Intensity (%)** | **> 0.6** | **< 1.0** | **> 1.0** |

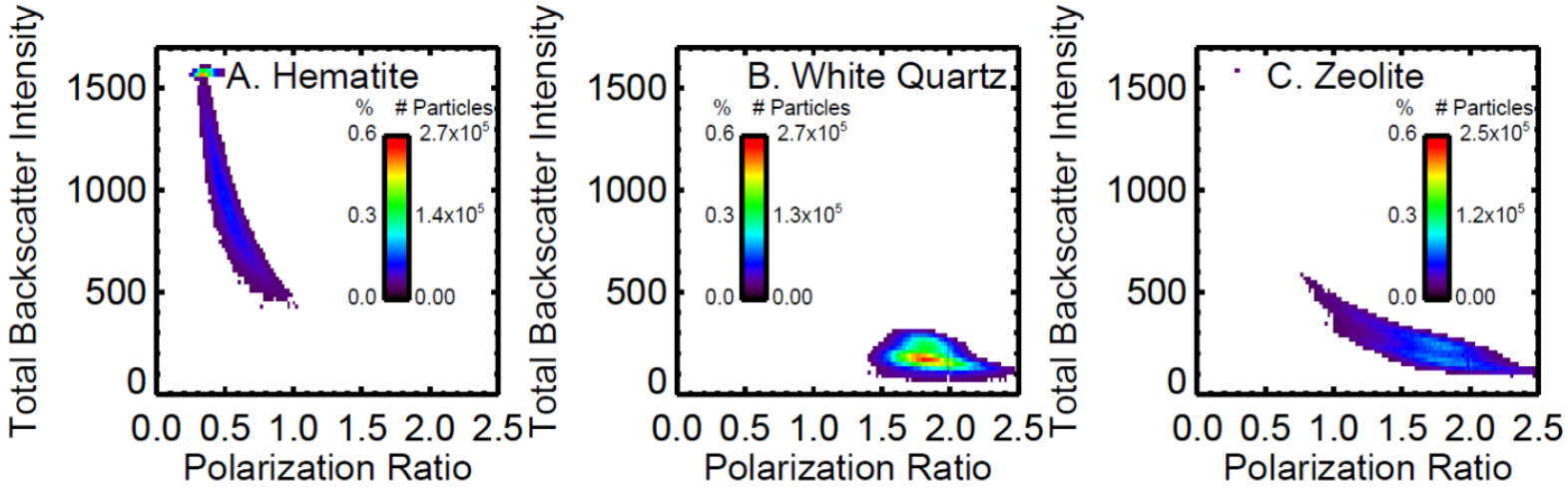


**Figure 35. Total backscatter intensity vs. polarization ratio for representative members of the optical scattering groups A (hematite), B (white quartz) and C (zeolite) are shown.**

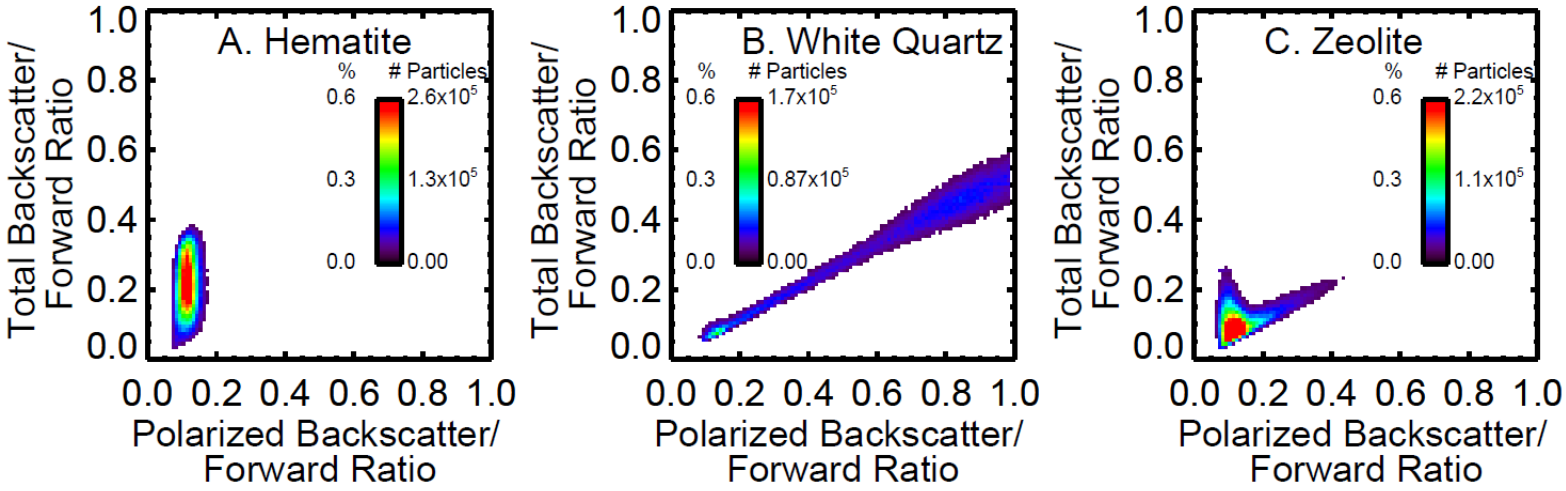


**Figure 36. Polarized backscatter to forward scatter ratio vs. total backscatter to forward scatter ratio for representative members of the optical scattering groups A (hematite), B (white quartz) and C (zeolite) are shown.**

The signature shape of data in the total backscatter intensity vs. polarization ratio plots, and the number of particles in a certain spatial region in the pixel map are very important in differentiating between the three groups. The signature curve shape for Group A is a relatively steep curve in which all members have polarization ratios < 1.0. In contrast, the Group B data can be described as a linear increase in polarization ratio with approximately constant total backscatter intensity. All particles in Group B had polarization ratios of > 1.0. Finally, Group C has a shallow curve of decreasing total backscatter intensity with increasing polarization ratio, and values of polarization ratio between 0.75 - 2.5.

For the second signature type, the total backscatter to forward scatter ratio vs. the polarized backscatter to forward scatter ratio, the overall signature shape and the values of the polarized backscatter to forward scatter ratio are the dominant factors in determining the signature (Figure 36). Members of Group A have a clustered distribution with polarized backscatter to forward ratio < 0.2. The ensemble of dust particles in Group B show a linear monotonic increase in total backscatter to forward ratio with increasing polarized backscatter to forward ratio. Members of Group C, display a 'V' shaped distribution with a maximum intensity > 1 % of the total number of particles measured and polarized backscatter to forward ratio < 0.4.

This method of identifying signatures based on the ratios of measured signals is powerful as it yields observable differences between dust types. With the exception of Arizona test dust, all of the dust samples collected in the field fit into one of the three groups using the signature method. Interestingly, dust samples from the two locations in

Saudi Arabia were allocated to different groups despite their close geographical proximity, approximately 110 km. To explore the feasibility of using the signature method in field sampling, additional signature plots were generated based on representative atmospheric loadings present during dust storms (See Supplement A). While actual field testing is required, the results indicate that this CASPOL method may potentially be used during a dust storm or other intense atmospheric dust phenomena. In addition, the constraints summarized in Table 3 could be used to develop an algorithm which classifies remote sensing observations of various types of dust.

## 4.10 Optical Signatures of Externally Mixed Ensemble Aerosol

As mentioned previously, Arizona test dust did not fit any of the signature groups. We speculate that this may be due to the fact that Arizona test dust is a multi-component dust which is highly inhomogeneous. The Arizona test dust used in this study was primarily composed of three components, montmorillonite, kaolinite and hematite in weight percentages of ~45, 45, and 10% respectively. Additional dust components appear in much smaller quantities as reported by the manufacturer (Powder Technology Inc., 2012), and are not included in this estimation. Figure 37 shows the measured signatures for Arizona test dust in Panels A (total backscatter intensity vs. polarization ratio) and C (total backscatter to forward scatter ratio vs. polarized backscatter to forward scatter ratio). A composite signature for Arizona test dust can be generated using representative concentrations of the components of which it is comprised. Taking

the additive combination of optical scattering signatures for montmorillonite, kaolinite and hematite (as discussed in Section 4.9) combined according to their known weight percentages produces the scattering signatures shown in Figure 37 panels B and D. Comparison of the measured signature (Panel A) to the composite (Panel B) for the ratio of total backscatter intensity to polarization ratio shows good agreement for the shape and intensity of the signature. However, there is some difference in shape, in that the composite signature has a narrower distribution in total backscatter intensity at a polarization ratio of ~ 1.0.

The composite total backscatter to forward scatter ratio vs. the polarized backscatter to forward scatter ratio signatures (Figure 37 Panel D) is also very similar to the measured signature (Figure 37 Panel C). The minor differences between the two panels are that the composite signature has a reduced intensity at a polarized backscatter to forward scatter ratios of ~0.1 and a slight protrusion of polarized backscatter to forward scatter ratios to values as high as ~0.3. While we have only generated composite vs. measured signatures for Arizona test dust thus far, this result for a single multi-component dust is very encouraging for the CASPOL instrument. This example suggests that it may be possible to predict the optical properties of real world dusts if only the major components of the dust are known. Future work will include CASPOL measurements and evaluation of additional external mixtures and their components.

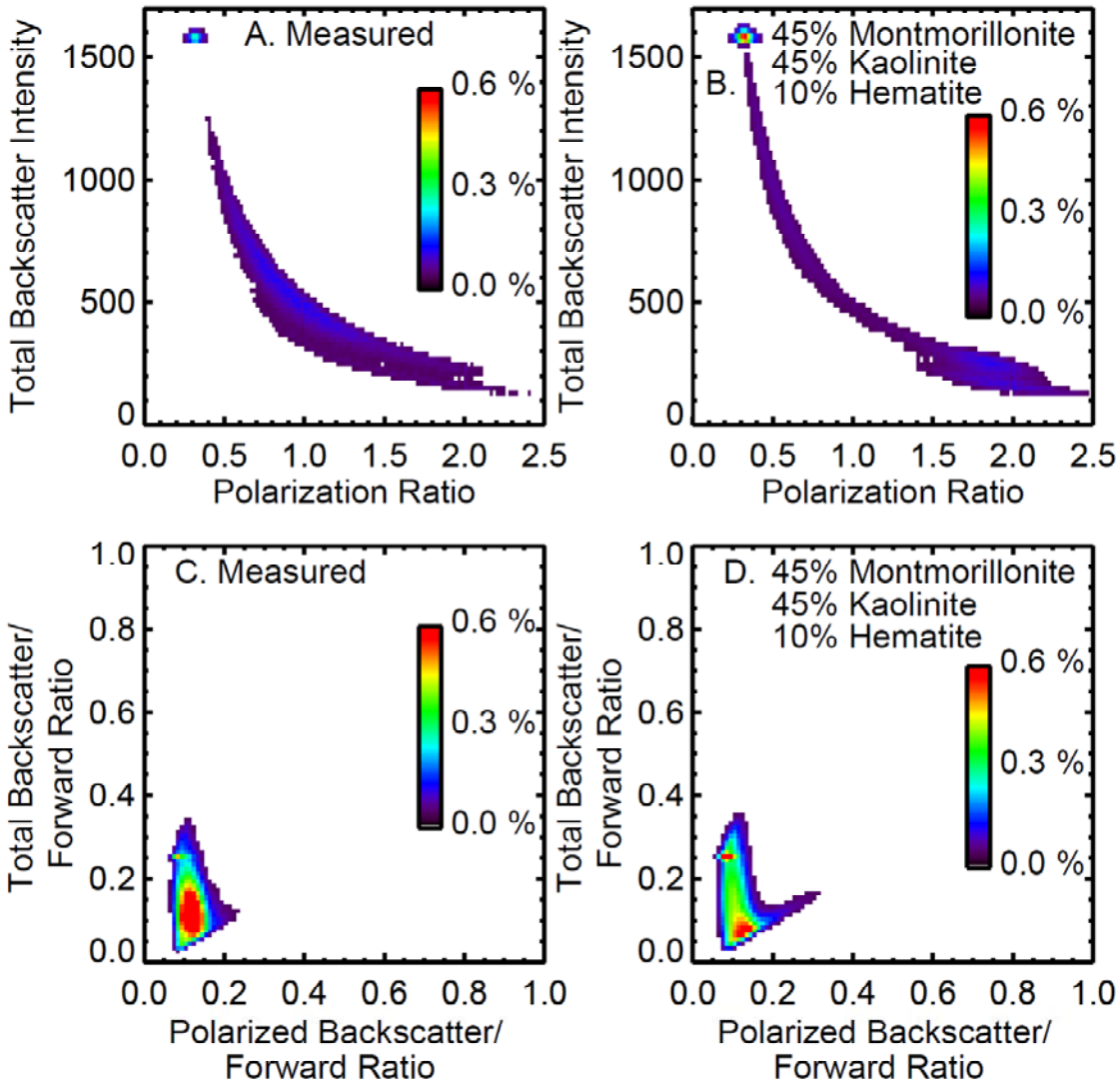


**Figure 37. The optical signature of measured Arizona test dust sample and the composite signature generated using montmorillonite, kaolinite and hematite data are shown in Figure 37A and Figure 37B, respectively.**

4.11 Estimated Backward Scattering Cross-sections

The ability of the CASPOL to simultaneously measure the forward and backward scattering of light from a single particle allows for the calculation of the backward scattering cross section of particles based on the size resolved measurements. Assuming the olive oil droplets used in the calibration were spheres, the theoretical backscattering flux for light scattered over the angles in the backward direction collected by the CASPOL (168° - 176°) is attained using Mie theory and Equation 3 below (Baron and Willeke, 2001).

$$Backscattering\ \ Flux = \frac{4\pi I}{k^2} \times \int_{168°}^{176°} Backscatter_{Mie} \qquad \text{Equation 3}$$

where I is the laser intensity, k is the size parameter, ($k = \frac{2\pi}{\lambda}$), and λ is the wavelength of the CASPOL laser. $Backscatter_{Mie}$ is the calculated Mie response in the backward direction and is integrated over the collection angles of the CASPOL (168° to 176°). Theoretical backscattering fluxes are calculated for all particle sizes used in the olive oil calibration. A spline fitting function is then applied to the total backscattering intensity (measured) vs. the backscatter flux data (calculated) to generate a function for converting measured backscattering intensity to backscattering flux. Next, scattering cross sections σ, are determined by Equation 4.

$$\sigma = \frac{Backscattering\ \ Flux}{I} \qquad \text{Equation 4}$$

where I is the intensity of the incident CASPOL laser beam and the backscattering flux is taken from Equation 3.

Using this method, an approximate backscattering cross section was determined for a 2.5 μm spherical olive oil particle, $1.0x10^{-9}$ $cm^{-2}$. The following backscattering cross sections were calculated for 2.5 μm particles representative of the three compositions; $4.1x10^{-9}$ $cm^{-2}$ for hematite, $5.3x10^{-10}$ $cm^{-2}$ for white quartz, and $7.3x10^{-9}$ $cm^{-2}$ for zeolite. The CASPOL data collected here illustrates the high degree of variability in the optical properties of atmospheric dusts depending on source composition, as demonstrated by the aerosol backscattering cross sections which vary by a factor of 7 or more. Another implication of these results is that detection of particles using backward scattering techniques such as lidar are subject to a high degree of uncertainty.

## 4.12 Theoretical Dust Storm Signatures

While the laboratory data collected by the CASPOL is very promising, one consideration is that the particle concentrations generated in this study are drastically higher than those in the atmosphere. To test of the feasibility of using CASPOL to sample dust storm particles in-situ, we have produced scattering signatures based on an atmospherically relevant number concentration of particles during a high dust event. Iwasaka et al. (1983) reported dust concentrations of 50 $cm^{-3}$ (upper atmosphere) and 225 $cm^{-3}$ (lower atmosphere) during an Asian dust event. Similar values have been

reported by Gringel and Muhleisen (1977) and Prodi and Fea (1979). Thus, we estimate that a CASPOL mounted on an aircraft during flight through a hypothetical dust storm would sample ~50 dust particles per $cm^{-3}$ or more. Assuming the standard CASPOL flow rate (1.2 L $min^{-1}$), ≥ ~60,000 particles would be detected in a one minute sampling period within the dust storm. Applying the analysis technique described in Section 4.11, we generated signature plots for 60,000 particles of each dust type instead of the original concentrations approximately $10^5$ particles.

The results of this estimation can be seen in Figure 38, which shows that for the three representative dusts discussed, the shape, position and relative intensities of the signatures are comparable to the ones generated from the data with much larger aerosol concentrations (Figure 35). Thus we conclude that the same three Groups may be established, and that such data might be obtained when flying through a dust storm or during other intense atmospheric dust phenomena even when sampling times may be quite short.

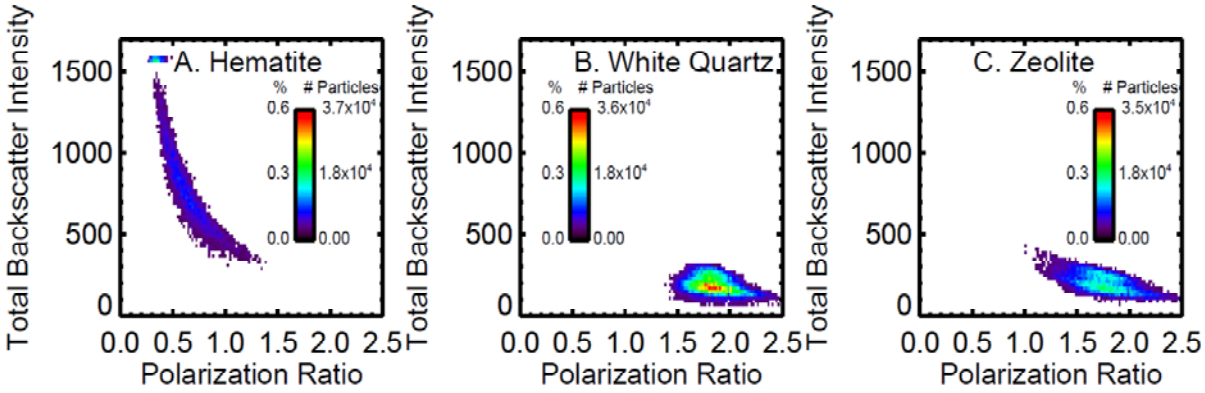


**Figure 38. The total backscatter intensity vs. polarization ratio for representative members of the optical scattering groups A (hematite), B (white quartz) and C (zeolite), using a total number of particles of 60,000.**

# 5. CLOUD AND AEROSOL SPECTROMETER WITH POLARIZATION - MK II

The previous version of the CASPOL instrument (MK I) was a prototype instrument constructed specifically for Texas A&M University under the instruction of Dr. Sarah Brooks. While this instrument served as a successful detector of differences in dust optical properties, it was not well constrained for measurements of absolute backscattering intensity and depolarization. To this end, DMT who manufactured the CASPOL made advances and upgrades to their production model instruments to build an instrument which accurately measured backscatter intensity and depolarization ratio.

## 5.1 Modifications to the CASPOL

The prototype CASPOL (MK I) was returned to DMT for modification and upgrade to match the currently available commercial units. A number of optical, electronic and firmware changes were required to make the CASPOL MK I operate like the current production CASPOL MK II unit. These modifications are listed below:

1) An improved beam splitter that is highly wave dependent.

2) Fixing problems within the depolarization circuitry which had been leading to a large percentage of unqualified particles to be counted.

3) Replacement of the CASPOL MK I sapphire window installed on the optical block faces with a new fused silica window to correct an elevated depolarization baseline due to the sapphire window.

The modifications made to the CASPOL optics and subsequent data collection/analysis lead to one significant change in the way data is processed. Due to the change in the instrument response to the measured light coming from the dusts, the

$$Total\ Backscatter\ Intensity\ (\beta_{Total}) = \beta_{\perp} + \beta_{\parallel} \qquad \text{Equation 5}$$

and therefore the

$$Depolarization\ Ratio = \frac{\beta_{\parallel}}{\beta_{Total}} \qquad \text{Equation 6}$$

## 5.2 Ice Measurements Using the CASPOL MK II

The following section is based on experiments conducted in laboratory using the CASPOL MK II and the Texas A&M CFDC and has been submitted to Aerosol Science and Technology for publication. The title of this article will be: Single Particle Measurements of the Optical Properties of Small Ice Crystals and Heterogeneous Ice Nuclei.

Dust aerosol and ice crystals are two major types of non-spherical particles in the atmosphere which have significant impacts on cloud-aerosol interactions and the radiative budget of the atmosphere. The presence of dust and ice often coincide in the atmosphere because dust is an effective ice nuclei. The size and composition dependant scattering properties of dust and ice are needed to determine the individual contributions of optical scattering of sunlight and the earth's radiative budget. Here we present a new measurement technique used to determine the single particle forward scattering,

backscattering, and depolarization ratio (at a wavelength of 680nm) for representative non-spherical atmospheric particles. The Texas A&M University Continuous Flow Diffusion Chamber (CFDC) is used as an ice crystal generator to produce ice crystals via both homogenous and heterogeneous nucleation mechanisms under well controlled laboratory conditions. Optical scattering properties of mineral dusts and small ice crystals (0.6 μm to 50 μm diameter) were measured by the Droplet Measurement Technologies, Inc (DMT) Cloud Aerosol Spectrometer with Polarization (CASPOL). Significant differences between the optical properties of single dusts and ice particles of the same size were observed. Differences between the optical signatures of homogeneously and heterogeneously nucleated ice crystals were not statistically significant. In addition, using assumed size distributions representative of dust and cirrus ice clouds in the atmosphere, we used the CASPOL single particle data to estimate the additive composite backscatter intensity and depolarization ratio for these populations of non-spherical particles in the atmosphere, and hence their contributions to the Earth's radiative budget. Our results suggest that atmospheric ice crystals can be identified and quantified independently from the dust particles on which they form based on analysis of their backscatter and depolarization signals.

## 5.3 Experimental Methods

In our previous work, we measured the optical properties of four dusts, including Arizona test dust, hematite, white quartz, and zeolite using a prototype version of the CASPOL instrument (Glen and Brooks, 2013). For direct comparison with ice crystal measurements here, optical properties of a subset of the dusts measured in Glen and Brooks (2013) are also observed by the upgraded CASPOL and are reported here. In addition, ice crystals were generated in a Continuous Flow Diffusion Chamber (CFDC) using and their optical properties were measured by the CASPOL.

The CASPOL measures the optical properties for individual particles in a range of sizes, from 0.6 μm < diameter ($D_p$) < 50 μm, using a diode laser at a wavelength of 680 nm. The CASPOL measures light scattered by individual aerosol particles in the forward (4° to 12°) and backward (168° to 176°) directions utilizing three detectors. The forward scattering detector (*f*) provides the size measurement of the sampled particles, and the two backward scattering detectors measure the parallel and perpendicularly polarized scattered light respectively. Note that the CASPOL used in this study differs from the prototype instrument used in Glen and Brooks (2013) in one major way, which is that instead of the back detector measuring the total intensity of light scattered in the back direction, the current CASPOL configuration employs an additional polarized filter which only allows scattered radiation which is parallel to the incident laser beam to be measured by this detector.

The arrangement of the detectors in the CASPOL provides the opportunity to measure differences in the optical scattering properties leading to the differentiation of particle types, spherical droplets, non-spherical dust, and ice crystals.

The relationship for calculating the Total Backscatter Intensity (TBI) is shown in Equation 7.

$$TBI = \beta_{\perp} + \beta_{\parallel} \qquad \text{Equation 7}$$

The parallel and perpendicular components of the backscattering signal can be used to calculate the in-situ depolarization ratio (DR) (Equation 8).

$$DR = \frac{\beta_{\parallel}}{\beta_{\perp}+\beta_{\parallel}} \qquad \text{Equation 8}$$

As the wavelength of the laser is similar to that of many remote sensing platforms, the CASPOL measures at nearly 180° backscatter, the CASPOL TBI and DR measurements can be compared to lidar data.

## 5.4 Mineral Dust Generation

The method used to generate mineral dust distributions has been described in the past (Glen and Brooks, 2013) and only a brief overview of this technique is included here. All of the dusts are commercially available; the Arizona test dust was purchased from Powder Technology Inc., and collected from 33.38°N, -112.31°E. The three other dusts, hematite, white quartz, and zeolite were purchased from Sigma Aldrich. For each

sample, a Topas Solid Aerosol Generator 410 (SAG) was used to generate a polydisperse aerosol distribution. The size distribution of the generated dust varied with dust type, with subtle differences in the dust size distribution being observed. The generated polydisperse distribution was then directed to a dilution chamber and subsequently sampled from the chamber by the CASPOL at a flow rate of 1.2 L $min^{-1}$, the setup for these experiments are shown in Figure 39. The CASPOL was used to measure the optical scattering properties of the dust sample until a minimum of $10^5$ particles were counted.

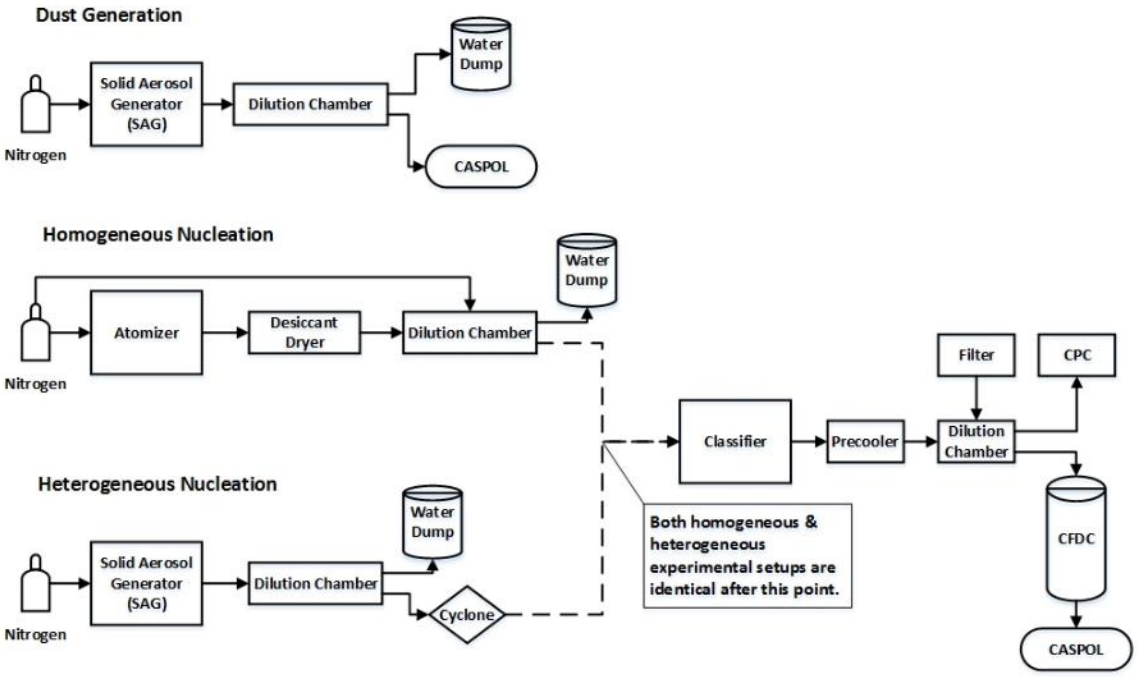


**Figure 39. Experimental setup for measuring the optical properties of dust, homogeneously nucleated ice crystals, and heterogeneously nucleated ice crystals are shown.**

## 5.5 Ice Crystal Generation

The CASPOL was used to measure the variation in the optical scattering properties of ice crystals generated by both homogenous and heterogeneous mechanisms using the Texas A&M CFDC (Hiranuma et al., 2013; McFarquhar et al., 2011). The CFDC is an instrument typically studies to measure the ice nucleation potential of aerosol (DeMott et al., 2011; Prenni et al., 2008; Prenni et al., 2007; Rogers et al., 2001a; Rogers et al., 2001b). The work conducted in this study is unique as this is the first time a CASPOL instrument has been coupled with a CFDC. The integration of these two instruments allows the CFDC to be used as an ice generator while the CASPOL is used to measure the optical properties under well constrained generation conditions.

An inlet at the top of the CFDC allows a pre-generated aerosol stream to enter an annular chamber where the sample air is sandwiched between two laminar flows of dry filtered air. The walls of the chamber are coated with ice and held at different temperatures which sets up a highly controlled supersaturation field between the two walls. As the aerosol samples travel through this controlled supersaturation region, they have the potential to nucleate and form ice crystals under chamber conditions specific to the aerosol (Rogers et al., 2001b).

For the generation of homogeneously nucleated ice crystals, the following method was used (Figure 39). First a solution of ammonium sulfate was atomized using a TSI 3076 Aerosol Generator (Atomizer). The polydisperse distribution was then dried using desiccant dryers and delivered to a large dilution chamber and mixed with dry

filtered air to reduce the number concentration. Next, the aerosol stream was directed to a TSI 3080 Electrostatic Classifier which generated a monodisperse distribution centered at 200 nm. Using IN particles with a diameter smaller than the lowest size measurement of the CASPOL ensures that the CASPOL does not miscount large dust particles as ice crystals if they have successfully travelled through the CFDC (Glen and Brooks, 2013). Next the sample stream flows to the custom built pre-cooler (set at -10 °C) for removing any remaining moisture on the particle and pre-cooling before it is split, with a portion sent to a TSI 3025A Condensation Particle Counter (CPC) and a portion of directed to the top of the CFDC. The sample stream then passes through the CFDC where nucleation and growth of ice crystal occurs. Exiting the CFDC, ice crystals are measured by the CASPOL. For all homogenous experiments in this study, the CFDC conditions were set for an aerosol processing temperature of approximately -55 °C ± 0.2 °C and supersaturations with respect to ice of 51 % ± 2.3 %.

For the heterogeneous IN experiments in this study, the four mineral dusts, Arizona test dust, hematite, white quartz, and zeolite were used as potential IN. For each of the four mineral dusts, a polydisperse distribution was initially generated using the SAG (Figure 39). The generated dust particles were then sent to a dilution chamber to reduce the total number concentration. After which the diluted aerosol stream entered a cyclone impactor to remove any particles larger than 1.5 µm. From the cyclone, a TSI 3080 Electrostatic Classifier was used to size select only particles with a with a mode diameter of 200 nm. The method then follows that of the homogeneous generation, with the monodisperse sample passing through a pre-cooler and mixing chamber before being

sampled by the CPC, CFDC, and CASPOL, as shown in Figure 39. For heterogeneous nucleation experiments the CFDC was controlled to produce an aerosol stream temperature of approximately -56 °C ± 0.1 °C and supersaturations with respect to ice of 56 % ± 4.3 %. This supersaturation is well below water saturation (~ -10 %), it is expected that ice nucleating in the CFDC will occur by depositional freezing only.

## 5.6 Experimental Results

Based on the forward scattering CASPOL measurements, the polydisperse mineral dusts displayed show tri-modal size distributions of high particle concentrations (not shown). Under the chosen CFDC conditions, all mineral dusts acted as efficient IN. High concentrations (~ 3 - 1500 $L^{-1}$) of ice crystals were produced in all homogenous and heterogeneous experiments and sampled by the CASPOL. Previous studies have shown the ability of various mineral dusts to act as IN (Archuleta et al., 2005; Atkinson et al., 2013; Koehler et al., 2010; Murray et al., 2012). Atkinson et al. (2013) show that feldspar minerals are the most efficient IN with nucleation occurring at temperatures near 255 K (-18 °C), quartz had nucleation occurring around 247 K (-26 °C), whereas homogenous nucleation began at 238 K (-35 °C). In addition, Archuleta et al. (2005) show that hematite can begin to nucleate at 228 K (-45 °C). These previous studies all indicate a large variation in the nucleation conditions for varying dust types.

CASPOL data collection allows comparison of dust and ice, on a single particle-by-particle basis as well as the comparison of ensembles of each particle type. Total

backscattering intensity and depolarization ratio measured for hematite particles and ice nucleated using hematite as the IN are shown in Figure 40. As seen in Figure 40A, the generated ice crystals have a relatively constant total backscatter intensity, approximately 50 arbitrary units (a.u.) over the particle size range of 0.6 μm to 10 μm. The standard deviation is relatively low, indicating the variation in total backscatter intensity is small. In contrast, the hematite dust shows a general increase in total backscatter intensity as a function of particle size ranging from 100 arbitrary units to 400 arbitrary units over the size range from 0.6 μm to 10 μm. The observed increase in total backscatter intensity is generally expected with increasing particle size, similar to that of spherical particles using Mie theory (Hinds, 1999). However, the near constant total backscatter intensity results for the ice crystals are unexpected. No definitive reason for this can be confirmed from this data set.

The depolarization ratio as a function of the particle diameter for dry hematite dust and ice crystals is shown in Figure 40B. The results show a difference between the dry hematite dust, and nucleated ice crystals of like size. Across the measured size range, 0.6 μm to 10 μm, the hematite dust has a relatively low depolarization ratio, with very low standard deviations for each particle type. The ice crystals formed from nucleated hematite dust have much higher depolarization ratios, 2 to 3 times higher than the hematite dust for many size bins. In addition, the ice crystals also have much larger standard deviations from the mean depolarization ratio. The average variation across all the particle sizes collected is ~ 260 %, which is very similar to the variation (270 %) observed by Clavano et al. (2007) for the depolarization ratios measured for very

irregular particles. The highest variation in DR for a single size bin is 500% in the case of 3 μm ice crystals. In general, the deviations in depolarization ratio are higher for the smaller ice crystals (Dp < 3 μm) than large ice crystals. Cho et al. (2008) show that optical scattering signals with low total backscatter intensity and relatively high depolarization ratio are associated with randomly oriented ice crystals.

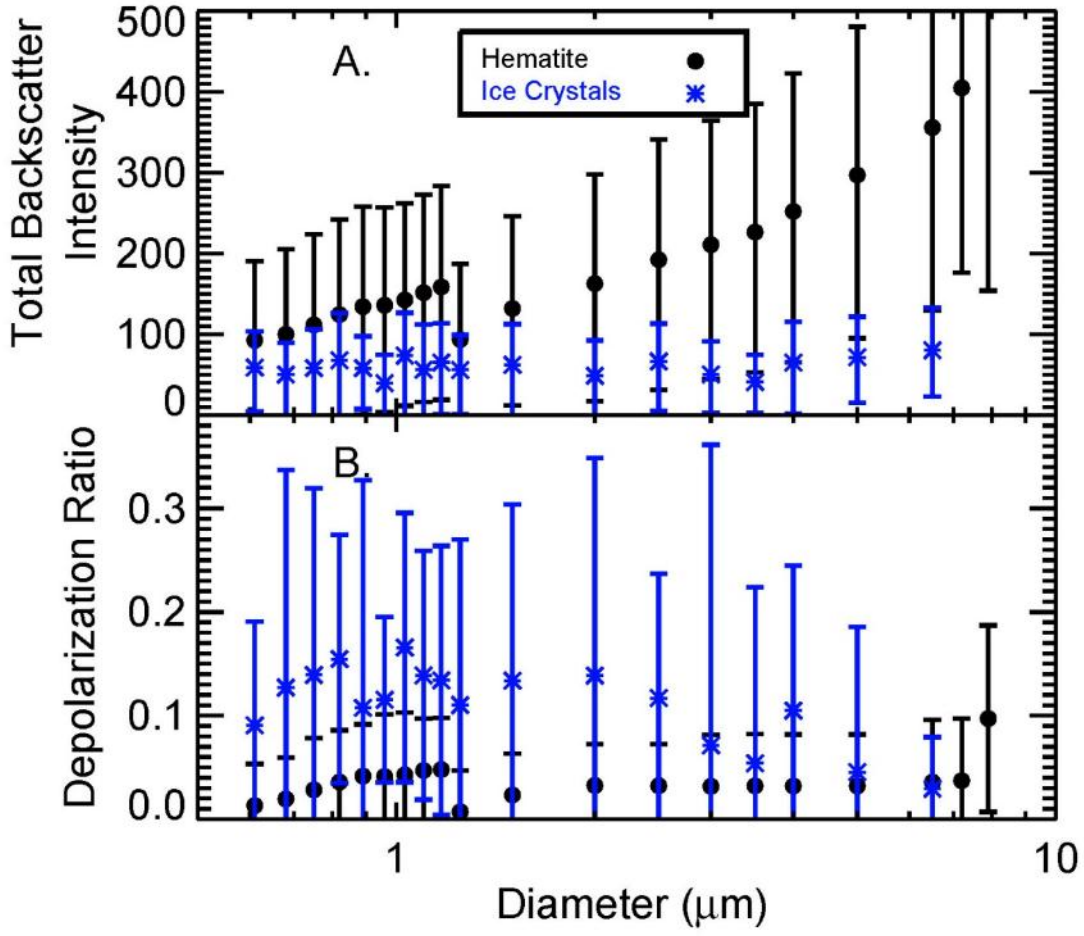


**Figure 40. The differences in the optical properties of dust and ice for particles of the same size, specifically the variation in total backscatter intensity (panel A) and depolarization ratio (panel B) as measured by the CASPOL for dry hematite dust and ice crystals nucleated using hematite dust as an IN.**

Next we look for differences between the optical properties of additional dust and ice crystals. Figure 41 shows the variation in the CASPOL measured optical properties for all four mineral dusts and the ice crystals heterogeneously nucleated on these dusts when acting as IN within the CFDC. In Figure 41A, it can be seen that three out of the four mineral dusts have a relatively low total backscatter intensity (< 100 arbitrary units) over the particle size range from 0.6 μm to 5 μm. Hematite is the exception and has much higher total backscattering intensities for smaller particle sizes compared to the other dusts. At diameters above 5 μm all the dusts show an increasing trend in total backscattering intensity.

The heterogeneously nucleated ice crystals also have relatively low total backscattering intensities. These intensities were almost identical for three of the four IN types. The only heterogeneous ice crystals which showed variation in the total backscatter intensity were those nucleated on Arizona test dust. Results based on three of the four sampled dusts scattering intensities suggest that while IN type may influence nucleation conditions and relative rates (Archuleta et al., 2005; Atkinson et al., 2013) the resulting ice crystals possess similar shapes and optical properties. One exception to this is that ice crystals nucleated on Arizona test dust have total backscatter intensities approximately twice as high as the other three ice crystal samples. The total backscatter intensity alone is not enough to reliably differentiate between mineral dust particles and ice crystals.

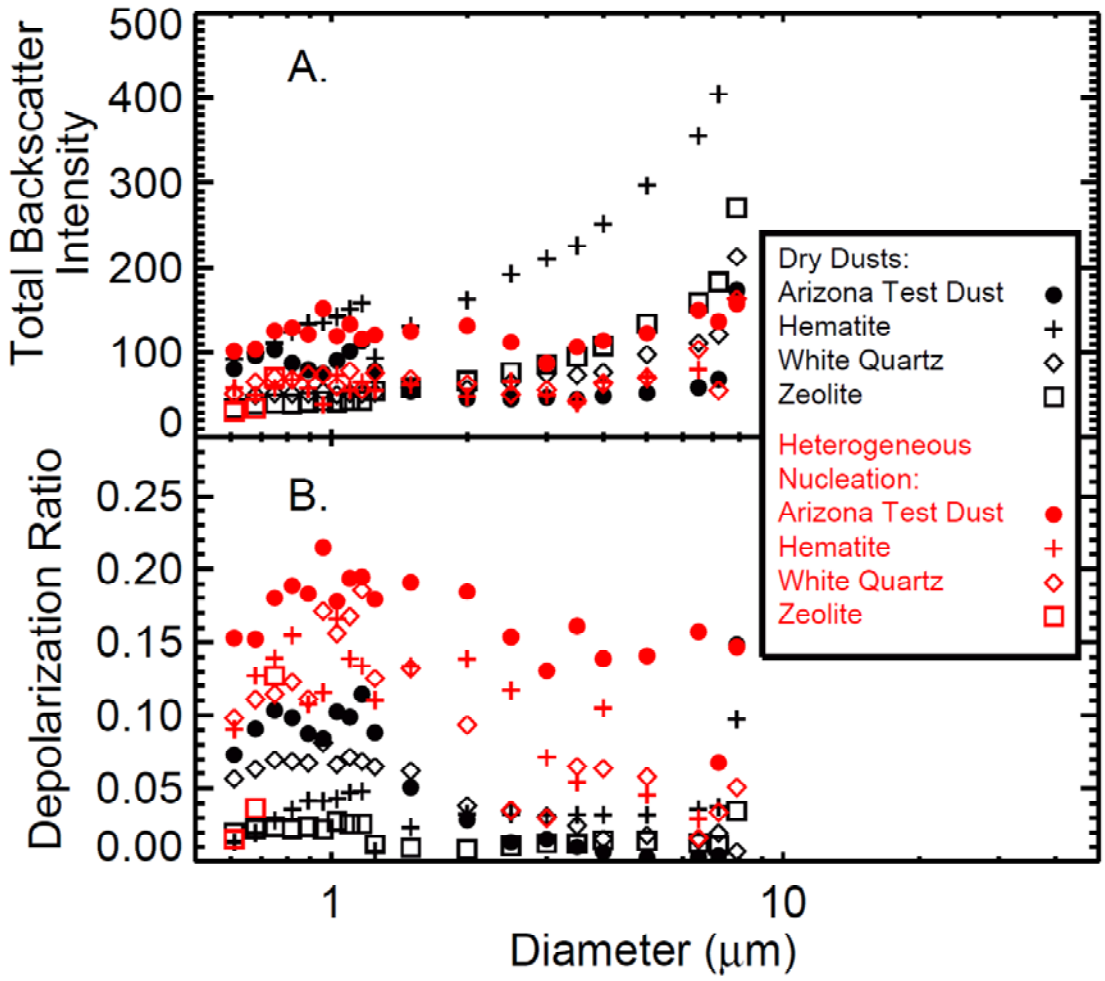


**Figure 41. The total backscatter intensity (panel A) and depolarization ratio (panel B) for mineral dusts (black symbols) and ice crystals generated using 200 nm particles of each mineral dust type as the heterogeneous IN (red symbols).**

The differences in the depolarization ratios of mineral dusts and nucleated ice crystals as a function of the particle diameter can be seen in Figure 41B. Generally the figure shows that the mineral dusts have a depolarization ratio less than 0.1 for particle sizes between 0.6 μm and 1.5 μm. Above 1.5 μm the depolarization ratio for mineral dusts decreases to less than 0.05 for all dust types. The heterogeneously nucleated ice

crystals show higher depolarization ratios between 0.10 and 0.22 for ice crystals with diameters between 0.6 μm and 2.0 μm, after which the ice crystals formed using white quartz and hematite IN have a reduced depolarization ratio of approximately 0.05. These results indicate that ice crystals and mineral dusts can be differentiated using the depolarization ratio likely due to the ice crystals highly irregular shape, which is less prevalent for the mineral dusts.

Figure 42 shows the average total backscatter intensity (Panel A) and depolarization ratio (Panel B) as a function of particle diameter for both the homogeneous and heterogeneous ice experiments. For the homogeneous experiments, the total backscatter intensity average is calculated from the scattering data measured during the four experimental datasets using 200 nm ammonium sulfate particles and exposed to CFDC conditions of -55 °C ± 0.2 °C and supersaturations with respect to ice of 51 % ± 2.3 %. The heterogeneous mechanism average total backscatter intensity is calculated using the scattering data collected for the nucleation of the four dust types, Arizona test dust, hematite, white quartz and zeolite. The ice crystals generated in the homogeneous freezing experiments are depicted by blue diamonds, and the ice crystals activated heterogeneously are shown by red squares in Figure 42. The standard deviation calculated for both nucleation mechanisms specific data sets are also shown in the figure. As Figure 42A shows, there is very little difference in the total backscatter intensity of ice crystals nucleated by the two nucleation mechanisms. For many size bins, the standard deviation overlaps between the two mechanisms. Both the

homogeneous and heterogeneously nucleated ice crystals span the range of total backscatter intensities from ~ 50 to 175 a.u.

Figure 42B illustrates the depolarization ratios for ice crystals nucleated by homogeneous and heterogeneous nucleation mechanisms. The measured ice crystals initiated by both freezing mechanisms showing a similar general curve in DR as function of size. However, the data from the homogeneous nucleation experiments show slightly higher depolarization ratios which may be attributed to slightly more irregular shaped particles than particles formed from heterogeneous nucleation. The difference in the optical properties of these two mechanisms is not as pronounced as one might expect based on ice crystal shapes observed in other studies (Bailey and Hallett, 2004). Several potential reasons for this exist. The first is that we are only measuring small ice crystals, whereas most other studies (Baum et al., 2005b; Baum et al., 2010; Curtis et al., 2007; Curtis et al., 2008) of the optical properties of ice crystals have been conducted on particles on the order of 100 μm where the shape of the particle is more easily determined and subsequently the particles effect on the scattering of light is easier to observe. Also experimental limitations may cause melting of the ice crystal edges during both the homogeneous and heterogeneous experiments leading to the similar optical scattering signatures. Finally, if the CASPOL were modified to measure optical properties at additional angles, it may be possible to gain the necessary information to observe the fine scale changes in the optical properties of very small ice crystals formed by different mechanisms.

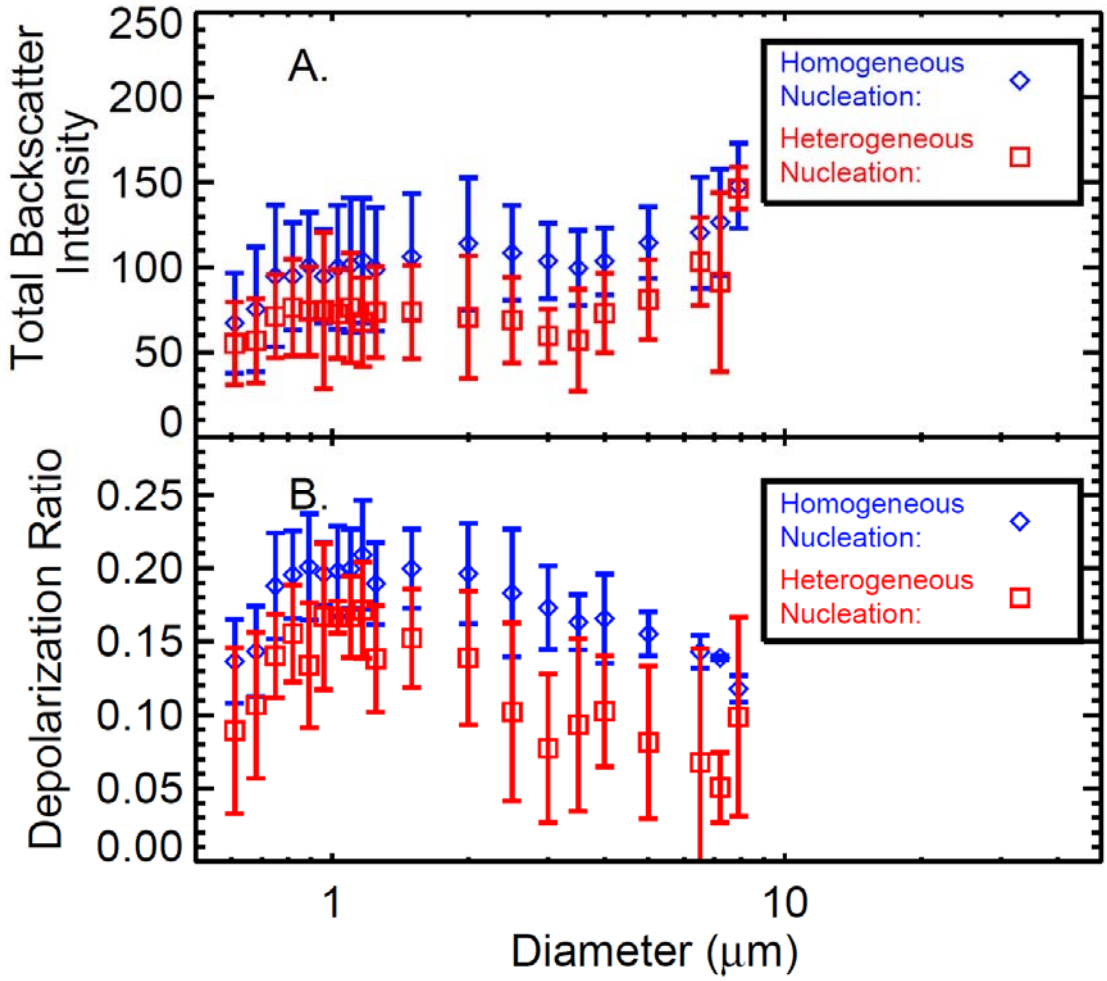


**Figure 42. The average total backscatter intensity (panel A) and depolarization ratio (panel B) as a function of particle diameter for ice crystals nucleated by the average 200 nm ammonium sulfate homogeneous and the average of the four heterogeneously nucleated dusts are shown as blue diamonds and red squares, respectively. The heterogeneous data is composed of the average nucleation data using all four mineral dusts as IN.**

Next, the CASPOL data is used to examine the range of observed total backscattering intensities for a single size bin in an effort to further differentiate between dust particles and ice crystals (Figure 43). For the 2.5 µm to 3.0 µm CASPOL channel only, the frequency of particles of a given total backscatter intensity are shown for; four

dust types, the heterogeneously-nucleated ice crystals (combined from all heterogeneous nucleation experiments), and homogeneously nucleated ice crystals (combined from all homogeneous nucleation experiments) and are plotted in Figure 43A. The same treatment of the data for the CASPOL size channel from 7.2 μm to 7.9 μm is shown in Figure 43B, the frequency of particles of a given total backscatter intensity are shown. Figure 43 shows that for each of the particle types sampled with the CASPOL, Arizona test dust, hematite, white quartz, zeolite and both homogenously and heterogeneously generated ice crystals there are large variations in the total backscatter intensity distribution even within a narrow size range.

For the 2.5 μm to 3.0 μm channel, hematite has the largest variation in total backscatter intensity, ranging from 0 to over 800 au. Four of the particle types, Arizona test dust, white quartz, heterogeneous and homogeneous ice crystals all have a similar spread in the total backscatter intensity variation with the maximum measured total backscatter intensities of approximately 250 a.u. For all the dust types, the distribution of total backscatter intensities is weighted toward the lower end of the range, < 20 a.u. For the heterogeneously nucleated ice crystals, the maximum percentage of particles is also found when the total backscatter intensities are < 20 a.u. In contrast, for homogeneously nucleated crystals, the mode of the distribution is centered at a higher total backscattering intensity, ~75 a.u.

The relative distribution of intensities for 7.2 μm to 7.9 μm size bin reflect those of the same particle composition in the smaller size bin. For instance, the highest total backscattering intensities and widest range of intensities are observed for hematite, and

the second highest intensities and range are zeolite, in both size bins. For all particle types, the distribution of total backscattering intensities of 7.2 μm to 7.9 μm particles is shifted to higher values, relative to the 2.5 μm to 3.0 μm particles. Overall, the distributions of intensities are broader for the large size, suggesting greater variability in the shapes of the larger particles.

The results of these experiments show that mineral dust and ice crystals can be differentiated based on their total backscatter intensities and depolarization ratios. In addition, the results indicate that all four dusts, Arizona test dust, hematite, white quartz, and zeolite can act as IN for heterogeneous nucleation at controlled experimental conditions within the CFDC of -55°C and 50 % supersaturation with respect to ice, in general agreement with previous studies (Murray et al. (2012) and references within). While the total backscatter intensities and depolarization ratios are slightly higher for homogeneously nucleated ice crystals than for heterogeneous ones, the differences are not statistically significant. Hence, future in-situ CASPOL measurements may be used to differentiate between dust and ice crystals, but not between homogeneously and heterogeneously nucleated ice crystals.

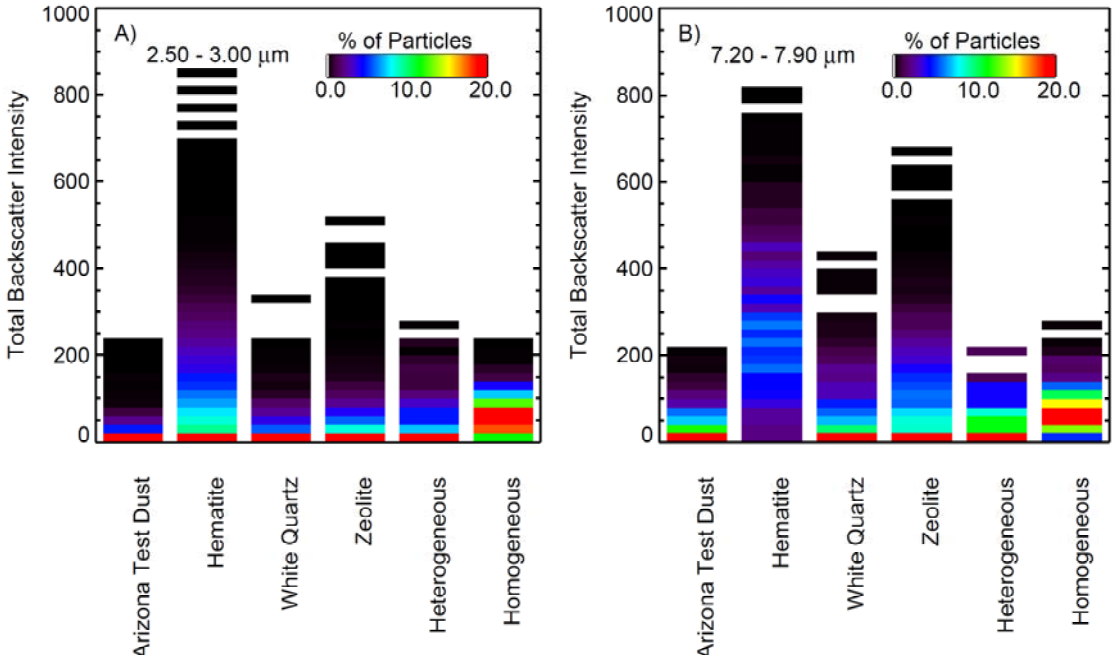


**Figure 43 Panel A. For the 2.5 µm to 3.0 µm CASPOL channel only, the frequency of particles of a given total backscatter intensity are shown, for four dust types, heterogeneously-nucleated ice crystals, and homogenously nucleated ice crystals. The legend indicates the percentage of 2.5 to 3.0 µm diameter particles which have the total backscatter intensity indicated on the ordinate axis. Panel B is for the 7.2 µm to 7.9 µm size bin, the frequency of particles of a given total backscatter intensity are shown.**

The results of these experiments show that under controlled conditions mineral dust and ice crystals can be differentiated based on their backscatter intensity and depolarization ratio. In addition it was shown that all four dusts, Arizona test dust, hematite, white quartz, and zeolite can act as IN for heterogeneous nucleation at controlled experimental conditions within the CFDC of -55°C and 50 % supersaturation with respect to ice. However, the differentiation of ice crystals generated by different nucleation mechanisms is not easily identifiable.

## 5.7 Development of Composite Atmospheric Aerosol Depolarization Ratios

Since the optical properties of scattered light are additive, the CASPOL single particle data can be used to estimate the optical properties of ensembles of particles in the atmosphere. The composite method employed here relies on the CASPOL's ability to act as a single particle instrument. A similar approach has been used in previous studies to relate stratospheric cloud particle properties to lidar measurements (Brooks et al., 2004; Toon et al., 2000). First, representative size distributions were obtained from the literature for recent field measurements of mineral dust and ice crystals. From the Saharan Mineral Dust Experiment (SAMUM), 19 dust particle size distributions were collected during aircraft studies from May to June 2006, from which the data were averaged to generate the average distribution used here (Weinzierl et al., 2009). In a previous study, representative ice crystal size distributions based on data collected during both Cirrus Regional Study of Tropical Anvils and Cirrus Layers - Florida Area Cirrus Experiment (CRYSTAL-FACE) and First International Satellite Cloud Climatology Project Regional Experiments (FIRE II) were obtained (Baum et al., 2005a). In that study, the particle distributions were then filtered by cloud temperature ($T_{cloud} < -25°C$) to ensure the particles measured were ice crystals. The total number of remaining particle size distributions for CRYSTAL-FACE was 41 and of FIRE II was 22. From these remaining ice crystal size distributions, a representative sample was reported for both CRYSTAL-FACE and FIRE II, and were subsequently used in this analysis.

The size distributions for these three events, SAMUM, CRYSTAL-FACE and FIRE II were used to represent size distributions of three specific atmospheric events; 1) dust storms, 2) tropical cirrus clouds and 3) mid-latitude ice clouds. The log normal fitting parameters based on a tri-modal distribution for particles observed during the specific events within these three field campaigns are shown in Table 4. Log normal fitting functions and resulting composite backscatter intensity and composite depolarization ratios.. The size distribution data from each of the three field study cases were then combined with the optical scattering properties of dust and ice measured in the laboratory to produce a Composite Backscatter Intensity (CBI) and a Composite Depolarization Ratio (CDR). For example, the SAMUM data was first discretized into 30 particle diameters corresponding to the 30 size channels of the CASPOL instrument. Each particle diameter in the SAMUM size distribution is assigned values for the single particle backscatter and depolarization ratio based on the CASPOL optical scattering data for the corresponding particle diameter.

The equations used to calculate composite backscatter and depolarization are shown in Equation 9 and Equation 10. These derived parameters are for particle scattering only, and do not take into account Raleigh scattering by gas molecules.

$$CBI = \sum_{i=1}^{30} N_i\left(\beta_{\perp_i} + \beta_{\parallel_i}\right) \qquad \text{Equation 9}$$

$$CDR = \sum_{i=1}^{30} N_i \left(\frac{\beta_{\perp_i}}{\beta_{\perp_i}+\beta_{\parallel_i}}\right) \qquad \text{Equation 10}$$

where i is the size bin index (i=1-30) corresponding to the CASPOL size bins between 0.6 μm and 50 μm, $N_i$, is the particle concentration in each SAMUM discretized bin based on the size distribution, $\beta_{\perp i}$ is the average intensity measured by the CASPOL's perpendicular backscatter for the size bin, and $\beta_{\parallel i}$ the average intensity measured by the CASPOL parallel backscatter detector for the corresponding size bin.

The calculated composite optical scattering properties are shown in Table 4. Log normal fitting functions and resulting composite backscatter intensity and composite depolarization ratios. CBI values are reported in arbitrary units and values of CDR are unit less. The results show that the dust is highly scattering and has a high depolarization ratio, which we attribute to its irregular shape. The estimates of the CBI and CDR for both ice events, (tropical cirrus cloud and mid-latitude ice cloud) are several orders of magnitude lower than that of the dust event. However, the estimates for ice crystals may be a conservative underestimate due to the lack of optical scattering property data measured by the CASPOL for particle sizes larger than 10 μm

This method has unique applications as it provides a way of relating laboratory derived scattering properties of particles and ice crystals to remote sensing retrievals. It has been suggested (Yang and Liou, 2006) that small ice crystals also have an important effect on the radiative balance of the atmosphere, our results confirm this but show that large concentrations of dust have a larger impact. Nevertheless, the estimation of the composite parameters illustrates the potential use of in-situ particle-by-particle measurements of particle optical properties by the remote sensing community.

**Table 4. Log normal fitting functions and resulting composite backscatter intensity and composite depolarization ratios.**

| Type | Campaign | Mode 1 N ($cm^{-3}$) | Mode 1 CMD (µm) | Mode 1 σ | Mode 2 N ($cm^{-3}$) | Mode 2 CMD (µm) | Mode 2 σ | Mode 3 N ($cm^{-3}$) | Mode 3 CMD (µm) | Mode 3 σ | Total Composite Backscatter Intensity (A.U.) | Total Composite Depolarization |
|---|---|---|---|---|---|---|---|---|---|---|---|---|
| Dust | SAMUM | 938 | 0.073 | 1.95 | 71 | 0.37 | 1.58 | 21 | 1.02 | 2.04 | $11.0 \times 10^{6}$ | $9.8 \times 10^{5}$ |
| Tropical Cirrus | CRYSTAL FACE | 64 | 12.15 | 1.64 | 180.1 | 29.25 | 1.59 | 90.06 | 58.65 | 1.45 | 0.81 | 0.12 |
| Mid-latitude Cirrus | FIRE II | 7 | 30.16 | 1.75 | 23.83 | 74.22 | 1.49 | 51.8 | 157.18 | 1.49 | $9.0 \times 10^{-3}$ | $1.2 \times 10^{-3}$ |

## 5.8 Scattering Signatures for MK II Data

As four of the thirteen dusts used in Section 4 were used in this study it is prudent to analyze the data to produce scattering signatures similar to those seen in Figure 35 and Figure 36. The four dusts chosen for this study were Arizona test dust, hematite, white quartz and zeolite, these dusts were chosen for their apparent ice nucleation abilities and as representative dust types of the optical scattering groups first established by the CASPOL MK I in Section 4 and Glen and Brooks (2013). This analysis is important twofold, 1) to identify any differences in the optical properties between each of the four dusts measured by the CASPOL MK II, and, 2) to compare the scattering signatures between the prototype CASPOL MK I and CASPOL MK II. The scattering signatures were produced using the same method as those for Figure 35 and Figure 36, however now the total backscatter intensity and depolarization ratio are represented by Equation 7 and Equation 8.

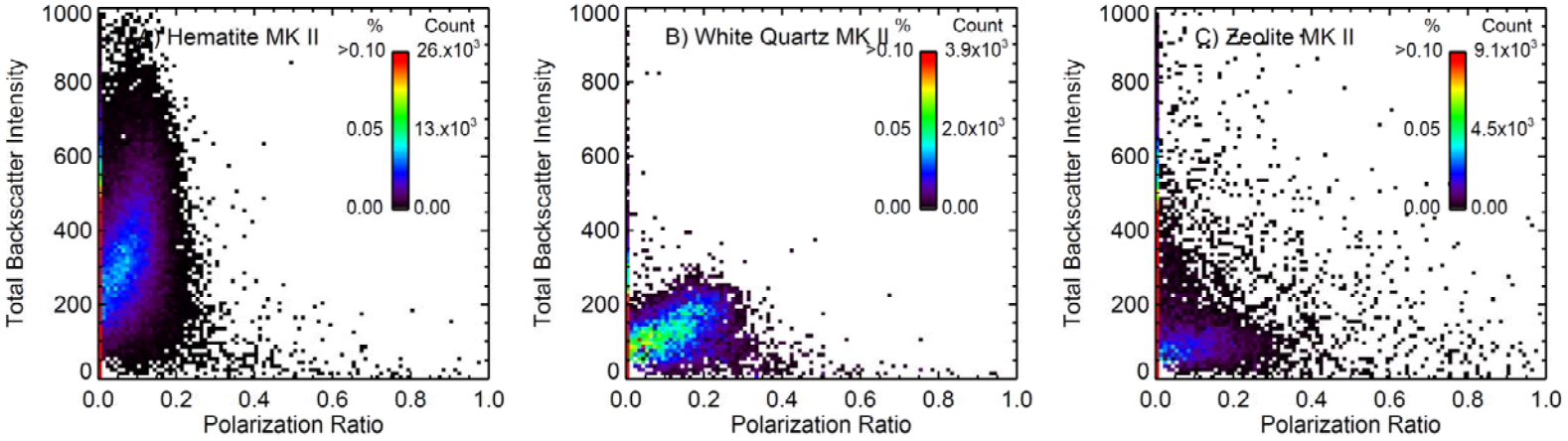


**Figure 44. Polarized backscatter to forward scatter ratio vs. total backscatter to forward scatter ratio for representative members of the optical scattering groups A (hematite), B (white quartz) and C (zeolite) are shown.**

The results of this analysis for hematite, white quartz and zeolite can be seen in Figure 44 for the total backscatter intensity vs. depolarization ratio. The results of the total backscatter intensity vs. the depolarization ratio show three potential groups again, the first for hematite (Panel A) shows depolarization ratios less than 0.3 with total backscatter signals ranging from 0 to 1000 arbitrary units. The second group (Panel B), found using white quartz has depolarization ratios ranging from 0 to 0.4 and total backscatter intensities less than 200, with very high maximum intensities. The final group (Panel C), using zeolite illustrates a poor correlation signature with depolarization ratios ranging from 0 to 0.4 and total backscatter intensities ranging from 0 to 400 arbitrary units. These optical scattering signatures indicate that the dusts sampled in this study using the CASPOL MK II can be differentiated using their optical scattering properties. The scattering signatures for 13 atmospherically representative dusts are shown in Figure 53 of Appendix C for reference.

# 6. CONCLUSIONS AND FUTURE WORK

The following section discusses conclusions drawn from the work presented in this Thesis. In addition, future work is also suggested with improvements for instrumentation and potential designs of components using Solidworks are shown in Appendix B.

## 6.1 CFDC Conclusions

The Texas A&M University CFDC instrument was constructed and deployed in both laboratory and field operations. The design and construction including the refrigeration system were discussed. Additionally, the characterization of the temperature profile, cyclone impactor and residence time within the chamber was undertaken, including the development of support instrumentation such as the pre-cooler.

A thorough characterization of the CFDC was completed using silver iodide and ammonium sulfate IN. The results show an increase in the IN/CN ratio, as a function of increasing $SS_{ice}$ and as a function of temperature indicating that the instrument is successfully activating IN and growing ice crystals through condensation, immersion and depositional nucleation. The CFDC OPC correctly identified the difference between aerosol and activated IN which formed ice crystals.

## 6.2 ISDAC - Conclusions

ISDAC was the first deployment of the Texas A&M CFDC. This project took place in April 2008, near Barrow, AK. The CFDC successfully operated onboard the Environment Canada Convair 580 aircraft in combination with approximately 40 other instruments. The CFDC was operational for over 30 sorties in and around Barrow, AK.

The data collected during ISDAC showed high variability in the IN concentration with average lower concentrations of less than 0.1 $L^{-1}$ to upper averages of 100 $L^{-1}$, with no clear trends over the entire campaign. Individual flights displayed interesting "extreme" nucleation events which were controlled by both IN particle size and composition, leading to no clear conclusion to which factor is the most important in ice nucleation in the Arctic. These events were short lived plumes of varying IN under differing atmospheric conditions and CFDC operating conditions.

The measurements made during ISDAC are very different from those made during M-PACE in the fall of 2004. M-PACE data show that the Arctic environment is pristine during the fall season where the IN concentration were less than 1 $L^{-1}$, and below the CFDC's detection threshold 85 % of the time (Verlinde et al., 2007). During ISDAC the CFDC was only below the detection limit for approximately 30% of the measurements, a large difference from that seen for M-PACE. This contrast between ISDAC and M-PACE data suggests a strong seasonal dependence on the aerosol available to act as potential IN in the Arctic, in addition to the variation by composition or IN diameter.

## 6.3 CASPOL MK I - Conclusions

A new instrument, the CASPOL, was tested in a series of laboratory experiments using representative atmospheric dust samples available through commercial sources, and samples collected in various locations in Saudi Arabia and the Southwestern United States. The CASPOL data show a large variation in total backscatter intensity and polarization ratio as a function of dust type and particle size. Predicting the optical properties of aerosols is a challenge because of the multiple factors on which such properties depend, including a particle's composition, refractive index, aspect ratio, shape, and surface roughness. As these properties vary together rather than independently, it is generally not possible to extract cause and effect relationships between a single particle property and the resulting scattering properties. Since the CASPOL provides optical information on a single particle basis, the effects of size can be considered relative to other properties. However, because multiple particle properties varied even within a single size, defining their individual influence on optical properties was not possible.

For ensembles of particles, it was found that the plots of polarization ratio vs. total backscattering intensity could be used to differentiate between various types of dust. Differences in the optical scattering signatures observed in these plots were used to sort twelve of the thirteen surveyed dust types into three distinct groups. Only one dust, Arizona Test Dust, did not fit into any of these categories. Optical scattering signatures from the CASPOL data were used to develop a set of rules which can be used for

classification of additional dusts sampled in the laboratory and during field campaigns. An analogous approach has been used to analyze backscatter signals and depolarization ratios observed by Cloud-Aerosol Lidar and Infrared Pathfinder Satellite Observations (CALIPSO) to infer cloud types (Cho et al., 2008). While not addressed in this manuscript, it is likely feasible to use CASPOL polarization ratio to backscattering intensity plots to differentiate between in-situ liquid droplets and nonspherical ice crystals. Thus, the CASPOL's potential as a field instrument may include characterization of cloud particles as well as dust.

We also demonstrated that using CASPOL data collected on individual components and the known ratio of those components, the overall optical signature for Arizona test dust can be predicted. While additional measurements of this type on other mixtures of dusts are needed, this implies that the Arizona test dust sample was externally mixed and that the optical properties of other atmospheric external mixtures may also be predicted through laboratory CASPOL measurements of their components.

Calculated backscattering cross sections show a factor of 7 difference between representative dust samples. This study demonstrates that dusts with different source regions and compositions have large variations in optical properties and ultimately in the scattering cross sections. As illustrated by the two Saudi Arabian samples, even a small change in geographical location may result in atmospheric dust with different optical properties.

In summary, the CASPOL provides valuable particle-by-particle measurements of size, total backscatter intensity and polarized backscatter intensity. Even within a

narrow size range, scattering was observed to vary distinctly depending on the dust type. Differences are most likely due to a complex relationship between the size, shape, morphology, composition and refractive index. Although it was not possible to identify the dominant trait causing the differences in the optical properties observed here, a major finding of this work, that various dust types have distinctly different optical properties, has ramifications for other applications in atmospheric science. For example, our results imply that due to differences in aerosol shape and composition, lidar backscattering could vary greatly, even for dust particles of the same particle size (Brooks et al., 2004). Clearly, mineral dust type should be taken into account in interpretation of lidar data. Also, in future radiative transfer studies, the CASPOL data may be used to improve particle phase functions in which assumed particle size and shape are modified to produce backscattering cross sections consistent with the CASPOL observations. Such information will ultimately result in better remote sensing measurements, more accurate radiative transfer calculations, and a better understanding of aerosol direct effects on climate.

## 6.4 CASPOL MK II - Conclusions

This study used a new single particle scattering instrument, the second generation CASPOL, to measure the forward and backward scattering with dedicated detectors for both the parallel and perpendicularly polarized backscatter components. Using

combinations of the measured signal from these detectors the total backscatter intensity and depolarization ratio on a particle-by-particle basis was calculated.

Single particle optical scattering measurements of dust and ice crystals generated in a both homogeneous and heterogeneous ice nucleation experiments in a CFDC were measured by the CASPOL. The optical properties of homogeneously and heterogeneously nucleated ice crystals were not significantly different under the experimental conditions utilized here. However, the single particle properties of dust particles and ice crystals clearly differ in both the total backscattering intensity and depolarization ratio for particles of the same diameter.

Based on the measured data set, composite backscatter intensity and depolarization ratios for atmospheric, dust, were estimated. The results of which showed large variability between the dust and ice crystals. The dust storm produced the largest value of composite backscatter intensity. CBI estimates for both cirrus clouds, and mid-latitude ice clouds were several orders of magnitude smaller. A caveat to this, is the limit in the size range of CASPOL data which was for $Dp < \sim 9$ μm. In the atmosphere there are relatively large concentrations of ice crystals larger than this cut off size which would impact the total composite backscatter intensity.

Overall, this study presents a new technique for the measurement of mineral dusts and ice crystals. The unique measurements presented here illustrate the differences in the optical properties of dust and ice crystals, shedding light on the impacts of both particle types on the global atmospheric radiative balance. The differences found between the dust types and ice crystals sampled allows a better understanding of the

optical properties of these particles and subsequently the opportunity to differentiate between these two particles subtypes using in-situ and remote sensing platforms. The laboratory results obtained here suggest that the optical scattering properties of dust and ice may potentially be used in-situ as a method for identifying the particle type. In addition, these data may potentially provide inputs into analysis of remote sensing data to gain a greater understanding of dust storm events, ice crystals in clouds, and the interaction between the dust and nucleation of the ice crystals.

# REFERENCES


Arakawa, E. T., Tuminello, P. S., Khare, B. N., Millham, M. E., Authier, S., and Pierce, J.: Measurement of optical properties of small particles, 1997 scientific conference on obscuration and aerosol research, Aberdeen Proving Ground, MD (United States), 23-27 June 1997, OSTI ID: 627449; Legacy ID: DE98001913, 1997.

Archuleta, C., DeMott, P., and Kreidenweis, S.: Ice nucleation by surrogates for atmospheric mineral dust and mineral dust/sulfate particles at cirrus temperatures, Atmospheric Chemistry and Physics, 5, 2617-2634, 2005.

Atkinson, J. D., Murray, B. J., Woodhouse, M. T., Whale, T. F., Baustian, K. J., Carslaw, K. S., Dobbie, S., O/'Sullivan, D., and Malkin, T. L.: The importance of feldspar for ice nucleation by mineral dust in mixed-phase clouds, Nature, advance online publication, doi: 10.1038/nature12278, 2013.

Attwood, A. R., and Greenslade, M. E.: Optical properties and associated hygroscopicity of clay aerosols, Aerosol Science and Technology, 45, 1350-1359, doi: 10.1080/02786826.2011.594462, 2011.

Bailey, M., and Hallett, J.: Growth rates and habits of ice crystals between −20° and −70°C, Journal of the Atmospheric Sciences, 61, 514-544, doi: 10.1175/1520-0469(2004)061<0514:grahoi>2.0.co;2, 2004.

Baron, P. A., and Willeke, K.: Aerosol measurement - Principles, techniques, and applications, Second Edition, John Wiley & Sons, Canada, 2001.

Baum, B. A., Heymsfield, A. J., Yang, P., and Bedka, S. T.: Bulk scattering properties for the remote sensing of ice clouds. Part I: Microphysical data and models, Journal of Applied Meteorology, 44, 1885-1895, doi: 10.1175/JAM2308.1, 2005a.

Baum, B. A., Yang, P., Heymsfield, A. J., Platnick, S., King, M. D., Hu, Y. X., and Bedka, S. T.: Bulk scattering properties for the remote sensing of ice clouds. Part

II: Narrowband models, Journal of Applied Meteorology, 44, 1896-1911, doi: 10.1175/jam2309.1, 2005b.

Baum, B. A., Yang, P., Heymsfield, A. J., Schmitt, C. G., Xie, Y., Bansemer, A., Hu, Y.-X., and Zhang, Z.: Improvements in shortwave bulk scattering and absorption models for the remote sensing of ice clouds, Journal of Applied Meteorology and Climatology, 50, 1037-1056, doi: 10.1175/2010jamc2608.1, 2010.

Baumgardner, D., Jonsson, H., Dawson, W., O'Connor, D., and Newton, R.: The cloud, aerosol and precipitation spectrometer: A new instrument for cloud investigations, Atmospheric Research, 59–60, 251-264, doi: 10.1016/s0169-8095(01)00119-3, 2001.

Baumgardner, D., Brenguier, J. L., Bucholtz, A., Coe, H., DeMott, P., Garrett, T. J., Gayet, J. F., Hermann, M., Heymsfield, A., Korolev, A., Krämer, M., Petzold, A., Strapp, W., Pilewskie, P., Taylor, J., Twohy, C., Wendisch, M., Bachalo, W., and Chuang, P.: Airborne instruments to measure atmospheric aerosol particles, clouds and radiation: A cook's tour of mature and emerging technology, Atmospheric Research, 102, 10-29, doi: 10.1016/j.atmosres.2011.06.021, 2011.

Bi, L., Yang, P., Kattawar, G. W., and Kahn, R.: Single-scattering properties of triaxial ellipsoidal particles for a size parameter range from the Rayleigh to geometric-optics regimes, Applied Optics, 48, 114-126, 2009.

Bohren, C. F., and Singham, S. B.: Backscattering by nonspherical particles: A review of methods and suggested new approaches, Journal of Geophysical Research: Atmospheres, 96, 5269-5277, doi: 10.1029/90jd01138, 1991.

Bohren, C. F., and Huffman, D. R.: Absorption and scattering of light by small particles, Wiley-VCH Verlag GmgH, Weinheim, Germany, 2004.

Brooks, S. D., Toon, O. B., Tolbert, M. A., Baumgardner, D., Gandrud, B. W., Browell, E. V., Flentje, H., and Wilson, J. C.: Polar stratospheric clouds during SOLVE/THESEO: Comparison of lidar observations with in situ measurements, Journal of Geophysical Research: Atmospheres, 109, D02212, doi: 10.1029/2003jd003463, 2004.

Bullard, J. E., and White, K.: Quantifying iron oxide coatings on dune sands using spectrometric measurements: An example from the Simpson-Strzelecki Desert, Australia, Journal of Geophysical Research: Atmospheres, 107, 2125, doi: 10.1029/2001jb000454, 2002.

Caquineau, S., Gaudichet, A., Gomes, L., and Legrand, M.: Mineralogy of Saharan dust transported over northwestern tropical Atlantic Ocean in relation to source regions, Journal of Geophysical Research: Atmospheres, 107, 4251, doi: 10.1029/2000jd000247, 2002.

Carlson, T. N., and Benjamin, S. G.: Radiative heating rates for Saharan Dust, Journal of the Atmospheric Sciences, 37, 193-213, doi: 10.1175/1520-0469(1980)037<0193:rhrfsd>2.0.co;2, 1980.

Chen, Y., Kreidenweis, S. M., McInnes, L. M., Rogers, D. C., and DeMott, P. J.: Single particle analyses of ice nucleating aerosols in the upper troposphere and lower stratosphere, Geophysical Research Letters, 25, 1391-1394, doi: 10.1029/97gl03261, 1998.

Cho, H.-M., Yang, P., Kattawar, G. W., Nasiri, S. L., Hu, Y., Minnis, P., Trepte, C., and Winker, D.: Depolarization ratio and attenuated backscatter for nine cloud types: Analyses based on collocated CALIPSO lidar and MODIS measurements, Optics Express, 16, 3931-3948, 2008.

Clavano, W., Boss, E., and Karp-Boss, L.: Inherent optical properties of non-spherical marine-like particles from theory to observation, Oceanography and Marine Biology: An Annual Review, 45, 1-38, 2007.

Creamean, J. M., Suski, K. J., Rosenfeld, D., Cazorla, A., DeMott, P. J., Sullivan, R. C., White, A. B., Ralph, F. M., Minnis, P., Comstock, J. M., Tomlinson, J. M., and Prather, K. A.: Dust and biological aerosols from the Sahara and Asia influence precipitation in the Western U.S, Science, 339, 1572-1578, doi: 10.1126/science.1227279, 2013.

Curtis, D. B., Aycibin, M., Young, M. A., Grassian, V. H., and Kleiber, P. D.: Simultaneous measurement of light-scattering properties and particle size

distribution for aerosols: Application to ammonium sulfate and quartz aerosol particles, Atmospheric Environment, 41, 4748-4758, doi: 10.1016/j.atmosenv.2007.03.020, 2007.

Curtis, D. B., Meland, B., Aycibin, M., Arnold, N. P., Grassian, V. H., Young, M. A., and Kleiber, P. D.: A laboratory investigation of light scattering from representative components of mineral dust aerosol at a wavelength of 550 nm, Journal Geophysical Research, 113, D08210, doi: 10.1029/2007jd009387, 2008.

Cziczo, D. J., DeMott, P. J., Brock, C., Hudson, P. K., Jesse, B., Kreidenweis, S. M., Prenni, A. J., Schreiner, J., Thomson, D. S., and Murphy, D. M.: A method for single particle mass spectrometry of ice nuclei, Aerosol Science and Technology, 37, 460-470, doi: 10.1080/02786820300976, 2013.

DeMott, P. J., Möhler, O., Stetzer, O., Vali, G., Levin, Z., Petters, M. D., Murakami, M., Leisner, T., Bundke, U., Klein, H., Kanji, Z. A., Cotton, R., Jones, H., Benz, S., Brinkmann, M., Rzesanke, D., Saathoff, H., Nicolet, M., Saito, A., Nillius, B., Bingemer, H., Abbatt, J., Ardon, K., Ganor, E., Georgakopoulos, D. G., and Saunders, C.: Resurgence in ice nuclei measurement research, Bulletin of the American Meteorological Society, 92, 1623-1635, doi: 10.1175/2011bams3119.1, 2011.

Dessler, A. E., and Yang, P.: The distribution of tropical thin cirrus clouds inferred from terra MODIS data, Journal of Climate, 16, 1241-1247, doi: 10.1175/1520-0442(2003)16<1241:tdottc>2.0.co;2, 2003.

DMT: The Cloud Aerosol Spectrometer - Depolarization Option operator manual, DOC-0167 Revision C, 2011.

Duce, R. A., and Tindale, N. W.: Atmospheric transport of iron and its deposition in the ocean, Limnology and Oceanography, 36, 1715–1726, 1991.

Ellis, E. A., and Pendleton, M. W.: Vapor coating: A simple, economical procedure for preparing difficult specimens for scanning electron microscopy, Microscopy Today, 15, 1, 2007.

Glen, A., and Brooks, S.: A new method for measuring optical scattering properties of atmospherically relevant dusts using the Cloud and Aerosol Spectrometer with Polarization (CASPOL), Atmospheric Chemistry and Physics, 13, 1345-1356, doi:10.5194/acp-13-1345-2013, 2013.

Goudie, A. S., and Middleton, N. J.: Saharan dust storms: nature and consequences, Earth-Science Reviews, 56, 179-204, doi: 10.1016/s0012-8252(01)00067-8, 2001.

Gringel, W., and Muhleisen, R.: Sahara dust concentration in the troposphere over the north Atlantic derived from measurements of air conductivity, Beiträge zur Atmosphärenphysik, 51, 121-128, 1977.

Harris-Hobbs, R. L., and Cooper, W. A.: Field evidence supporting quantitative predictions of secondary ice production rates, Journal of the Atmospheric Sciences, 44, 1071-1082, doi: 10.1175/1520-0469(1987)044<1071:fesqpo>2.0.co;2, 1987.

Heymsfield, A. J., and Iaquinta, J.: Cirrus crystal terminal velocities, Journal of the Atmospheric Sciences, 57, 916-938, doi: 10.1175/1520-0469(2000)057<0916:cctv>2.0.co;2, 2000.

Hinds, W. C.: Aerosol technology: Properties, behavior, and measurement of airborne particles, Second Edition., Wiley, New York, 1999.

Hiranuma, N., Brooks, S. D., Moffet, R. C., Glen, A., Laskin, A., Gilles, M. K., Liu, P., Macdonald, A. M., Strapp, J. W., and McFarquhar, G. M.: Chemical characterization of individual particles and residuals of cloud droplets and ice crystals collected onboard research aircraft in the ISDAC 2008 study, Journal of Geophysical Research: Atmospheres, doi: 10.1002/jgrd.50484, 2013.

Hu, Y., Vaughan, M., Liu, Z., Lin, B., Yang, P., Flittner, D., Hunt, B., Kuehn, R., Huang, J., Wu, D., Rodier, S., Powell, K., Trepte, C., and Winker, D.: The depolarization - attenuated backscatter relation: CALIPSO lidar measurements vs. theory, Optics Express, 15, 5327-5332, 2007.

IPCC: Climate Change 2007: The physical science basis. Contribution of working group I to the fourth assessment report of the intergovernmental panel on climate change, Cambridge, United Kingdom and New York, NY, USA, 996, 2007.

Isono, K.: On ice-crystal nuclei and other substances found in snow crystals, Journal of Meteorology, 12, 456-462, doi: 10.1175/1520-0469(1955)012<0456:oicnao>2.0.co;2, 1955.

Iwasaka, Y., Minoura, H., and Nagaya, K.: The transport and spacial scale of Asian dust-storm clouds: A case study of the dust-storm event of April 1979, Tellus B, 35B, 189-196, doi: 10.1111/j.1600-0889.1983.tb00023.x, 1983.

Kanji, Z. A., and Abbatt, J. P. D.: Ice nucleation onto Arizona test dust at cirrus temperatures: Effect of temperature and aerosol size on onset relative humidity, The Journal of Physical Chemistry A, 114, 935-941, doi: 10.1021/jp908661m, 2009.

Kerker, M., Scheiner, P., Cooke, D. D., and Kratohvil, J. P.: Absorption index and color of colloidal hematite, Journal of Colloid and Interface Science, 71, 176-187, doi: 10.1016/0021-9797(79)90231-5, 1979.

Koehler, K.: The impact of natural dust aerosol on warm and cold cloud formation, PhD, Atmospheric Science, Colorado State University, Fort Collins, CO, 225 pp., 2007.

Koehler, K., Kreidenweis, S., DeMott, P., Petters, M., Prenni, A., and Möhler, O.: Laboratory investigations of the impact of mineral dust aerosol on cold cloud formation, Atmospheric Chemistry and Physics, 10, 955-911, 2010.

Li, I. L., Fu, L., Li, H., Zhai, J., and Ruan, S.: Refraction indices measurement of hexagonal zeolite crystal using Brewster angle method, Advanced Materials Research 146-147, 3, doi: 10.4028/www.scientific.net/AMR.146-147.429, 2010.

Lin, H., Noone, K. J., Ström, J., and Heymsfield, A. J.: Small ice crystals in cirrus clouds: A model study and comparison with in situ observations, Journal of the Atmospheric Sciences, 55, 1928-1939, doi: 10.1175/1520-0469(1998)055<1928:sicicc>2.0.co;2, 1998.

Liou, K.-N.: Influence of cirrus clouds on weather and climate processes: A global perspective, Monthly Weather Review, 114, 1167-1199, doi: 10.1175/1520-0493(1986)114<1167:ioccow>2.0.co;2, 1986.

Liu, B. Y. H., Berglund, R. N., and Agarwal, J. K.: Experimental studies of optical particle counters, Atmospheric Environment 8, 717-732, doi: 10.1016/0004-6981(74)90163-2, 1974.

Liu, Z., Liu, D., Huang, J., Vaughan, M., Uno, I., Sugimoto, N., Kittaka, C., Trepte, C., Wang, Z., Hostetler, C., and Winker, D.: Airborne dust distributions over the Tibetan Plateau and surrounding areas derived from the first year of CALIPSO lidar observations, Atmospheric Chemistry and Physics, 8, 5045-5060, doi: 10.5194/acp-8-5045-2008, 2008.

McFarquhar, G. M., Zhang, G., Poellot, M. R., Kok, G. L., McCoy, R., Tooman, T., Fridlind, A., and Heymsfield, A. J.: Ice properties of single-layer stratocumulus during the Mixed-Phase Arctic Cloud Experiment: 1. Observations, Journal of Geophysical Research: Atmospheres, 112, D24201, doi: 10.1029/2007jd008633, 2007.

McFarquhar, G. M., Ghan, S., Verlinde, J., Korolev, A., Strapp, J. W., Schmid, B., Tomlinson, J. M., Wolde, M., Brooks, S. D., Cziczo, D., Dubey, M. K., Fan, J., Flynn, C., Gultepe, I., Hubbe, J., Gilles, M. K., Laskin, A., Lawson, P., Leaitch, W. R., Liu, P., Liu, X., Lubin, D., Mazzoleni, C., Macdonald, A.-M., Moffet, R. C., Morrison, H., Ovchinnikov, M., Shupe, M. D., Turner, D. D., Xie, S., Zelenyuk, A., Bae, K., Freer, M., and Glen, A.: Indirect and semi-direct aerosol campaign, Bulletin of the American Meteorological Society, 92, 183-201, doi: 10.1175/2010bams2935.1, 2011.

Mishchenko, M. I., Travis, L. D., Kahn, R. A., and West, R. A.: Modeling phase functions for dustlike tropospheric aerosols using a shape mixture of randomly oriented polydisperse spheroids, Journal of Geophysical Research: Atmospheres, 102, 16831-16847, doi: 10.1029/96jd02110, 1997.

Mishchenko, M. I.: Electromagnetic scattering by nonspherical particles: A tutorial review, Journal of Quantitative Spectroscopy and Radiative Transfer, 110, 808-832, doi: 10.1016/j.jqsrt.2008.12.005, 2009.

Morgan, W. T., Allan, J. D., Bower, K. N., Esselborn, M., Harris, B., Henzing, J. S., Highwood, E. J., Kiendler-Scharr, A., McMeeking, G. R., Mensah, A. A., Northway, M. J., Osborne, S., Williams, P. I., Krejci, R., and Coe, H.: Enhancement of the aerosol direct radiative effect by semi-volatile aerosol components: Airborne measurements in North-Western Europe, Atmospheric Chemistry and Physics: Discussion, 10, 10653-10705, doi: 10.5194/acpd-10-10653-2010, 2010.

Murray, B., O'Sullivan, D., Atkinson, J., and Webb, M.: Ice nucleation by particles immersed in supercooled cloud droplets, Chemical Society Reviews, 41, 6519-6554, 2012.

Noone, K. B., Noone, K. J., Heintzenberg, J., Ström, J., and Ogren, J. A.: In situ observations of cirrus cloud microphysical properties using the counterflow virtual impactor, Journal of Atmospheric and Oceanic Technology, 10, 294-303, doi:10.1175/1520-0426(1993)010<0294:ISOOCC>2.0.CO;2, 1993.

Peters, T. M., Riss, A. L., Holm, R. L., Singh, M., and Vanderpool, R. W.: Design and evaluation of an inlet conditioner to dry particles for real-time particle sizers, Journal of Environmental Monitoring, 10, 541-551, 2008.

Prenni, A. J., DeMott, P. J., Kreidenweis, S. M., and Rogers, D. C.: Continuous flow ice thermal diffusion chamber measurements of ice nuclei in the Arctic, Sixteenth ARM Science Team Meeting Proceedings, Albuquerque, NM, 2006.

Prenni, A. J., DeMott, P. J., Twohy, C., Poellot, M. R., Kreidenweis, S. M., Rogers, D. C., Brooks, S. D., Richardson, M. S., and Heymsfield, A. J.: Examinations of ice formation processes in Florida cumuli using ice nuclei measurements of anvil ice crystal particle residues, Journal of Geophysical Research: Atmospheres, 112, D10221, doi: 10.1029/2006jd007549, 2007.

Prodi, F., and Fea, G.: A case of transport and deposition of Saharan dust over the Italian Peninsula and Southern Europe, Journal of Geophysical Research: Atmospheres, 84, 6951-6960, doi: 10.1029/JC084iC11p06951, 1979.

Prospero, J. M., Bonatti, E., Schubert, C., and Carlson, T. N.: Dust in the Caribbean atmosphere traced to an African dust storm, Earth and Planetary Science Letters, 9, 287-293, doi: 10.1016/0012-821x(70)90039-7, 1970.

Prospero, J. M., Olmez, I., and Ames, M.: Al and Fe in PM2.5 and PM10 suspended particles in South Central Florida: The impact of the long range transport of African mineral dust, Journal of Water, Air, and Soil Pollution, 125, 291 - 317, 2001.

Prospero, J. M.: Saharan dust impacts and climate change, Oceanography, 19, 60-61, 2006.

Rogers, D. C.: Development of a continuous flow thermal gradient diffusion chamber for ice nucleation studies, Atmospheric Research, 22, 149-181, 1988.

Rogers, D. C.: Detecting ice nuclei with a continuous flow diffusion chamber - Some exploratory tests of instrument response, Journal of Atmospheric and Oceanic Technology, 11, 1042-1047, doi:10.1175/1520-0426(1994)011<1042:DINWAC>2.0.CO;2, 1994.

Rogers, D. C., DeMott, P. J., Kreidenweis, S. M., and Chen, Y.: Measurements of ice nucleating aerosols during SUCCESS, Geophysical Research Letters, 25, 1383-1386, doi: 10.1029/97gl03478, 1998.

Rogers, D. C., DeMott, P. J., and Kreidenweis, S. M.: Airborne measurements of tropospheric ice-nucleating aerosol particles in the Arctic spring, Journal of Geophysical Research, 106, 15053-15063, doi: 10.1029/2000jd900790, 2001a.

Rogers, D. C., DeMott, P. J., Kreidenweis, S. M., and Chen, Y.: A continuous-flow diffusion chamber for airborne measurements of ice nuclei, Journal of Atmospheric and Oceanic Technology, 18, 725-741, doi: 10.1175/1520-0426(2001)018<0725:ACFDCF>2.0.CO;2, 2001b.

Rosenfeld, D., Yu, X., Liu, G., Xu, X., Zhu, Y., Yue, Z., Dai, J., Dong, Z., Dong, Y., and Peng, Y.: Glaciation temperatures of convective clouds ingesting desert dust, air pollution and smoke from forest fires, Geophysical Research Letters, 38, L21804, doi: 10.1029/2011gl049423, 2011.

Sassen, K.: The polarization lidar technique for cloud research: A review and current assessment, Bulletin of the American Meteorological Society, 72, 1848-1866, doi: 10.1175/1520-0477(1991)072<1848:tpltfc>2.0.co;2, 1991.

Sassen, K.: Indirect climate forcing over the western US from Asian dust storms, Geophysical Research Letters, 29, 1465, doi: 10.1029/2001gl014051, 2002.

Ström, J., Heintzenberg, J., Noone, K. J., Noone, K. B., Ogren, J. A., Albers, F., and Quante, M.: Small crystals in cirriform clouds: A case study of residue size distribution, cloud water content and related cloud properties, Atmospheric Research, 32, 125-141, http://dx.doi.org/10.1016/0169-8095(94)90056-6, 1994.

Sugimoto, N., Matsui, I., Shimizu, A., Uno, I., Asai, K., Endoh, T., and Nakajima, T.: Observation of dust and anthropogenic aerosol plumes in the Northwest Pacific with a two-wavelength polarization lidar on board the research vessel Mirai, Geophysical Research Letters, 29, 1901, doi: 10.1029/2002gl015112, 2002.

Toon, O. B., Tabazadeh, A., Browell, E. V., and Jordan, J.: Analysis of lidar observations of Arctic polar stratospheric clouds during January 1989, Journal of Geophysical Research: Atmospheres, 105, 20589-20615, doi: 10.1029/2000jd900144, 2000.

TSI: Model 3450 Vibrating Orifice Aerosol Generator manual, http://www.tsi.com/vibrating-orifice-aerosol-generator-3450/, 2002.

Uematsu, M., Wang, Z., and Uno, I.: Atmospheric input of mineral dust to the western North Pacific region based on direct measurements and a regional chemical transport model, Geophysical Research. Letters, 30, 1342, doi: 10.1029/2002gl016645, 2003.

Vali, G.: Ice Nucleation - Theory, NCAR/ASP 1999 Summer Colloquium, Boulder, Colorado, June 25, 1999.

Verlinde, J., Harrington, J. Y., Yannuzzi, V. T., Avramov, A., Greenberg, S., Richardson, S. J., Bahrmann, C. P., McFarquhar, G. M., Zhang, G., Johnson, N., Poellot, M. R., Mather, J. H., Turner, D. D., Eloranta, E. W., Tobin, D. C., Holz, R., Zak, B. D., Ivey, M. D., Prenni, A. J., DeMott, P. J., Daniel, J. S., Kok, G. L., Sassen, K., Spangenberg, D., Minnis, P., Tooman, T. P., Shupe, M., Heymsfield, A. J., and Schofield, R.: The mixed-phase Arctic cloud experiment, Bulletin of the American Meteorological Society, 88, 205-221, doi:10.1175/BAMS-88-2-205, 2007.

Weinzierl, B., Petzold, A., Esselborn, M., Wirth, M., Rasp, K., Kandler, K., SchÜTz, L., Koepke, P., and Fiebig, M.: Airborne measurements of dust layer properties, particle size distribution and mixing state of Saharan dust during SAMUM 2006, Tellus B, 61, 96-117, doi: 10.1111/j.1600-0889.2008.00392.x, 2009.

West, R. A., Doose, L. R., Eibl, A. M., Tomasko, M. G., and Mishchenko, M. I.: Laboratory measurements of mineral dust scattering phase function and linear polarization, Journal Geophysical Research, 102, 16871-16881, doi: 10.1029/96jd02584, 1997.

Xu, J., Bergin, M. H., Greenwald, R., Schauer, J. J., Shafer, M. M., Jaffrezo, J. L., and Aymoz, G.: Aerosol chemical, physical, and radiative characteristics near a desert source region of northwest China during ACE-Asia, Journal Geophysical Research, 109, D19S03, doi: 10.1029/2003jd004239, 2004.

Yang, P., and Liou, K.-N.: Light scattering and absorption by nonspherical ice crystals, in Light scattering reviews, edited by: Institute of Environmental Physics, University of Bremen, Springer Berlin Heidelberg, 31-71, 2006.

Yunus, W. M. M., Fen, Y. W., and Yee, L. M.: Refractive index and fourier transform infrared spectra of virgin coconut oil and virgin olive oil, American Journal of Applied Sciences, 6, 328-331, doi: 10.3844/ajassp.2009.328.331, 2009.

Zender, C. S., and Kiehl, J. T.: Radiative sensitivities of tropical anvils to small ice crystals, Journal of Geophysical Research: Atmospheres, 99, 25869-25880, doi: 10.1029/94jd02090, 1994.

# APPENDIX A

Attached below are Appendix files discussed throughout the Thesis.

## CASPOL IDL Analysis - MK II

The following code was developed to generate the backscatter and depolarization ratio plots as a function of particle size as seen in Figure 42. Acknowledgement must be given for use of this code.

```
PRO CASPOL_Lab_MK_II
;The following code is used to complete the basic analysis for the
;CASPOL MK II lab experiments. where
;the x ordinate is the diameter and the y axis will be backscatter
;intensity and depolarization ratio.
;Text data files are created in Part I and read back into the code in
;Part II for analysis.

;Created by Andrew Glen, Texas A&M University
;------------- Analysis Setup ----------------------------------------

drive_loc = 'g:\'

;Options:
part_1 = 'Yes'     ;Run part I analysis, which analyzes each experiment
part_2 = 'Yes'     ;Run part II analysis, which is where all experiment
data is plotted together
composition_select = 'MK II Data'     ;'Proposal 06/11'; All
min_num_particles_cutoff = 'Yes'      ;Uses a minium number of
particles per channel as a cutoff for analysis

;Constants
wavelength = 680. ;nm
CASPOL_Q = 1.2    ;L/min
ratio_y_max = 1
normalization_cnts = 1
min_num_particles = 10
```

```
;-------------------------------------------------------------------
---------------------------------------------------

;Selecting which compositions are to be used in analysis and supporting
changes to file locations
IF composition_select eq 'MK II Data' THEN BEGIN

composition_types = ['Arizona Test Dust', 'Hematite',
'Kaolinite','Gypsum','Quartz','Red N.M.','Red S.A.', $
                     'White Quartz','White Sands','Magnetite',
'Montmorillonite','Yellow S.A.','Zeolite', $
                     'Homo -46C 18%i','Homo -56C 79%i','Homo -55C
39%i',$
                     'Homo -54C 29%i', 'Homo -55C 34%i', 'Homo -55C
41%i','Homo -56C 48%i', 'Hete -55C 55%i ATD','Hete -55C 85%i ATD',$
                     'Hete -55C 50%i Zeo','Hete -55C 50%i Hema2']

  number_of_files = SIZE(composition_types, /N_ELEMENTS)
  txt_output_file_path = drive_loc+'Arranged Files\Work -
Texas\Research\CASPOL\Data MK II\Compiled Data\'
ENDIF


;-------------------------------------------------------------------
---------------------------------------------------
;-------------------------------------------------------------------
---------------------------------------------------
;Part I - Opening each raw data file and creating Figures for each one
and outputting an average of all important
;data in a .txt file for use in part II.


IF part_1 eq 'Yes' THEN BEGIN

;Creating Text File templates for use later. See
output_ratios_vs_size_data.pro
CLOSE, 34
OPENW, 34, txt_output_file_path+'Output List - PBP Size Data.txt'
CLOSE, 34
;-------------------------------------------------------------------
--------

;Opening all RAW data files from the CASPOL and begins the single
experiment data reduction and analysis
;also creates the individual figures for each experiment and the .txt
file of average values of data.

FOR data_num = 0, number_of_files-1 DO BEGIN

IF composition_select eq 'MK II Data' THEN BEGIN

data_list_MK_II_Data, data_num, drive_loc, main_file_name,
pbp_file_name,$      ;Opens list containing the
```

```
           file_path, composition, aero_size, hh_start, mm_start,
hh_finish,$   ;data files and oeprational
           mm_finish, sample_status, file_time_s
;conditions.

PRINT, 'Data Selected = '+composition


PRINT, STRING(data_num)+' out of '+STRTRIM(STRING(number_of_files-1),2)


CASPOL_pbp_csv_file_reader_MK_II, file_path, pbp_file_name, time,
fwd_size,$     ;Opening the .csv file for the
                           bck_size, depol_size, IPT, n, diameter, $
;CASPOL pbp data
                           fwd_thresholds, bck_diameter,
bck_thresholds

FOR o = 0L, SIZE(bck_size,/N_ELEMENTS)-1 DO BEGIN
bck_size(o) = bck_size(o)+depol_size(o)
ENDFOR
;size_parameter_calc, diameter, thresholds, wavelength,
size_parameter,$           ;Calculating Size Parameter and
;                     file_path, pbp_file_name
;output a .txt file for each exp.

n_particles = SIZE(fwd_size, /n_elements)
;Print the total number of particles in
PRINT, 'Number of Particles', n_particles
;the steady state interval.


avg_fwd_size = FLTARR(30)
avg_bck_size = FLTARR(30)
avg_depol_size = FLTARR(30)
particles_per_ch = FLTARR(30)
stdev_fwd = DBLARR(30)
stdev_bck = DBLARR(30)
stdev_depol = DBLARR(30)
stdev_bck_fwd = DBLARR(30)
stdev_depol_fwd = DBLARR(30)
stdev_depol_bck = DBLARR(30)

FOR i =0, 28 DO BEGIN
test = WHERE(fwd_size(*) ge fwd_thresholds(i) AND fwd_size(*) lt
fwd_thresholds(i+1) AND bck_size(*) ne 0.)
  IF test(0) ne -1 AND SIZE(test, /N_ELEMENTS) ge 3 THEN BEGIN
    avg_fwd_size(i) = MEAN(fwd_size(test))/normalization_cnts
    avg_bck_size(i) = MEAN(bck_size(test))/normalization_cnts
    avg_depol_size(i) = MEAN(depol_size(test))/normalization_cnts
    particles_per_ch(i) = SIZE(test, /N_ELEMENTS)
    stdev_fwd(i) = STDDEV(fwd_size(test))
    stdev_bck(i) = STDDEV(bck_size(test))
```

```
    stdev_depol(i) = STDDEV(depol_size(test))
    stdev_bck_fwd(i) = STDEV(bck_size(test)/fwd_size(test))
    stdev_depol_fwd(i) = STDEV(depol_size(test)/fwd_size(test))
    stdev_depol_bck(i) = STDEV(depol_size(test)/bck_size(test))
  ENDIF
ENDFOR

size_parameter = FLTARR(30)
output_ratios_vs_size_MK_II_data, diameter, size_parameter,
avg_fwd_size, avg_bck_size, avg_depol_size,$
                                txt_output_file_path, pbp_file_name,
composition, aero_size, sample_status,$
                                particles_per_ch, stdev_fwd, stdev_bck,
stdev_depol, stdev_bck_fwd,$
                                stdev_depol_fwd, stdev_depol_bck,
composition_select

output_size_distributions_MK_II_data, diameter, fwd_size,
fwd_thresholds, bck_size, CASPOL_Q, file_time_s,$
                               txt_output_file_path, composition,
n_particles


output_name = STRTRIM(composition, 2)+' - Size vs Ratio.ps'
SET_PLOT, 'PS'
DEVICE, filename = file_path+output_name, /color,  $
                          /TT_FONT, xsize = 8.5, ysize =10, /inches,
yoffset = 0, xoffset = 0
LOADCT, 39
;!Y.RANGE = [1e-4,100]
!X.STYLE = 1
!Y.STYLE = 1
!P.THICK = 4
!X.THICK = 4
!Y.THICK = 4
!P.CHARTHICK = 5
!P.CHARSIZE = 1.1
!P.FONT = 6

plotting_ratios_vs_size_MK_II_data, fwd_size, bck_size, depol_size,
fwd_thresholds, diameter,$
                               size_parameter, main_file_name,
pbp_file_name,$
                               composition, aero_size, output_name,
txt_output_file_path, ratio_y_max,$
                               normalization_cnts, sample_status,
n_particles, composition_select

;Testing area:
;Test back thresholds and what they relate too.


    avg_fwd_size_from_bck = FLTARR(30)
```

```
    avg_bck_size_from_bck = FLTARR(30)
    avg_depol_size_from_bck = FLTARR(30)

FOR i =0, 28 DO BEGIN
test_bck = WHERE(bck_size(*) ge bck_thresholds(i) AND bck_size(*) lt
bck_thresholds(i+1))
  IF test_bck(0) ne -1 AND SIZE(test_bck, /N_ELEMENTS) ge 3 THEN BEGIN
    avg_fwd_size_from_bck(i) =
MEAN(fwd_size(test_bck))/normalization_cnts
    avg_bck_size_from_bck(i) =
MEAN(bck_size(test_bck))/normalization_cnts
    avg_depol_size_from_bck(i) =
MEAN(depol_size(test_bck))/normalization_cnts
  ENDIF
ENDFOR


PLOT, fwd_size, bck_size, psym = 3, position = [0.15,0.5,0.8,0.9],
xtitle = 'Fwd Digital', ytitle = 'Bck Digital'
OPLOT, avg_fwd_size, avg_bck_size, psym = 2, color =250

PLOT, fwd_thresholds, bck_thresholds, psym = 4, position =
[0.15,0.5,0.8,0.9], xtitle = 'fwd threshold channel',$
                            ytitle = 'bck_threshold channel'
PLOT, diameter, fwd_thresholds, psym = 4, position =
[0.15,0.15,0.8,0.45],/noerase, xtitle = 'Diameter (!9m!Xm)',$
                             ytitle = 'Digital Count'
OPLOT, bck_diameter, bck_thresholds, psym = 4, color = 250

PLOT, bck_diameter, avg_fwd_size_from_bck, psym =2, /xlog, position =
[0.15, 0.7,0.9, 0.95],$
                                                ytitle = 'Forward
Scatter Counts', yrange = [0, 9000]



PLOT, bck_diameter, avg_bck_size_from_bck, psym =2, /xlog, position =
[0.15, 0.45,0.9, 0.7], /noerase,$
                                                ytitle = 'Back Scatter
Counts';, yrange = [0, 500]


PLOT, bck_diameter, avg_depol_size_from_bck, psym =2, /xlog, position =
[0.15, 0.2,0.9, 0.45], /noerase,$
                                                xtitle = 'Back Diameter
(!9m!Xm)', ytitle = 'Depolarization Counts';,$
                                               ; yrange = [0, 20]

DEVICE, /close

ENDIF

ENDFOR
```

```
PRINT, 'End of Part I'
ENDIF



;---------------------------------------------------------------------------
-----------------------------------------
;***************************************************************************
************************************
;---------------------------------------------------------------------------
-----------------------------------------
;Part II - Creating Figures for all the data collected and listed in
the file: Output List - PBP Size Data.txt
IF part_2 eq 'Yes' THEN BEGIN    ;1

IF composition_select eq 'MK II Data' THEN BEGIN
  data_list_file_path = txt_output_file_path
  data_list_file_name = 'Output List - PBP Size Data.txt'
  part_2_data_list_reader, data_list_file_path, data_list_file_name,
p2_filename, composition, aero_size, n_files,$
                                          sample_status


  diameter_array = FLTARR(n_files, 30)
  size_parameter_array = FLTARR(n_files, 30)
  avg_fwd_cnts_array = FLTARR(n_files, 30)
  avg_bck_cnts_array = FLTARR(n_files, 30)
  avg_depol_cnts_array = FLTARR(n_files, 30)
  color_comp = FLTARR(n_files)
  line_sample_status = FLTARR(n_files)
  stdev_fwd_array = FLTARR(n_files, 30)
  stdev_bck_array = FLTARR(n_files, 30)
  stdev_depol_array = FLTARR(n_files, 30)
  stdev_bck_fwd_array = FLTARR(n_files, 30)
  stdev_depol_fwd_array = FLTARR(n_files, 30)
  stdev_depol_bck_array = FLTARR(n_files, 30)
  num_particles_array = FLTARR(n_files, 30)
        color_comp = FLTARR(n_files)
        symbol = FLTARR(n_files)
        optical_group = FLTARR(n_files)
  FOR i = 0, n_files-1 DO BEGIN
    part_2_CASPOL_avg_pbp_size_file_reader, data_list_file_path,
p2_filename(i), channel, diameter, size_parameter,$
                              avg_fwd_cnts, avg_bck_cnts, avg_depol_cnts,
n, stdev_fwd, stdev_bck, stdev_depol,$
                              stdev_bck_fwd, stdev_depol_fwd,
stdev_depol_bck, num_particles

    FOR j = 0, 28 DO BEGIN
      diameter_array(i,j) = diameter(j)
      size_parameter_array(i,j) = size_parameter(j)
      avg_fwd_cnts_array(i,j) = avg_fwd_cnts(j)
```

```
      avg_bck_cnts_array(i,j) = avg_bck_cnts(j)
      avg_depol_cnts_array(i,j) = avg_depol_cnts(j)
      stdev_fwd_array(i,j) = stdev_fwd(j)
      stdev_bck_array(i,j) = stdev_bck(j)
      stdev_depol_array(i,j) = stdev_depol(j)
      stdev_bck_fwd_array(i,j) = stdev_bck_fwd(j)
      stdev_depol_fwd_array(i,j) = stdev_depol_fwd(j)
      stdev_depol_bck_array(i,j) = stdev_depol_bck(j)
      num_particles_array(i,j) = num_particles(j)

    ENDFOR

;Getting Rid of data with less than minimum number of particles:
;Use this value min_num_particles

    IF min_num_particles_cutoff eq 'Yes' THEN BEGIN
      FOR j = 0, 28 DO BEGIN
        IF num_particles_array(i,j) lt min_num_particles THEN BEGIN
          avg_fwd_cnts_array(i,j) = 0.0
          avg_bck_cnts_array(i,j) = 0.0
          avg_depol_cnts_array(i,j) = 0.0
          stdev_fwd_array(i,j) = 0.0
          stdev_bck_array(i,j) = 0.0
          stdev_depol_array(i,j) = 0.0
          stdev_bck_fwd_array(i,j) = 0.0
          stdev_depol_fwd_array(i,j) = 0.0
          stdev_depol_bck_array(i,j) = 0.0
        ENDIF

        IF avg_fwd_cnts_array(i,j) eq 0.0 THEN BEGIN
          avg_fwd_cnts_array(i,j) = !VALUES.F_NAN
          avg_bck_cnts_array(i,j) = !VALUES.F_NAN
          avg_depol_cnts_array(i,j) = !VALUES.F_NAN
          stdev_fwd_array(i,j) = !VALUES.F_NAN
          stdev_bck_array(i,j) = !VALUES.F_NAN
          stdev_depol_array(i,j) = !VALUES.F_NAN
          stdev_bck_fwd_array(i,j) = !VALUES.F_NAN
          stdev_depol_fwd_array(i,j) = !VALUES.F_NAN
          stdev_depol_bck_array(i,j) = !VALUES.F_NAN
        ENDIF
      ENDFOR
    ENDIF


; Make a vector of 16 points, A[i] = 2pi/16:
A = FINDGEN(17) * (!PI*2/16.)
; Define the symbol to be a unit circle with 16 points,
; and set the filled flag:
USERSYM, COS(A), SIN(A), /FILL

col_1 = 1
col_2 = 60
col_3 = 250
```

```
col_4 = 150
col_5 = 100
col_6 = 200
col_7 = 1

IF composition(i) eq composition_types(0) THEN optical_group(i) = 4;1
IF composition(i) eq composition_types(1) THEN optical_group(i) = 1;20
IF composition(i) eq composition_types(2) THEN optical_group(i) = 1;40
IF composition(i) eq composition_types(3) THEN optical_group(i) = 2;60
IF composition(i) eq composition_types(4) THEN optical_group(i) = 2;80
IF composition(i) eq composition_types(5) THEN optical_group(i) = 2;100
IF composition(i) eq composition_types(6) THEN optical_group(i) = 2;120
IF composition(i) eq composition_types(7) THEN optical_group(i) = 2;140
IF composition(i) eq composition_types(8) THEN optical_group(i) = 2;160
IF composition(i) eq composition_types(9) THEN optical_group(i) = 3;180
IF composition(i) eq composition_types(10) THEN optical_group(i) =
3;200
IF composition(i) eq composition_types(11) THEN optical_group(i) =
3;220
IF composition(i) eq composition_types(12) THEN optical_group(i) =
3;240

IF composition(i) eq composition_types(13) THEN optical_group(i) =
5;240
IF composition(i) eq composition_types(14) THEN optical_group(i) =
5;240
IF composition(i) eq composition_types(15) THEN optical_group(i) =
5;240
IF composition(i) eq composition_types(16) THEN optical_group(i) =
6;240
IF composition(i) eq composition_types(17) THEN optical_group(i) =
6;240
IF composition(i) eq composition_types(18) THEN optical_group(i) =
6;240
IF composition(i) eq composition_types(19) THEN optical_group(i) =
6;240

IF composition(i) eq composition_types(20) THEN optical_group(i) =
7;240
IF composition(i) eq composition_types(21) THEN optical_group(i) =
7;240
IF composition(i) eq composition_types(22) THEN optical_group(i) =
7;240
IF composition(i) eq composition_types(23) THEN optical_group(i) =
7;240

PRINT, optical_group(i)
IF composition(i) eq composition_types(0) THEN symbol(i) = 8;1
IF composition(i) eq composition_types(1) THEN symbol(i) = 1;20
IF composition(i) eq composition_types(2) THEN symbol(i) = 4;40
IF composition(i) eq composition_types(3) THEN symbol(i) = 1;60
IF composition(i) eq composition_types(4) THEN symbol(i) = 4;80
IF composition(i) eq composition_types(5) THEN symbol(i) = 5;100
```

```
IF composition(i) eq composition_types(6) THEN symbol(i) = 6;120
IF composition(i) eq composition_types(7) THEN symbol(i) = 7;140
IF composition(i) eq composition_types(8) THEN symbol(i) = 8;160
IF composition(i) eq composition_types(9) THEN symbol(i) = 1;180
IF composition(i) eq composition_types(10) THEN symbol(i) = 4;200
IF composition(i) eq composition_types(11) THEN symbol(i) = 5;220
IF composition(i) eq composition_types(12) THEN symbol(i) = 6;240
IF composition(i) eq composition_types(13) THEN symbol(i) = 1;240
IF composition(i) eq composition_types(14) THEN symbol(i) = 4;240
IF composition(i) eq composition_types(15) THEN symbol(i) = 5;240

IF composition(i) eq composition_types(16) THEN symbol(i) = 1;240
IF composition(i) eq composition_types(17) THEN symbol(i) = 4;240
IF composition(i) eq composition_types(18) THEN symbol(i) = 5;240
IF composition(i) eq composition_types(19) THEN symbol(i) = 6;240

IF composition(i) eq composition_types(20) THEN symbol(i) = 8;240
IF composition(i) eq composition_types(21) THEN symbol(i) = 8;240
IF composition(i) eq composition_types(22) THEN symbol(i) = 6;240
IF composition(i) eq composition_types(23) THEN symbol(i) = 1;240



IF optical_group(i) eq 1 THEN color_comp(i) = col_1
IF optical_group(i) eq 2 THEN color_comp(i) = col_2
IF optical_group(i) eq 3 THEN color_comp(i) = col_3
IF optical_group(i) eq 4 THEN color_comp(i) = col_4
IF optical_group(i) eq 5 THEN color_comp(i) = col_5
IF optical_group(i) eq 6 THEN color_comp(i) = col_6
IF optical_group(i) eq 7 THEN color_comp(i) = col_7


ENDFOR

part_2_plotting_each_composition, composition, diameter_array,
size_parameter_array,$
                      avg_fwd_cnts_array, avg_bck_cnts_array,
avg_depol_cnts_array,$
                      color_comp, composition_types,
txt_output_file_path, ratio_y_max,$
                      line_sample_status, stdev_fwd_array,
stdev_bck_array, stdev_depol_array,$
                      stdev_bck_fwd_array, stdev_depol_fwd_array,
stdev_depol_bck_array,$
                      composition_select



laser_power = 24.1 ;mW
beam_width = 2.E-3 ; m
laser_intensity = laser_power/(!pi*((beam_width/2.)^2.))
r = 1.E-2    ; m
```

```
k = 2.*!pi/(0.680*1E-6)

avg_bck_scat_intensity =
laser_intensity*avg_bck_cnts_array/((k^2.)*r^2.)
stdev_bck_scat_intensity =
laser_intensity*stdev_bck_array/((k^2.)*r^2.)


part_2_plotting_size_vs_counts_MK_II, txt_output_file_path,
diameter_array, avg_fwd_cnts_array,$
                avg_bck_cnts_array, avg_depol_cnts_array, color_comp,
n_files, p2_filename,$
                composition, size_parameter_array, composition_types,
ratio_y_max,$
                stdev_fwd_array, stdev_bck_array, stdev_depol_array,$
                stdev_bck_fwd_array, stdev_depol_fwd_array,
stdev_depol_bck_array, composition_select,$
                symbol, col_1, col_2, col_3, col_4,
avg_bck_scat_intensity, stdev_bck_scat_intensity



DEVICE,/close

PRINT, 'MK II Data Complete'
ENDIF

ENDIF

END
```

CASPOL Signature Analysis - MK II

The following code was developed to generate the mapped data for scattering signature seen in Figure 44. Acknowledgement must be given for use of this code.

```
PRO d_b_vs_b_map_data_MK_II
;The following code is used to calculate the signatures for MK II
;Dusts and Ice. Step 1) is to read in the data and create a map where
;the x ordinate is the depolarization ratio and the y axis is the total
;backscatter intensity. Step 2 is then to plot this map to produce a
;scattering signature.

;Created by Andrew Glen, Texas A&M University
;------------- Analysis Setup ----------------------------------------
```

```
  drive_loc = 'g:\'
  main_file_name = ' ';'00CAS_POL_PBP20110210145644.csv'
  graph_type = 'd-b vs b'


  working_loc = 'Work\PhD - TX\Research\CASPOL MK II\Data MK
II\Compiled Data\Scatter Plots\'
  output_path = drive_loc+working_loc+graph_type+' Data\'
  file_name = ['White Sands MK II.csv','Gypsum MK II.csv','Arizona Test
Dust MK II.csv','Kaolinite MK II.csv',$
               'Montmorillonite MK II.csv','Quartz MK
II.csv','Magnetite MK II.csv','Red SA MK II.csv',$
               'Yellow SA MK II.csv','Zeolite MK II.csv','White Quartz
MK II.csv','Hematite MK II.csv',$
               'Red NM MK II.csv']

  file_path = drive_loc+working_loc

  output_path = drive_loc+working_loc+graph_type+' Data\'


x_title = 'Total Backscatter Intensity'
y_title = 'Depolarization Ratio'


x_bins = 100.
x_bins_divide = 100.
y_bins = 100.
y_bins_multi = 10.

FOR num_files = 0, SIZE(file_name, /N_ELEMENTS)-1 DO BEGIN

pbp_file_name = file_name(num_files)
;file_path = drive_loc+working_loc+sub_dir(num_files)

PRINT, num_files,' Working File: ',pbp_file_name

CASPOL_pbp_csv_file_reader_MK_II, file_path, pbp_file_name, time,
fwd_size, bck_size,$
                            depol_size, IPT, n, diameter,
fwd_thresholds, bck_diameter,$
                            bck_thresholds
n_particles = size(fwd_size, /n_elements)                        ;Print
the total number of particles in
PRINT, 'Number of Particles', n_particles
;the steady state interval.


bck_total = bck_size + depol_size

bck_fwd_ratio = bck_total/fwd_size          ;Setting up ratios of
detectors.
depol_fwd_ratio = depol_size/fwd_size      ;
```

```
depol_bck_ratio = depol_size/bck_total      ;

FOR i = 0L, n_particles-1 DO BEGIN
IF bck_fwd_ratio(i) eq !VALUES.F_INFINITY THEN bck_fwd_ratio(i) =
!VALUES.F_Nan
IF depol_fwd_ratio(i) eq !VALUES.F_INFINITY THEN depol_fwd_ratio(i) =
!VALUES.F_Nan
IF depol_bck_ratio(i) eq !VALUES.F_INFINITY THEN depol_bck_ratio(i) =
!VALUES.F_Nan
ENDFOR


x_depol_bck = FINDGEN(x_bins)/x_bins_divide
y_bck = FINDGEN(y_bins)*y_bins_multi
z = FLTARR(x_bins,y_bins)

FOR k =0L, n_particles-1 DO BEGIN
  FOR i = 0, x_bins-2 DO BEGIN
    FOR j = 0, y_bins-2 DO BEGIN
      IF depol_bck_ratio(k) ge x_depol_bck(i) AND depol_bck_ratio(k) lt
x_depol_bck(i+1) AND $
         bck_total(k) ge y_bck(j) AND bck_total(k) lt y_bck(j+1) $
         THEN BEGIN z(i,j) = z(i,j)+1
         GOTO, end_loop
      ENDIF
    ENDFOR
  ENDFOR
end_loop:



IF k eq 0 THEN PRINT, '0% Data Ingested'

FOR percent = 1,99 DO BEGIN
IF k ge (n_particles/100.)*percent AND k lt
((n_particles/100.)*percent)+1 THEN PRINT,
STRTRIM(STRING(percent),2)+'% Data Ingested'
ENDFOR
IF k eq n_particles-1 THEN PRINT, '100% Data Ingested'
ENDFOR

PRINT, 'MAX Z', MAX(z(*,*))


;------------- Plotting Data ----------------------------------------
SET_PLOT, 'PS'
DEVICE, filename = output_path+pbp_file_name+' - '+graph_type+'.ps',
/color,  $
                         /TT_FONT, xsize = 8.5, ysize =10, /inches,
yoffset = 0, xoffset = 0
```

```
LOADCT, 39
!X.STYLE = 1
!Y.STYLE = 1
!P.THICK = 5
!X.THICK = 7
!Y.THICK = 7
!P.CHARTHICK = 5
!P.CHARSIZE = 1.1
!P.FONT = 6

PLOT, [0,x_bins/x_bins_divide],[0,y_bins*y_bins_multi], /NODATA,
position = [0.15, 0.4, 0.8, 0.9], xstyle =1, ystyle =1,$
                 xtitle = x_title, ytitle = y_title


; Make a vector of 16 points, A[i] = 2pi/16:
A = FINDGEN(17) * (!PI*2/16.)
; Define the symbol to be a unit circle with 16 points,
; and set the filled flag:
USERSYM, COS(A), SIN(A), /FILL

background_colour = 255
col_step = 0.5
;
  FOR i = 0, x_bins-1 DO BEGIN
;
    FOR j = 0, y_bins-1 DO BEGIN
;

;
      IF (z(i,j) lt col_step) THEN BEGIN
;
        oplot, [i(0)/x_bins_divide],[j(0)*y_bins_multi], psym =8, color
= background_colour, symsize = 0.7      ;
      ENDIF
;

;
      FOR col_index = 1, 250 DO BEGIN
;
        IF (z(i,j) ge col_index*col_step AND z(i,j) lt
(col_index+1)*col_step) THEN BEGIN   ;
          oplot, [i(0)/x_bins_divide],[j(0)*y_bins_multi], psym =8,
color = col_index, symsize = 0.7            ;
        ENDIF
;
      ENDFOR
;

;
     IF (z(i,j) gt 250*col_step) THEN BEGIN
;
```

```
        oplot, [i(0)/x_bins_divide],[j(0)*y_bins_multi], psym =8, color
= 254, symsize = 0.7                    ;
     ENDIF
;
    ENDFOR
;
  ENDFOR
;

DEVICE, /close


;------------- Outputting text file ----------------------------------
FREE_LUN,32
OPENW, 32, output_path+pbp_file_name+' - '+graph_type+'.txt'



FOR j = 0, y_bins-1  DO BEGIN

 PRINTF, 32,
z(0,j),STRING(9b),z(1,j),STRING(9b),z(2,j),STRING(9b),z(3,j),STRING(9b)
,z(4,j),STRING(9b),$

z(5,j),STRING(9b),z(6,j),STRING(9b),z(7,j),STRING(9b),z(8,j),STRING(9b)
,z(9,j),STRING(9b),$

z(10,j),STRING(9b),z(11,j),STRING(9b),z(12,j),STRING(9b),z(13,j),STRING
(9b),z(14,j),STRING(9b),$

z(15,j),STRING(9b),z(16,j),STRING(9b),z(17,j),STRING(9b),z(18,j),STRING
(9b),z(19,j),STRING(9b),$

z(20,j),STRING(9b),z(21,j),STRING(9b),z(22,j),STRING(9b),z(23,j),STRING
(9b),z(24,j),STRING(9b),$

z(25,j),STRING(9b),z(26,j),STRING(9b),z(27,j),STRING(9b),z(28,j),STRING
(9b),z(29,j),STRING(9b),$

z(30,j),STRING(9b),z(31,j),STRING(9b),z(32,j),STRING(9b),z(33,j),STRING
(9b),z(34,j),STRING(9b),$

z(35,j),STRING(9b),z(36,j),STRING(9b),z(37,j),STRING(9b),z(38,j),STRING
(9b),z(39,j),STRING(9b),$

z(40,j),STRING(9b),z(41,j),STRING(9b),z(42,j),STRING(9b),z(43,j),STRING
(9b),z(44,j),STRING(9b),$

z(45,j),STRING(9b),z(46,j),STRING(9b),z(47,j),STRING(9b),z(48,j),STRING
(9b),z(49,j),STRING(9b),$

z(50,j),STRING(9b),z(51,j),STRING(9b),z(52,j),STRING(9b),z(53,j),STRING
(9b),z(54,j),STRING(9b),$
```

```
z(55,j),STRING(9b),z(56,j),STRING(9b),z(57,j),STRING(9b),z(58,j),STRING
(9b),z(59,j),STRING(9b),$

z(60,j),STRING(9b),z(61,j),STRING(9b),z(62,j),STRING(9b),z(63,j),STRING
(9b),z(64,j),STRING(9b),$

z(65,j),STRING(9b),z(66,j),STRING(9b),z(67,j),STRING(9b),z(68,j),STRING
(9b),z(69,j),STRING(9b),$

z(70,j),STRING(9b),z(71,j),STRING(9b),z(72,j),STRING(9b),z(73,j),STRING
(9b),z(74,j),STRING(9b),$

z(75,j),STRING(9b),z(76,j),STRING(9b),z(77,j),STRING(9b),z(78,j),STRING
(9b),z(79,j),STRING(9b),$

z(80,j),STRING(9b),z(81,j),STRING(9b),z(82,j),STRING(9b),z(83,j),STRING
(9b),z(84,j),STRING(9b),$

z(85,j),STRING(9b),z(86,j),STRING(9b),z(87,j),STRING(9b),z(88,j),STRING
(9b),z(89,j),STRING(9b),$

z(90,j),STRING(9b),z(91,j),STRING(9b),z(92,j),STRING(9b),z(93,j),STRING
(9b),z(94,j),STRING(9b),$

z(95,j),STRING(9b),z(96,j),STRING(9b),z(97,j),STRING(9b),z(98,j),STRING
(9b),z(99,j),STRING(9b), format='(100(I9, A1))'

ENDFOR
CLOSE, 32
FREE_LUN,32
ENDFOR
PRINT, 'Code Complete - Good Job'
END
```

# APPENDIX B

## Solidworks Designs for Instrument Upgrades

Several design ideas were drafted during the period of this research for upgrading instrumentation. These ideas were the result of observing short comings in either the experimentation or instruments themselves and do not necessarily represent the absolute solution but instead, represent potential ideas for improvements. These designs are included below as potential ideas for future work:

### CASPOL - CFDC Inlet Plate

Through experiments combining both the CFDC and CASPOL, it is clear to see that the shortest path for ice crystals exiting the CFDC and entering the CASPOL would be preferential not just for improved accuracy but to help keep ice crystals from being fractured or destroyed during their transport to the CASPOL. In addition a shorter travel time at cooled temperatures would help reduce the chance of ice crystal melt. This can be accomplished a number of ways, reduce the mass of the current sliding plate so there is less of a thermal sink (Figure 45) or pump a cooling fluid through the sliding plate (Figure 48 through Figure 51). Figure 45 shows a plate with an 'O' Ring groove on the top protrusion which would seal to the base plate of the current CFDC, allowing enough

space for the bolts which secure the CASPOL to the plate from underneath. In addition there are four holes on the wings to fasten to the current CFDC mounting mechanism.

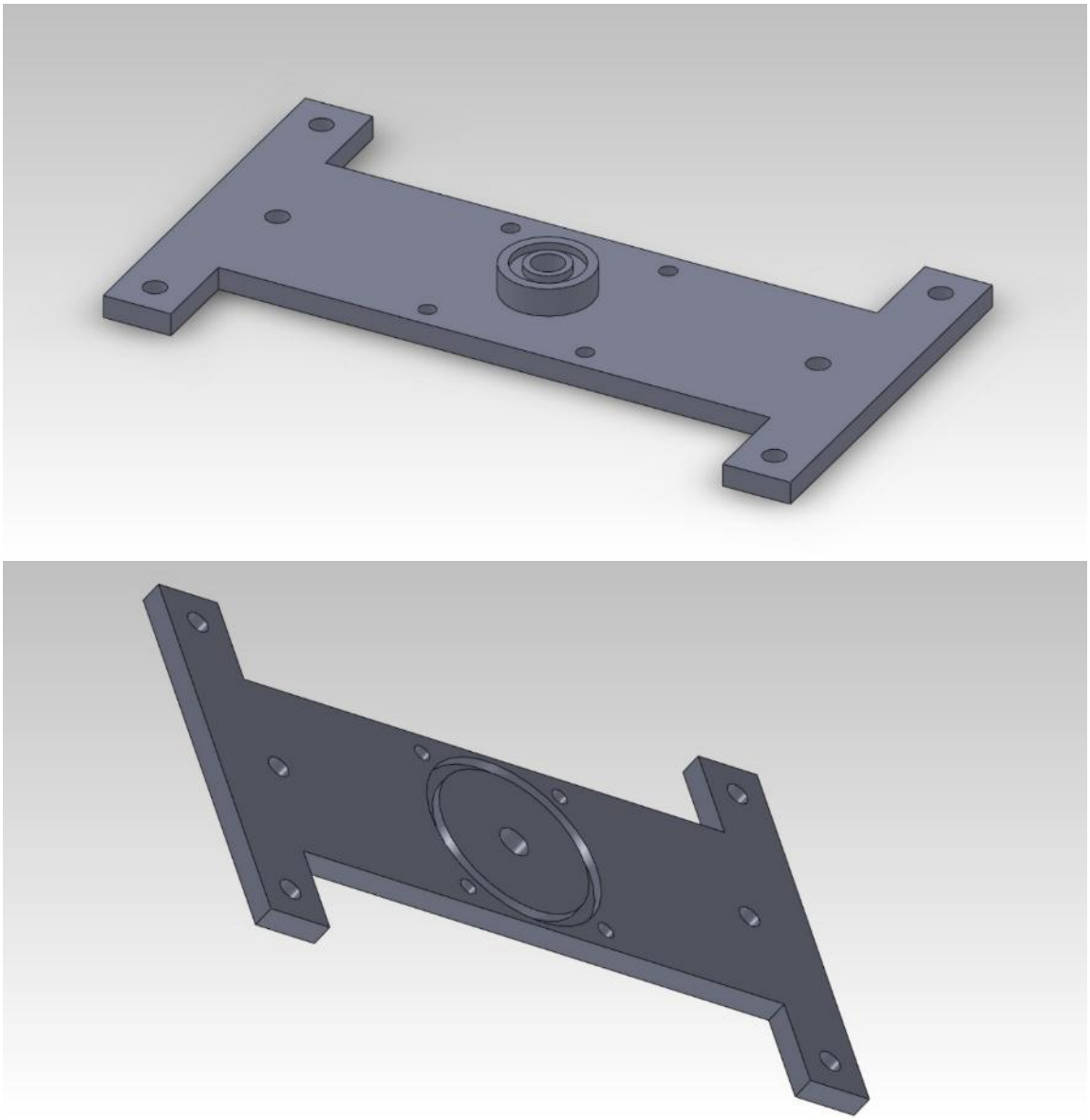

**Figure 45. Modified CFDC sliding plate for connecting to the CASPOL. Reduced thermal mass to reduce particle loss.**

Machining diagrams of this sliding plate option are shown in Figure 46 and Figure 47, they show the dimensions needed to construct this piece including hole cut outs and bolt plates.

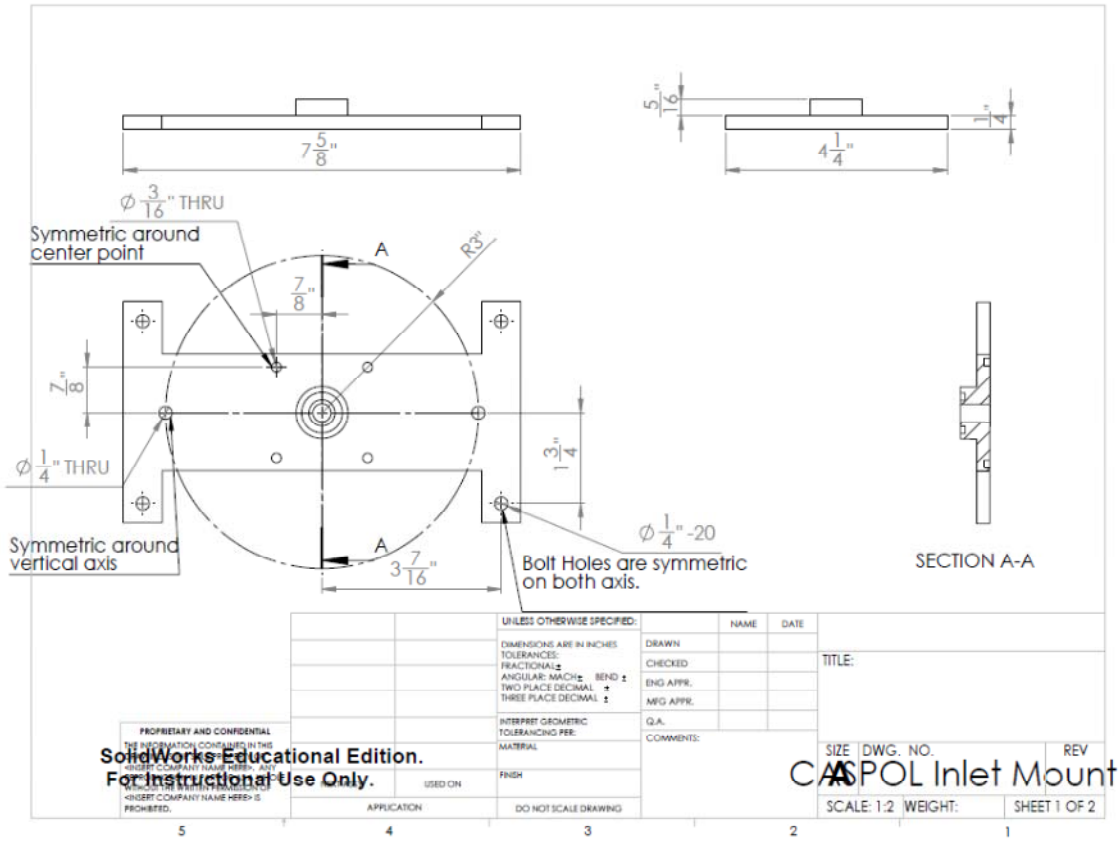


**Figure 46. Machining diagram for the construction of a new CFDC sliding plate which is mountable to the CASPOL.**

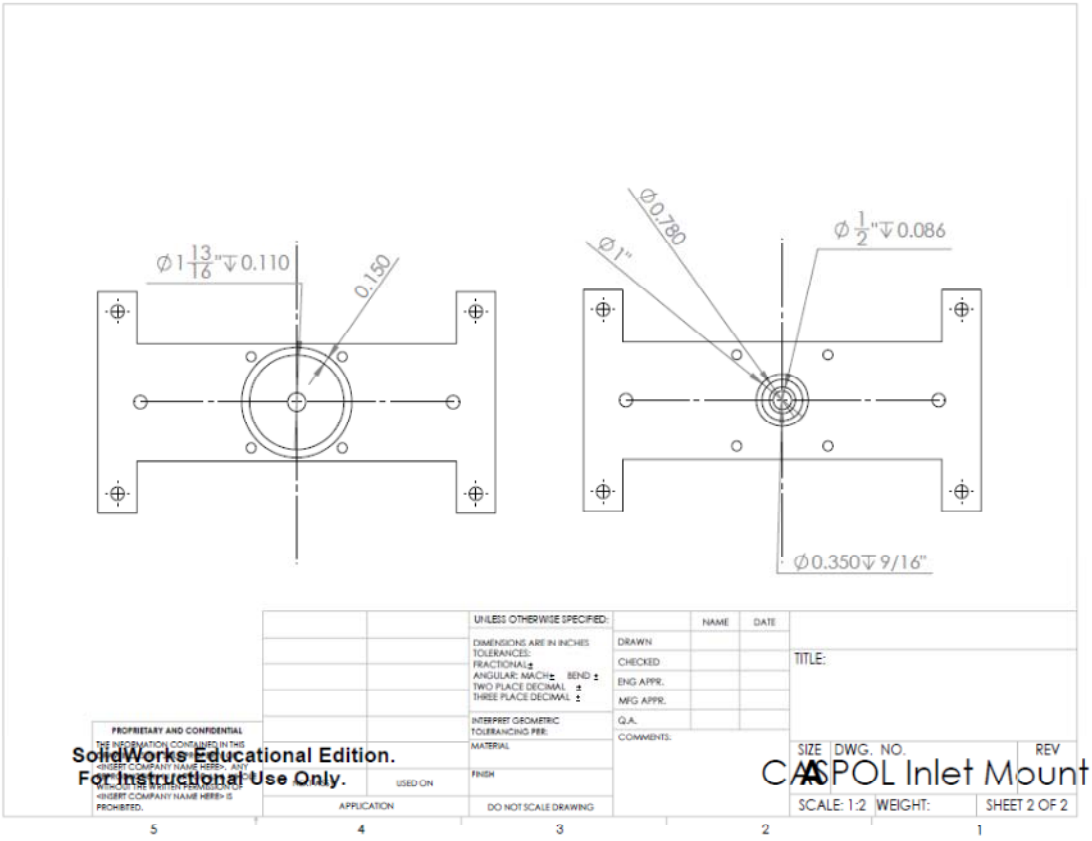


**Figure 47. Machining diagram for the construction of a new CFDC sliding plate which is mountable to the CASPOL.**

CFDC Liquid Cooled Sliding Plate

As previously mentioned the thermal capacity of the sliding plate may be an issue in maintaining ice crystals in the air flow between the CFDC and detector, as the plate is not actively cooled. Experimental tests have shown that the plate is several degrees warmer than the chamber walls. A new plate was therefore designed which allows Slytherm XLT fluid to be pumped around a sheath surrounding the ice crystal laden air in order to keep it a similar temperature to the chamber walls. Figure 48

through Figure 51 show the designs for this sliding plate. The plate maintains the two inlets for evacuation and water fill, but the third inlet (sampling) has a jacket surrounding it with two ports for connection in series to the cooling lines. The plate also has a reduced amount of material reducing the thermal mass of the entire plate.

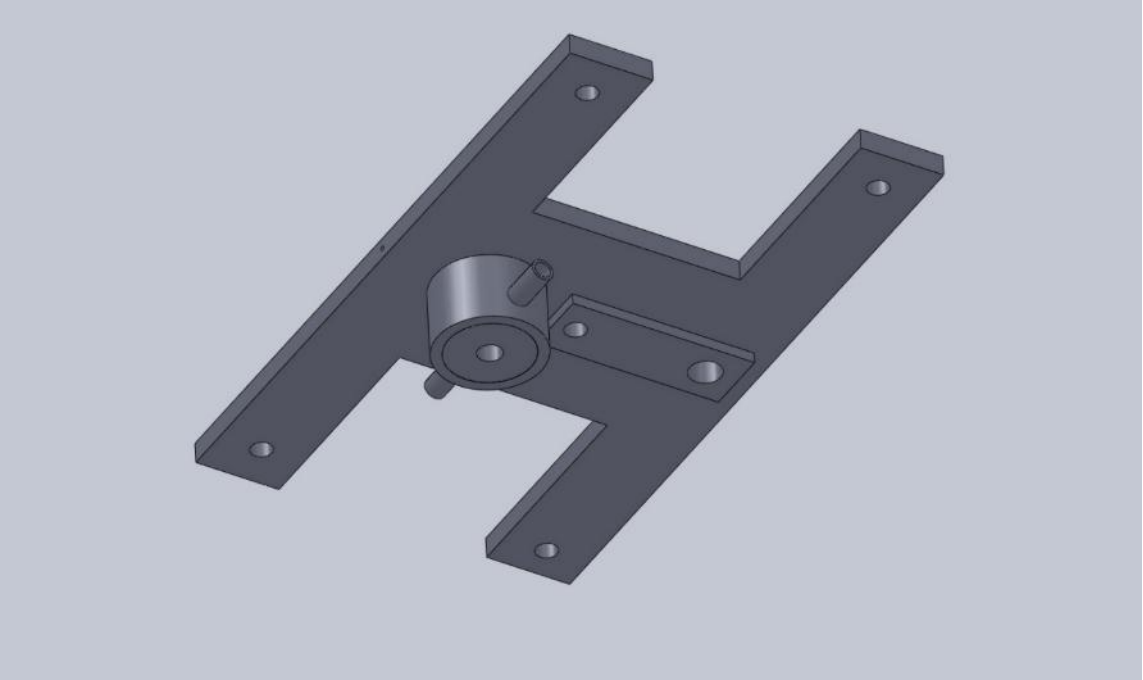

**Figure 48. Modified CFDC sliding plate for connecting to the CASPOL. Reduced thermal mass to reduce particle loss and active cooling sheath around sample line. This image is taken from underneath of the plate.**

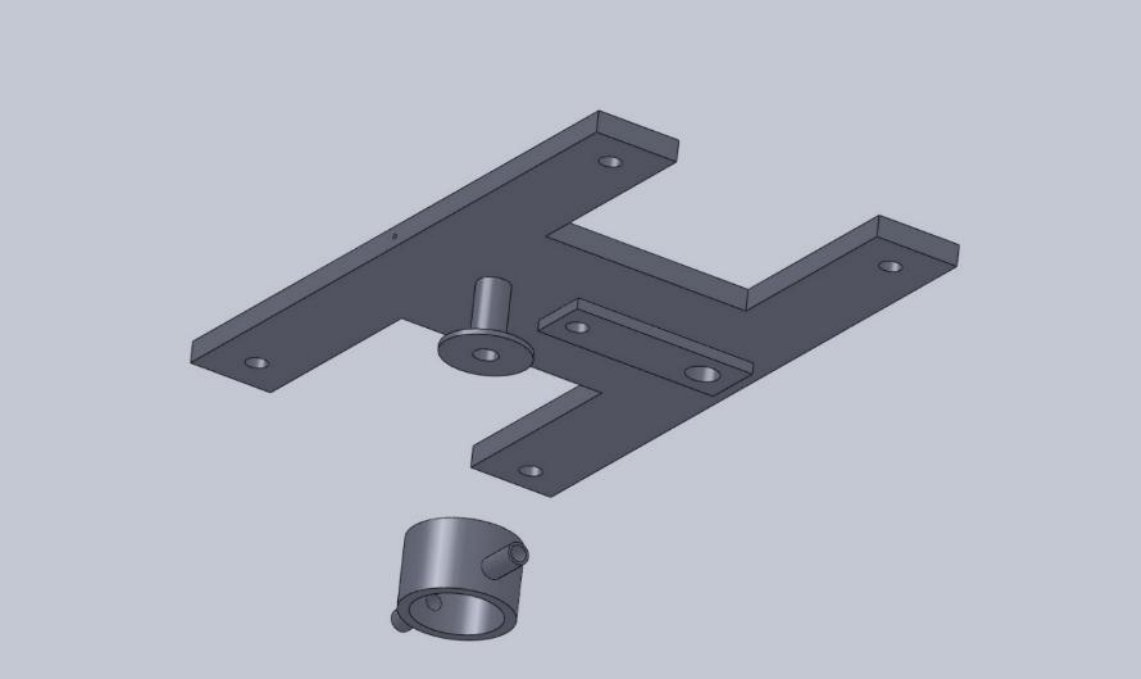

**Figure 49. Modified CFDC sliding plate for connecting to the CASPOL. Reduced thermal mass to reduce particle loss and active cooling sheath around sample line. This image is taken from underneath of the plate with the cooling sheath removed.**

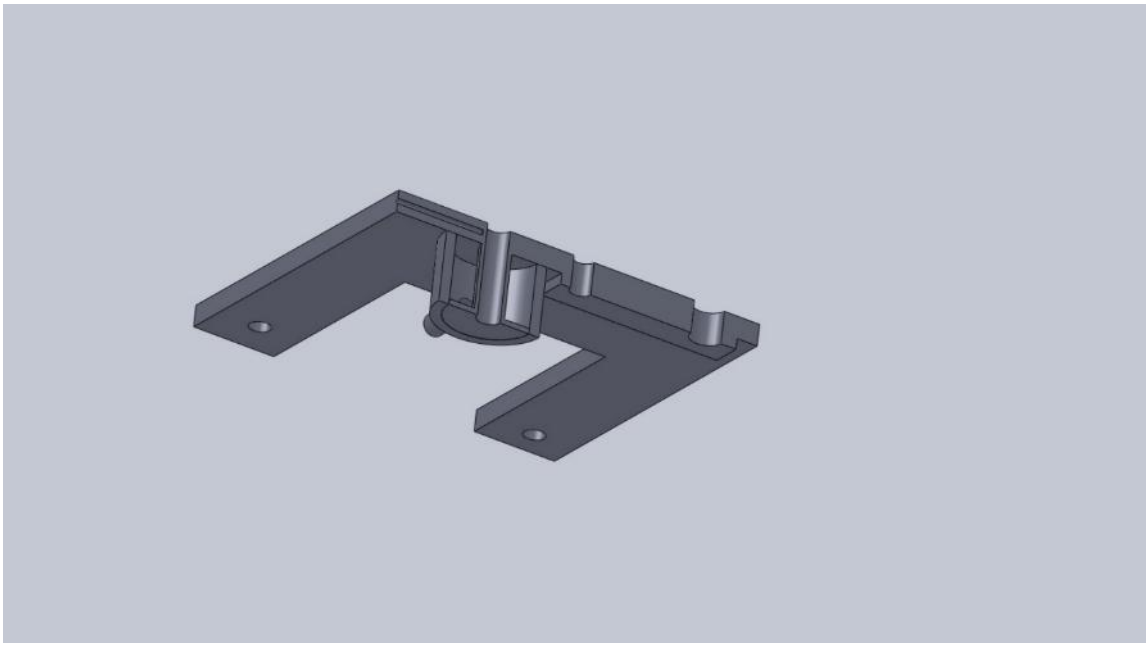

**Figure 50. Modified CFDC sliding plate for connecting to the CASPOL. Reduced thermal mass to reduce particle loss and active cooling sheath around sample line. This image shows a cross section through the plate.**

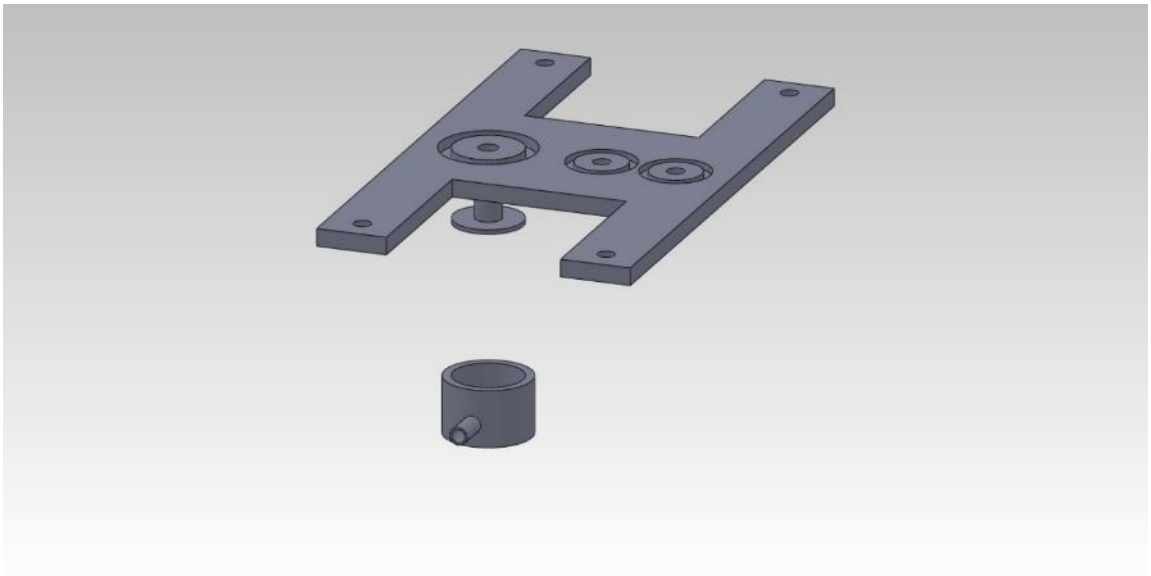

**Figure 51. Modified CFDC sliding plate for connecting to the CASPOL. Reduced thermal mass to reduce particle loss and active cooling sheath around sample line. This image shows the top of the plate with the sheath removed. The 'o' ring groves for seal to the base plate of the CFDC are shown for each of the three connection ports.**

## CFDC Rack Mount

One major observation during the ISDAC field campaign was that as the aircraft geared up and down there were often spikes in the IN concentration. This false counting was thought to occur due to the change in vibration throughout the aircraft infrastructure, to that end a new rack was partially designed. This new rack mount for the CFDC uses rubber strapping to support the chamber within an 8020 frame and is shown in Figure 52. This helps support the chamber and should help cut down on ice breaking off the walls and also cut down on the total weight of the instrument and improve accessibility.

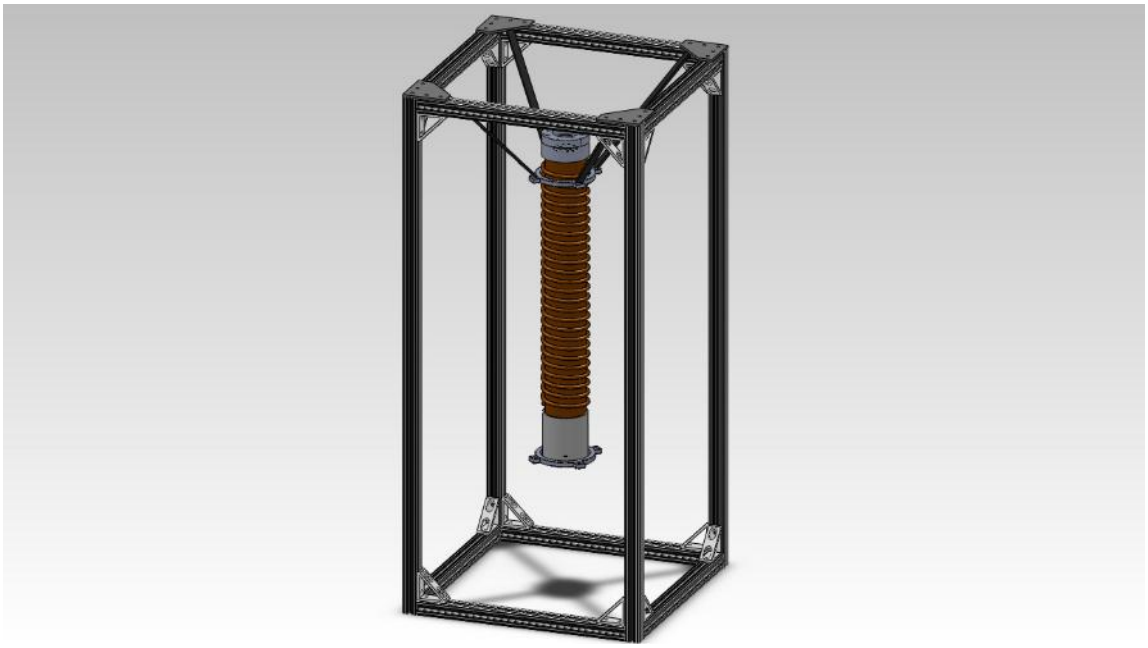

**Figure 52. Improved CFDC rack to reduce vibration issues. The straps support the CFDC and reduce vibration. The dimensions match the current CFDC rack size, however there is much less weight and more access to the instrument.**

# APPENDIX C

## Scattering Signatures for All Atmospheric Dusts – CASPOL MK II

Section 5 discusses the optical scattering properties of atmospheric dusts as measured by the CASPOL MK II. The total backscatter intensity versus the depolarization ratio were shown for three representative dusts in Figure 44. During the laboratory experiments 13 atmospherically relevant dusts were measured using the CASPOL MK II, these dusts were analyzed to determine the three representative groups. The scattering signatures for each of these atmospherically relevant dusts are shown in Figure 53.

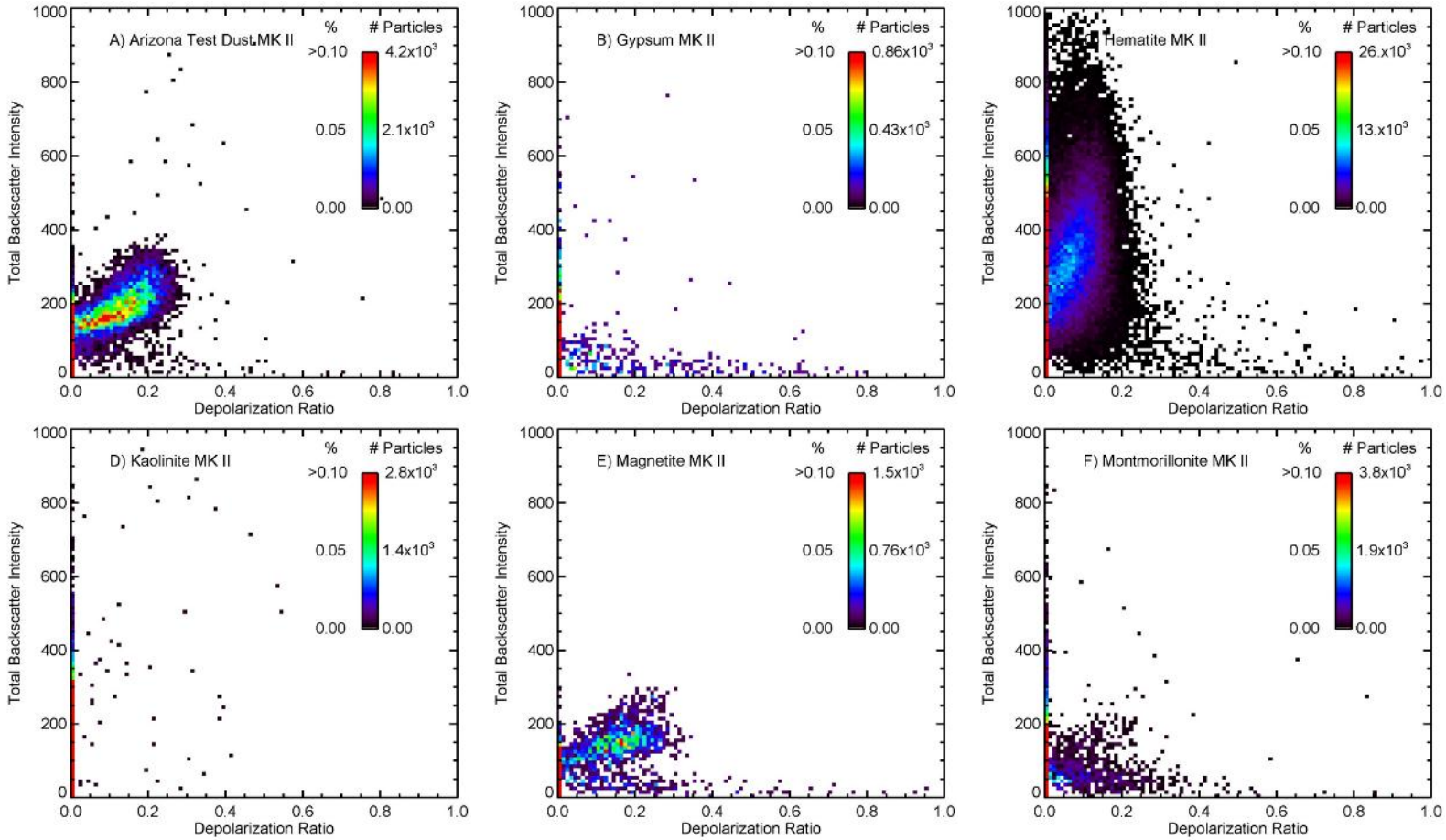


**Figure 53. Total backscatter intensity vs. polarization ratio for representative members of the optical scattering groups A (hematite), B (white quartz) and C (zeolite) are shown.**

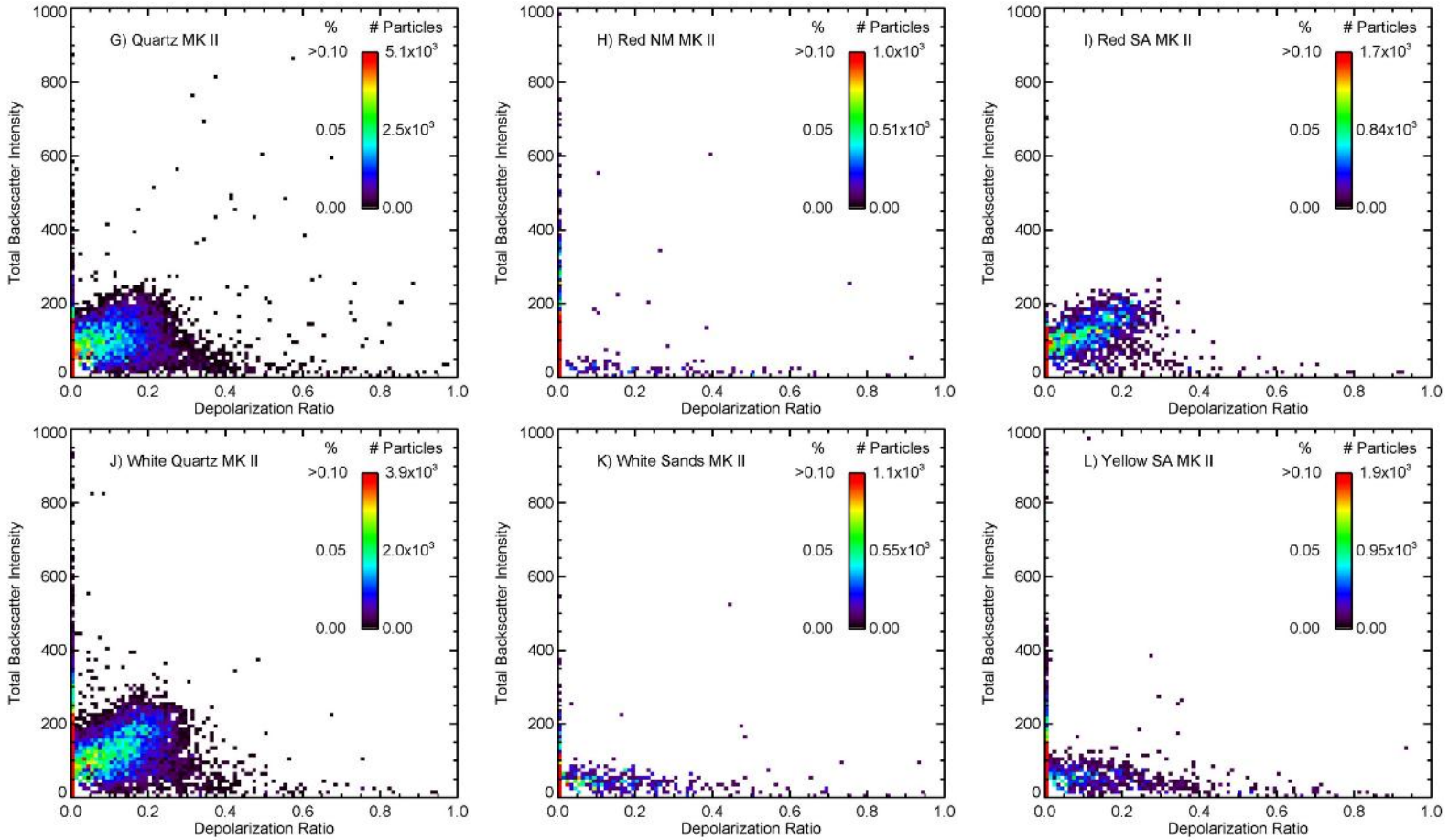


**Figure 53. Continued.**

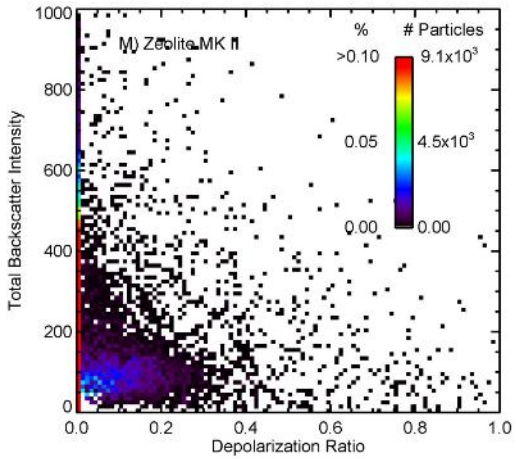


**Figure 53. Continued.**